Master's thesis

Solid Earth Geophysics

Using Three-Component Data for Seismic Interferometry Studies at the Kylylahti Mine, Eastern Finland

Sakari Väkevä

14th May 2019

Advisors:	Emilia Koivisto
	Gregor Hillers
Censors:	Gregor Hillers
	Emilia Koivisto

HELSINGIN YLIOPISTO — HELSINGFORS UNIVERSITET — UNIVERSITY OF HELSINKI

Tiivistelmä — Referat — Abstract

Den reflektionsseismiska mätmetoden är nyttig då man bedriver mineralprospektering i den kristallina berggrunden på grund av dess bra djupdimension och upplösning. De traditionella experimenten med aktiva källor är dock dyra och svåra att utföras, särskilt i avlägsna trakter eller i naturskyddsområden där mineralprospektering är begränsad på grund av miljöskäl. Under den senaste tiden har ett antal teoretiska framsteg bevisat att passiva lodningar som utnyttjar omgivningens seismiska brus kan ge nya möjligheter till seismisk avbildning och bidra till datagenerering för reflektionsseismiska undersökningar, utan att det behövs några explosions- eller vibrationskällor. En av de mest lovande nya metoderna är seismisk interferometri där impulsresponsen mellan två mottagare rekonstrueras genom att korrelera deras signaler mot varandra.

COGITO-MIN är ett gemensamt projekt mellan Helsingfors universitet, Geologiska forskningscentralen, Polska vetenskapsakademien och industripartner med syfte att undersöka och utveckla nya kostnadseffektiva seismiska prospekteringsmetoder i den kristallina berggrunden. Inom ramen för projektet genomfördes ett passivt-seismiskt experiment där 45 trekomponentsgeofoner distribuerades under en månad i närheten av den polymetalliska Kylylahtigruvan i Polvijärvi, norra Karelen, där gruvoperatören är det svenska metallföretaget Boliden. Det ursprungliga syftet med de här geofonerna var att samla in data som är lämpliga för att upptäcka underjordiska hålor relaterade till kärnvapenexplosioner. Institutet som samlade in datan var CTBTO (Comprehensive Test Ban Treaty Organization) vars uppgift är att övervaka det omfattande testförbudsfördraget i världen innan det har ratificerats.

Syftet med denna magisteravhandling var att utveckla ett interferometriskt arbetsflöde för seismiska trekomponentsdata och att utreda metodens prestanda i ett område där den lokala geologin redan är välkänd efter nästan 40 år av prospekteringar och efter den därpå följande gruvbrytningen. De specifika vetenskapliga målen till avhandlingen är (1) att påvisa nyttan med att samla in trekomponentsdata i sammanhang med eller i stället för enkomponentsdata, (2) att forska de brusbaserade interferometrimetoder som använts i tidigare studier och förbättra deras stabilitet i den kristallina berggrunden samt (3) att utreda möjligheterna för seismisk interferometri ur ett operativt perspektiv.

Hastighetsvärden som erhållits genom laboratoriemätningar slogs ihop med Bolidens geologiska modell över målområdet. De resulterande hastighets- och täthetsrutnäten användes sedan som basen för vågformsmodellering, och resultaten från seismisk interferometri validerades mot dem. Utgångspunkten för seismisk interferometri var det brusstyrda tillvägagångssättet där "varje sampel räknas". Det interferometriska arbetsflödet bygger på Seismic Unix -produkten och självskrivna algoritmer som baserar sig på teoretiska resonemang. Interferometrin följs av ett avbildningssteg som utgör en grund för de seismiska tvärsnitten. Avhandlingsarbetet fokuserar på fem komponenter i Greentensoren samt den vertikala, radiella och transversa komponenten av impulssvaret. Med de horisontala komponenterna kan man komma åt S-vågor förutom P-vågorna.

Som specialitet testades också den så kallade teckenbitnormaliseringen där amplitudinformationen hos de ursprungliga seismogrammen hade förstörts genom att endast lämna kvar teckenbiten på varje sampel. Enligt resultaten kan teckenbitnormaliseringen göra det lättare att avbilda markens svaga reflektorer. Denna typ av seismisk interferometri verkar särskilt lämplig för det tidiga prospekteringssteget, där prospekteraren ännu inte har fullständig förståelse för det föremål han studerar. Den viktigaste fördelen med seismisk interferometri är dock dess kostnadseffektivitet och potentialen för minskningen av miljöriskerna.

HELSINGIN YLIOPISTO — HELSINGFORS UNIVERSITET — UNIVERSITY OF HELSINKI

Tiedekunta — Fakultet — Faculty	Koulutusohjelma — Utbildningsprogram — Education programme
Faculty of Science	Master's Programme in Geology and Geophysics

Tekijä — Författare — Author
Sakari Väkevä

Työn nimi — Arbetets titel — Title
Using Three-Component Data for Seismic Interferometry Studies at the Kylylahti Mine, Eastern Finland

Opintosuunta — Studieinriktning — Study track
Solid Earth Geophysics

Työn laji — Arbetets art — Level	Aika — Datum — Month and year	Sivumäärä — Sidoantal — Number of pages
Master's thesis	14th May 2019	76 pages + 5 appendix pages

Tiivistelmä — Referat — Abstract

The reflection seismic surveying method is useful when conducting mineral exploration in the crystalline bedrock because of its good depth extent and resolution. However, the traditional experiments with active sources are expensive and difficult to carry out, especially in remote areas or in conservation areas where mineral exploration is limited due to environmental reasons. Recently, a number of theoretical advances have proven that passive soundings utilizing ambient seismic noise can provide new opportunities for seismic imaging and contribute to data generation for reflection seismic surveys, without the need for explosive or vibratory sources. One of the most promising new methods is seismic interferometry (SI), where the impulse response between two receivers is reconstructed by correlating their signals with each other.

COGITO-MIN is a joint project between the University of Helsinki, the Geological Survey of Finland, Polish Academy of Sciences, and industrial partners with the aim of investigating and developing new cost-effective seismic exploration methods in the crystalline bedrock. Within the framework of the project, a passive seismic experiment was carried out in which 45 three-component geophones were deployed for a month in the vicinity of the polymetallic Kylylahti Mine in Polvijärvi, northern Karelia, where the mining operator is the Swedish metal company Boliden. The original purpose of these geophones was to collect data suitable for detecting underground cavities related to underground nuclear explosions. The institute that collected the data was CTBTO (Comprehensive Test Ban Treaty Organization) whose task is to monitor the treaty in the pre-ratification stage.

The purpose of this Master's thesis was to develop an SI workflow for the three-component data and to investigate the method's performance in an area where local geology is known after nearly 40 years of exploration and consequent mining operations. The specific scientific objectives of the thesis are (1) to demonstrate the usefulness of collecting three-component data in conjunction with or instead of single-component data, (2) to assess the noise-based SI methods used in previous studies and to improve their stability in the crystalline bedrock, and (3) to investigate the possibilities of SI from an operational perspective.

Seismic velocities obtained through laboratory measurements were merged with geological and density models of the target area provided by Boliden. The resulting velocity and density grids were then used as the basis for waveform modelling, and the results from SI were validated against them. The starting point for SI was the noise-driven approach where 'each sample matters'. The interferometric workflow is built on the Seismic Unix suite together with self-written algorithms that are based on theoretical evaluations. SI is followed by an imaging workflow, which provides the basis for the reflectivity profiles. The thesis work focuses on five components of the Green's tensor and the vertical, radial and transverse component of the impulse response. With the horizontal components, one can access the S-wave patterns in addition to the P-waves.

As a specialty, the so-called sign bit normalization (SBN) method was also tested. The technique involves destroying much of the amplitude information of the original seismograms by only retaining the sign bit of each sample. According to the results outlined in this thesis, SBN can make it easier to image the weak reflectors of the subsurface. This type of seismic interferometry seems particularly suitable for the early stage of mineral exploration, where the explorer does not yet fully understand the target they are studying. The most important advantage of seismic interferometry, however, is its cost effectiveness, and its potential for reducing risks for the environment.

Avainsanat — Nyckelord — Keywords
seismic reflection method, seismic interferometry, three-component acquisition, Outokumpu, Kylylahti

Säilytyspaikka — Förvaringsställe — Where deposited
HELDA

Muita tietoja — övriga uppgifter — Additional information

Acknowledgements

Contents

Acronyms

1C	one-component
3C	three-component
ANSI	Ambient Noise Seismic Interferometry
BP	bandpass
CMP	common midpoint
COGITO-MIN	Cost-effective Geophysical Imaging Techniques for Supporting Ongoing Mineral Exploration in Europe
CTBTO	Comprehensive Test Ban Treaty Organization
DAS	distributed acoustic sensing
DFT	discrete Fourier transform
E-MORB	enriched mid ocean ridge basalt
EGF	empirical Green's function
FD	finite-difference
GF	Green's function
GTK	Geological Survey of Finland
IG-PAS	Institute of Geophysics at Polish Academy of Sciences
IMS	International Monitoring System
ISUH	Institute of Seismology, University of Helsinki
KAL	Kalevian schists
LOTI	low-Ti tholeiite
MESI	Mineral Exploration Seismic Interferometry
MORB	mid ocean ridge basalt
MS/SMS	massive to semimassive sulphide mineralization
MSEED	Standard for the Exchange of Earthquake Data, miniature format

NMO	normal move-out
NRM	normal remanent magnetization
OME	carbonate-skarn-quartz rock alteration haloes in ultramafics
OSI	on-site inspection
OUM	Outokumpu ultramafic rocks
PGE	platinum group elements
PML	perfectly matched layer
SAMS	Seismic Aftershock Monitoring System
SBN	sign-bit normalization
SCLM	subcontinental lithospheric mantle
SI	seismic interferometry
SNR	signal-to-noise ratio
STF	source time function
SW	spectral whitening
UH	University of Helsinki
UNE	underground nuclear explosion
VHMS	volcanic hosted massive sulphide
ZNE	vertical–north–east
ZRT	vertical–radial–transverse

Chapter 1

Introduction

Le bruit de fond est fond de notre perception, sans aucune interruption, il est notre nourriture pérenne, il est l'air du logiciel.

— Serres, Michel (1982). *Genèse.* Éditions Grasset et Fasquelle, p. 16.

1.1 Background of the present study

Seismic surveys provide important information for deep ore exploration due to their non-invasive character, and good depth resolution and depth extent. In the active reflection seismic method, seismic wave energy is produced at ground surface using explosives or by shaking the ground with pulses of vibration. Some of the downgoing wave energy is reflected or backscattered at buried geological structures and lithological contacts and propagates back towards the surface. These reflections can be identified as coherent arrivals recorded over an array of geophones. With conventional processing techniques, these data can be used to obtain a 2D reflectivity section or a 3D reflectivity cube of the subsurface.

In the early stage of ore exploration (reconnaissance), there is a pressure to characterise the target with techniques that minimize costs but can still point out promising drilling targets with reasonable confidence. To meet the needs of the exploration sector and to respond to the increasing environmental concerns of local communities, non-invasive passive methods could provide an alternative to active source surveying in sensitive areas such as natural protection sites or wherever there are terrain restrictions for operating sources. Seismic interferometry (SI) is a comparatively new theoretical development for acquiring base data for reflection seismic surveys (Wapenaar and Fokkema 2006). It has for a long time been applied for ambient noise tomography, where the fundamental modes of surface-waves have been extracted using SI (e.g., Sabra et al. 2005; Nishida et al. 2009), but practical implementations of body-wave interferometry are still scarce. This is partly due to difficulties in retrieving the body-wave response given that surface-wave energy is dominating the ambient noise background (Chamarczuk et al. 2018).

In passive SI, the impulse response of the elastic system (i.e., bedrock) is retrieved from passive recordings, without prior control over the seismic sources. In scientific terms, SI is about reconstructing the Green's function (GF) **G** with the mathematical operation of cross-correlation. When empirical Green's function (EGF) retrieval is successively applied at each station on a geophone array, a set of virtual shot gathers is produced, as if there had been a line of explosions on the ground surface. Generally, SI surveys aim at long recording times (dozens of days) to improve the signal-to-noise ratio.

The objective of the present study is to demonstrate the benefits of seismic body-wave interferometry at the Kylylahti Mine in eastern Finland, an active sulphide mine area with known local geology. An SI implementation for three-component seismic data in 2D is developed and its performance is discussed. The migrated sections are validated and cross-checked against known geology and synthetic finite-difference (FD) modelling.

1.1.1   Advancing cost-effective method development

Cost-effective Geophysical Imaging Techniques for Supporting Ongoing Mineral Exploration in Europe (COGITO-MIN) is a joint project of the University of Helsinki (UH), Geological Survey of Finland (GTK), Institute of Geophysics at Polish Academy of Sciences (IG-PAS) and the industrial partners Boliden, Vibrometric, and Geopartner, with the aim to introduce and benchmark new cost-effective mineral exploration methods in crystalline bedrock (Koivisto et al. 2018). The project was funded for three years (2016–2018) through the third ERA-MIN joint call, addressing sustainable supply of raw materials in Europe. The funding for the Finnish project partners came from Business Finland (former Tekes – the Finnish Funding Agency for Technology and Innovation) and for the Polish project partners from the NCBR (Narodowe Centrum Badań i Rozwoju), an implementing agency in Poland supporting research and development.

The methods tested in COGITO-MIN include, among others, multi-azimuth vertical seismic profiling with conventional geophones and DAS technology (Riedel et al. 2018), sparse 3D active seismic profiling (Singh et al. in press), 3D seismic interferometry with ambient noise surface recordings (Chamarczuk et al. 2018), 2D reflection imaging (Heinonen et al. 2019), and audiomagnetotellurics (Koivisto et al. 2018). The test field of the project was the polymetallic Kylylahti deposit in Eastern Finland. A particularly noteworthy aspect of the fieldworks was the deployment of 1,000+ geophones on a $10 \, \text{km}^2$ rectangular grid (cf. Fig. 1.1), recording 20 hours a day over the course of one month in the summer of 2016. The experiment resulted in almost three terabytes of usable surface-based one-component (1C) SI data.
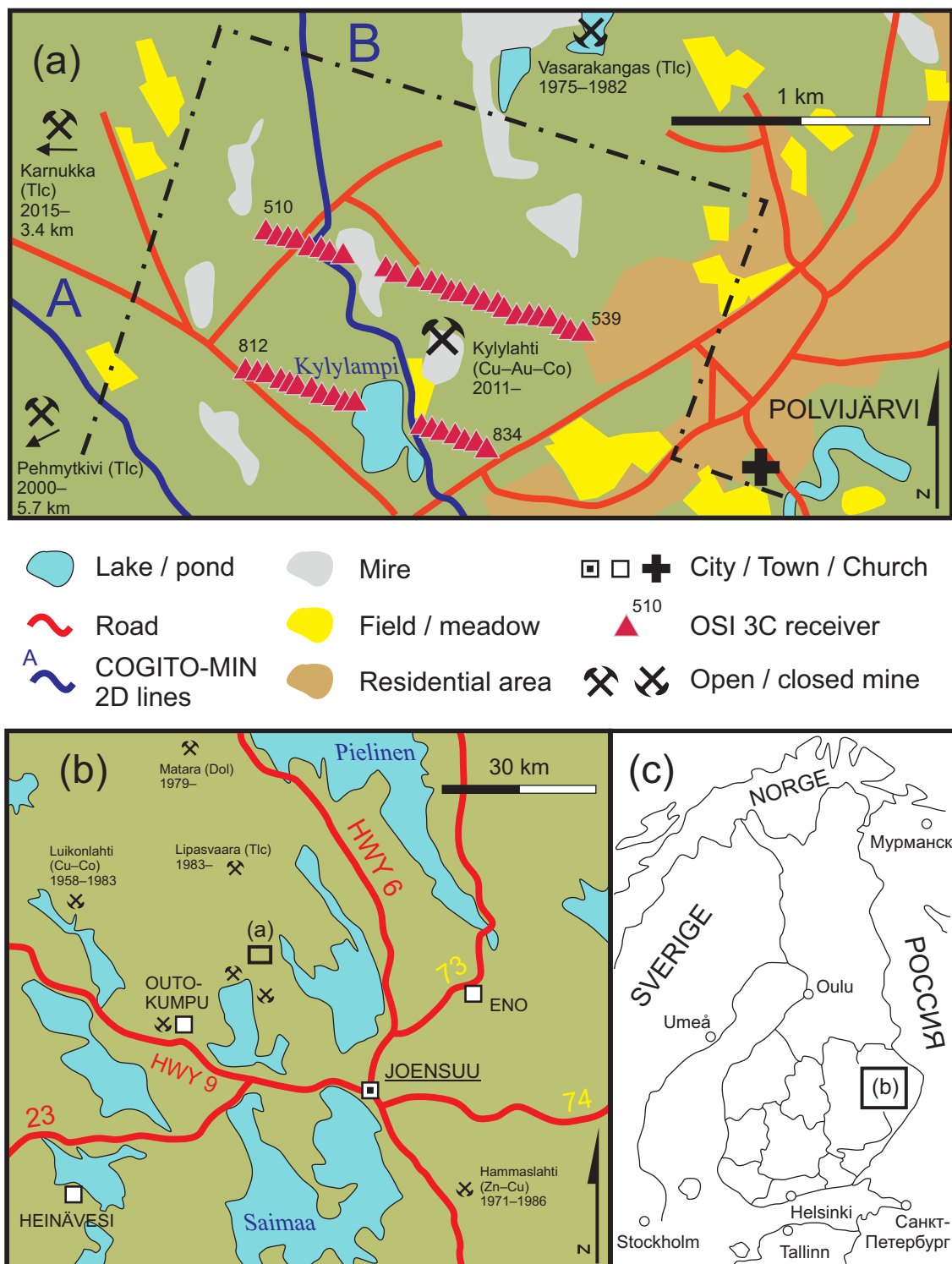
Figure 1.1: Maps showing the general location of Kylylahti mine in the municipality of Polvijärvi, North Karelia. (a) Town map. The on-site inspection (OSI) receivers (used in this study) are depicted as pink triangles. The COGITO-MIN 2D active seismic lines (A & B) are depicted as blue lines. The COGITO-MIN 1C receiver grid area is shown using a dash-dot line. (b) Regional map of North Karelia with some active and closed mines indicated. (c) Index map showing Finland and its neighbour countries. Modified from the Background map and Topographic map datasets by the National Land Survey of Finland (2019). The original maps are licensed under CC BY 4.0.

1.1.2   The challenging Kylylahti deposit

The polymetallic Kylylahti deposit (named after Kylylahti Bay at north end of Lake Polvijärvi) is located in the municipality of Polvijärvi in the region of North Karelia, Finland (see Fig. 1.1). Its mineral resources (measured, indicated and inferred) are estimated at 5.95 Mt @ 0.36 ppm Au, 0.44 % Cu, 0.23 % Zn, 0.26 % Ni, and 0.13 % Co (Boliden 2017), making it a medium sized deposit from a Finnish perspective. Kylylahti mine entered production in 2012, and it produces concentrate from the complex Cu–Au–Co ore. Boliden, a Swedish mining and smelting company, took over the mine in 2014 (Boliden 2015). In 2018, the production of the mine totalled 790 kt of ore (Boliden 2018). The agglomeration of Polvijärvi with its 4,000 inhabitants is in immediate proximity of the mining concession.

Kylylahti is part of the historic Outokumpu Field lavished with numerous Cu–Zn–Co deposits such as the Outokumpu, Vuonos and Luikonlahti, where mining has already ended, and the smaller deposits of Perttilahti and Saramäki, where Boliden also holds exploration areas. In Kylylahti, the massive to semimassive mineralization occurs in a narrow patch dipping SSW at 40°–50°, in an apparent parasitic fold of a larger synformal fold system. The extensive 'deep ore', or the so called Wombat subdomain, is presently being mined at depths greater than 700 meters. Despite a long history of drilling campaigns, a deep extension of the current mineralization has not been discovered, and the mine is approaching end of life. The marginal contacts on the eastern limb of the synform are near-vertical, limiting the use of reflection seismics on ground surface. The reflectivity patterns obtained from conventional seismics are therefore usually marked by piecewise, disconnected reflectivity (Riedel et al. 2018; Singh et al. in press).

1.2   Previous studies

After the theoretical developments in the early 2000's by, e.g., Wapenaar and Fokkema (2006), there have been several synthetic verifications for the basic analytical results involving body-wave interferometry. Thorbecke and Draganov (2011) tested the SI method in a synthetic setting with horizontal buried impedance contrasts, and investigated how the quality of Green's function retrieval depends on source distribution and source strength. They concluded that the short duration of local seismic sources can be compensated with longer overall recording times, but improper target illumination is difficult to compensate by any means. The finite-difference modelling code used for their article is publicly available in Jan Thorbecke's GitHub repository (`https://github.com/JanThorbecke`).

Cheraghi et al. (2015) report a pilot SI study in a Au–Zn brownfield environment in Lalor Mine, Canada. Their ambient noise data totalling 300 h were used for seismic interferometry over an area of 4 km^2. Their workflow produced partial retrievals of shallow reflectors

but rather unconvincing retrievals of steep reflectors. The COGITO-MIN project was a follow-up of this work, and our SI experiment, particularly when it comes to the recording times and receiver geometry, was planned using this experiment as a 'template'.

Chamarczuk et al. (2018) developed a robust mineral exploration SI workflow (MESI) for the COGITO-MIN SI data and presented preliminary results for the migration volume. As part of their work, they implemented an algorithm for identifying body-wave events in seismic recordings (Chamarczuk et al. 2019). The MESI workflow comprises bandpass (BP) filtering to attenuate surface and S waves in their characteristic frequency ranges, automatic source location methods, and EGF retrieval and selective stacking of the data that contain sources located within the stationary-phase areas. Chamarczuk et al. (2018) report variable reflective patterns in the subsurface, despite the difficulty of obtaining continuous reflections. They also make a note about the challenging structural environment, a possibly biased distribution of seismic sources, and the fact that the sampled wavefield may still be a mixture of body-wave and non-body-wave energy despite filtering attempts.

1.3   Objectives of the present study

Parallel to the COGITO-MIN experiment, the Comprehensive Test Ban Treaty Organization (CTBTO) was using the Kylylahti mine site as a testing ground to develop an emergent technique, resonance seismometry (Labak et al. 2017), for detecting underground cavities related to suspected underground nuclear explosions (UNEs). CTBTO is a preparatory commission constituted shortly after the 1996 United Nations General Assembly meeting where the treaty was opened for signature. After ratification by all the Annex 2 states[1], the full verification regime will be established, consisting of an International Monitoring System (IMS), a consultation and clarification process, on-site inspections (OSIs), and other confidence-building measures such as regular instrument calibrations (Bönnemann 2017). OSIs are forensic measures carried out in suspected test sites to verify if an UNE has occurred, and in the case of the Kylylahti experiment, the underground mining infrastructure served as an analogue of a nuclear test site. The CTBTO/OSI experiment featured 45 three-component (3C) seismometers, recording for about 30 days along two of the COGITO-MIN receiver lines (see Fig. 1.1), here named the Northern and Southern line, or Line 05 and Line 08.

In this study, the CTBTO/OSI data and experiences from COGITO-MIN's 1C interferometry experiment (Chamarczuk et al. 2018, 2019) are used for developing a passive seismic 3C interferometric workflow. The results are supported with synthetic modelling over the receiver lines. In principle, if all three axes of a 3C recording system are available, GF is obtained in tensor form after correlating the 3×3 trace pairs associated with each virtual source and receiver. With proper rotation of the tensor's coordinate system, the S-wavefield

---

[1]The 44 states whose signature and ratification are required for CTBT to enter into force.

can be separated into the transverse and radial components, while the P-wavefield remains in the vertical component. More sophisticated wavefield separation techniques also exist (e.g., Baan 2006) and could be applied to the data in the future.

Exploration with S-waves or 3C exploration are very specialized techniques in mineral exploration that, however, provide many benefits to P-waves such as a better depth resolution and stronger seismic impedance contrasts as seen in petrophysical assessments. Cross-validation of 3C and 1C datasets does not yet form a part of a typical SI field experiment since there are no well-established workflows for handling 3C data, but in time to come, such comparisons may be made in a routinely fashion. One of the objectives in my thesis is, indeed, to demonstrate the usefulness of acquiring some 3C data together with massive 1C spreads. The work at hand hopes to put new impetus on S wave utilization by demonstrating new approaches to processing and presenting 3C data.

In 3C exploration, it is useful to separate the SH component from radial and vertical orientations, since it does not involve any converted waves (Sheriff and Geldart 1995). Since the stations are not by default oriented in the in-line direction, a coordinate system rotation is needed. For a rotation from the conventional ZNE system into ZRT, only five Green's tensor components out of nine will suffice; the correlations between, e.g., vertical and horizontal channels do not matter as much because they cannot used for the direct interpretation of the subsurface.

Mining industry does not generally have an incentive to develop and experiment with mathematically and computationally heavy methods themselves as long as conventional exploration methods suit its needs and are well established. Therefore, the work done by academia is a valuable contribution to mineral exploration and, ultimately, benefits the industry as well.

1.4 Research questions

This study aims to answer three central questions related to 3C seismic interferometry in crystalline bedrock. The first question is whether it is possible to demonstrate a benefit in acquiring 3C data together with 1C spreads, or instead of them. As mentioned in earlier sections, the CTBTO/OSI deployment was not originally intended for mineral exploration. However, its alignment with two in-lines from the 1,000+ geophone grid allows side-by-side comparisons, and, if any benefit can be demonstrated, the extra components may indeed become an essential part of future exploration campaigns.

The second question is to investigate the relation of noise-driven (such as ANSI by Draganov et al. 2013) versus event-driven (such as MESI by Chamarczuk et al. 2018) SI approaches in mineral exploration and to find out how the former method could be further refined to improve its stability in crystalline bedrock. Remote or untouched areas often suffer from a

low natural seismic background, but methods familiar from earthquake seismology such as one-bit clipping in the time domain (Bensen et al. 2007; Cupillard and Capdeville 2010) can be tested to improve the performance of the noise-driven SI. A deeper understanding is also needed on the effect of recording time on the retrieved Green's functions.

The third question incorporates both technical and practical elements and concerns the potentials of the SI method. It can be speculated that SI is most helpful in the reconnaissance stage of mineral exploration, especially in sensitive areas such as nature protection sites where one often has to preliminarily characterize the target with non-invasive methods and only after acquiring substantial evidence can proceed to invasive methods such as diamond drilling or excavating test pits and trenches. A successful implementation of noise-driven 3C SI can offer several new lines of evidence for the interpreter, and would therefore be of interest to many geologists working on green- and brownfield mineral exploration.

Chapter 2

Principles of seismic interferometry

> *Le bruit de fond devient l'un des objets de la métaphysique. Il est aux limites de la physique et la baigne, il gît sous les découpes de tous les phénomènes, protée prenant toute apparence, matière et chair des manifestations.*
>
> — Serres, Michel (1982). *Genèse*, p. 21.

2.1 Green's function representation

For the notations and definitions used in this chapter, please refer to Appendix A.

2.1.1 Acoustic wave equations

Consider a continuous volume in space where each point $\mathbf{x}$ has been assigned density $\rho(\mathbf{x})$ and compressibility $\kappa(\mathbf{x})$. In addition, assume that the medium cannot sustain shear so that it behaves similarly to fluids such as air or water. This called the *acoustic assumption*. In absence of body forces, the propagation of pressure fields in the volume can be represented by the acoustic wave equations, which are a set of linear differential equations (Wapenaar and Fokkema 2006)

$$\begin{cases} \rho(\mathbf{x})\dot{\mathbf{v}}(\mathbf{x},t) + \nabla p(\mathbf{x},t) = \mathbf{f}(\mathbf{x},t) = \mathbf{0} \\ \kappa(\mathbf{x})\dot{p}(\mathbf{x},t) + \nabla \cdot \mathbf{v}(\mathbf{x},t) = q(\mathbf{x},t) \,, \end{cases} \tag{2.1.1}$$

where ∇ is the spatial operator of partial derivatives, $p(\mathbf{x},t)$ is the pressure field, $\mathbf{v}(\mathbf{x},t)$ is the velocity field and $q(\mathbf{x},t)$ is the distribution of pressure sources.

The Fourier-domain pair of the equations (2.1.1) is

$$\begin{cases} j\omega\rho(\mathbf{x})\hat{\mathbf{v}}(\mathbf{x},\omega) + \nabla \hat{p}(\mathbf{x},\omega) = \mathbf{0} \\ j\omega\kappa(\mathbf{x})\hat{p}(\mathbf{x},\omega) + \nabla \cdot \hat{\mathbf{v}}(\mathbf{x},\omega) = \hat{q}(\mathbf{x},\omega) \,. \end{cases} \tag{2.1.2}$$

To give an example, consider an acoustic medium that is excited with the simplest possible elementary source: a unit impulse centered at $\mathbf{x} = \mathbf{0}$ that is set off at time $t = 0$. We can express the source as $q(\mathbf{x}, t) = \delta(\mathbf{x})\delta(t)$ or $\hat{q}(\mathbf{x}, \omega) = \delta(\mathbf{x})$. By inserting this into the equations above, we get

$$\omega^2 \kappa(\mathbf{x})\hat{p}(\mathbf{x}, \omega) + \nabla \cdot \rho^{-1}(\mathbf{x})\nabla\hat{p}(\mathbf{x}, \omega) = -j\omega\delta(\mathbf{x}) . \tag{2.1.3}$$

With constant κ and ρ, this further reduces to

$$\left(k^2 + \nabla^2\right)\hat{p}(\mathbf{x}, \omega) = -j\omega\rho\delta(\mathbf{x}) , \tag{2.1.4}$$

where $k = \omega\sqrt{\rho\kappa}$ or ω/c_p, defining the speed of the compressional wave as $c_p = (\rho\kappa)^{-1/2}$.

One solution that satisfies (2.1.4) in the far field (that is, at a distance at which only terms decaying as $|\mathbf{x}|^{-1}$ prevail) is

$$\hat{p}(\mathbf{x}, \omega) = \frac{j\omega\rho}{4\pi|\mathbf{x}|}\exp(-jk|\mathbf{x}|) . \tag{2.1.5}$$

It is the Fourier transform of

$$\begin{aligned}
p_{\text{elementary}}(\mathbf{x}, \mathbf{x}_A, t) &= \frac{\rho}{8\pi^2|\mathbf{x}|}\int_{-\infty}^{\infty} j\omega \exp j\omega\left(t - \frac{|\mathbf{x}|}{c_p}\right) \, \mathrm{d}\omega \\
&= \frac{\rho}{8\pi^2|\mathbf{x}|}\frac{\mathrm{d}}{\mathrm{d}t}\delta\left(t - \frac{|\mathbf{x}|}{c_p}\right) .
\end{aligned} \tag{2.1.6}$$

This solution represents the propagation of the wavefront on an expanding spherical shell centered at $\mathbf{x} = \mathbf{0}$.

2.1.2 Green's function

For a single stationary source, assume that the source signature $q(\mathbf{x}, t)$ is separable into a time-dependent part and a location-dependent part so that $q(\mathbf{x}, t) = s(t)\delta(\mathbf{x} - \mathbf{x}_A)$. Assume further that the origin is placed so that $\mathbf{x}_A = \mathbf{0}$. The function $s(t)$ is called the source time function (STF), and assumed to be smooth enough that one can form its derivatives. Instead of solving for $p(\mathbf{x}, t)$ for arbitrary signatures, it is convenient to utilize the linearity of Fourier transform and 'decompose' $q(\mathbf{x}, t)$ into unit impulses. If we know the response of an acoustic system to the elementary unit impulse δ, we can reconstruct the response due to the possibly complicated STF $s(t)$ by using the convolution (A.0.4):

$$p(\mathbf{x}, t) = s(t) * p_{\text{elementary}}(\mathbf{x}, t) \tag{2.1.7}$$

Up to a constant multiplier, the solution can be written as

$$\begin{aligned}
p(\mathbf{x}, t, s(t)) &\propto \int_{-\infty}^{\infty} s(\tau)\frac{\mathrm{d}}{\mathrm{d}(t-\tau)}\delta\left(t - \frac{|\mathbf{x}|}{c_p} - \tau\right) \, \mathrm{d}\tau \\
&\propto -\frac{\mathrm{d}s}{\mathrm{d}t}\left(t - \frac{|\mathbf{x}|}{c_p}\right) ,
\end{aligned} \tag{2.1.8}$$

where the property (A.0.8) has been utilized in the simplification of the derivative. What is remarkable about (2.1.8) is that while the STF was $s(t)$, the waveform recorded in the far field is proportional to $\dot{s}(t)$, or the time derivative of the STF.

The elementary response $p_{\text{elementary}}$ is called the *Green's function (GF)* and may from now on be denoted by $G(\mathbf{x}, t; \mathbf{x}_A, \tau)$ where the first two arguments stand for the observer's location and time, and the last two stand for the location and activation time of the source. The Fourier transform of GF will be denoted by $\hat{G}(\mathbf{x}, \mathbf{x}_A, \omega)$. GF represents the impulse response of the acoustic system due to an impulsive pressure source (see Fig. 2.1). The power of GF is in the equation

$$p(\mathbf{x}, t) = s(t) * G(\mathbf{x}, t; \mathbf{x}_A, \tau) \,, \tag{2.1.9}$$

which can be used for the reconstruction of a linear acoustic system's response due to any physically reasonable STF $s(t)$, when we know the GFs of the system.

$$\begin{cases} \rho(\mathbf{x})\dot{\mathbf{v}}(\mathbf{x}, t) + \nabla p(\mathbf{x}, t) = \mathbf{f}(\mathbf{x}, t) = \mathbf{0} \\ \kappa(\mathbf{x})\dot{p}(\mathbf{x}, t) + \nabla \cdot \mathbf{v}(\mathbf{x}, t) = q(\mathbf{x}, t) \end{cases}$$
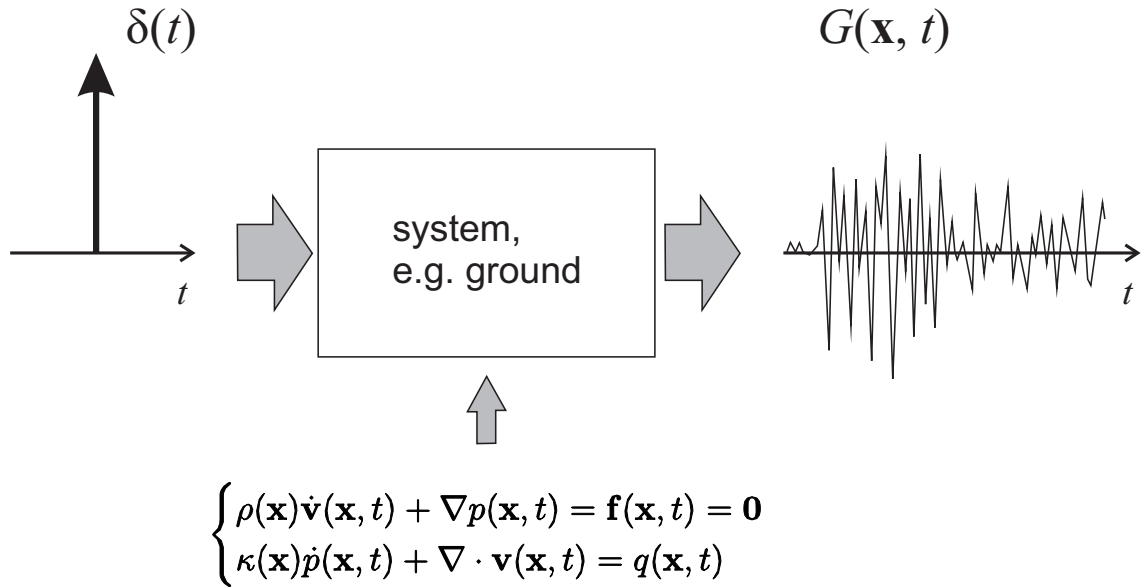
Figure 2.1: The GF $G(\mathbf{x}, t)$ represents the reaction of the system when it is subjected to an impulsive, 'spike-like' input signal $\delta(t)$. In seismology, the elastic system is causal and linear and its behaviour is governed by a set of differential equations (below).

Some of the important properties of the GF are linearity with respect to summation over a numerable set of sources, invariance to time shifts

$$G(\mathbf{x}, t; \mathbf{x}_A, \tau) = G(\mathbf{x}, t - \tau; \mathbf{x}_A, 0) \,, \tag{2.1.10}$$

and the source-receiver reciprocity

$$G(\mathbf{x}_A, t - \tau; \mathbf{x}_B, 0) = G(\mathbf{x}_B, t - \tau; \mathbf{x}_A, 0) \,. \tag{2.1.11}$$

2.1.3   Representation integral

The formula for seismic interferometry is derived from the *reciprocity theorem* (2.1.12) for pressure (p) and velocity ($\mathbf{v}$) fields. The following derivation is based on Wapenaar and Fokkema (2006). Assuming that no body forces are present and that the fields are defined over some domain $\mathcal{D}$, the reciprocity theorem states that

$$\iiint_{\mathcal{D}} [\hat{p}_A^* \hat{q}_B + \hat{q}_A^* \hat{p}_B] \ \mathrm{d}V = \oiint_{\partial\mathcal{D}} [\hat{p}_A^* \hat{\mathbf{v}}_B + \hat{\mathbf{v}}_A^* \hat{p}_B] \cdot \mathrm{d}\mathbf{S} \qquad (2.1.12)$$

in the Fourier domain, where the subscripted A and B stand for two independent acoustic states. Consider the states to hold impulsive point sources activating at $t = 0$ and located at $\mathbf{x}_A$ and $\mathbf{x}_B$, respectively. In this case, the left side of (2.1.12) is simplified as

$$\begin{aligned}
&\iiint_{\mathcal{D}} [\hat{p}_A^* \hat{q}_B + \hat{q}_A^* \hat{p}_B] \ \mathrm{d}V \\
&= \iiint_{\mathcal{D}} \left[\hat{G}^*(\mathbf{x}, \mathbf{x}_A, \omega)\delta(\mathbf{x} - \mathbf{x}_B) + \hat{G}(\mathbf{x}, \mathbf{x}_B, \omega)\delta(\mathbf{x} - \mathbf{x}_A) \right] \ \mathrm{d}V \qquad (2.1.13) \\
&= \hat{G}^*(\mathbf{x}_B, \mathbf{x}_A, \omega) + \hat{G}(\mathbf{x}_A, \mathbf{x}_B, \omega) = 2\Re\left\{ \hat{G}(\mathbf{x}_A, \mathbf{x}_B, \omega) \right\} \ .
\end{aligned}$$

Just like in the sieving property (A.0.5), the volume integral here localizes the GF at the receiver points $\mathbf{x}_A$ and $\mathbf{x}_B$.

The right-hand side of (2.1.12) is rewritten and simplified with equations (2.1.2) and source-receiver reciprocity as

$$\begin{aligned}
&\oiint_{\partial\mathcal{D}} [\hat{p}_A^* \hat{\mathbf{v}}_B + \hat{\mathbf{v}}_A^* \hat{p}_B] \cdot \mathrm{d}\mathbf{S} \\
&= \oiint_{\partial\mathcal{D}} -\frac{1}{j\omega\rho(\mathbf{x})} \left[\hat{G}^*(\mathbf{x}, \mathbf{x}_A, \omega)\nabla\hat{G}(\mathbf{x}, \mathbf{x}_B, \omega) - \nabla\hat{G}^*(\mathbf{x}, \mathbf{x}_A, \omega)\hat{G}(\mathbf{x}, \mathbf{x}_B, \omega) \right] \cdot \mathrm{d}\mathbf{S} \qquad (2.1.14) \\
&= \oiint_{\partial\mathcal{D}} -\frac{1}{j\omega\rho(\mathbf{x})} \left[\hat{G}^*(\mathbf{x}_A, \mathbf{x}, \omega)\nabla\hat{G}(\mathbf{x}_B, \mathbf{x}, \omega) - \nabla\hat{G}^*(\mathbf{x}_A, \mathbf{x}, \omega)\hat{G}(\mathbf{x}_B, \mathbf{x}, \omega) \right] \cdot \mathrm{d}\mathbf{S} \ .
\end{aligned}$$

By combining (2.1.13) and (2.1.14), we get

$$\begin{aligned}
2\Re\left\{ \hat{G}(\mathbf{x}_A, \mathbf{x}_B, \omega) \right\} = \oiint_{\partial\mathcal{D}} &-\frac{1}{j\omega\rho(\mathbf{x})} [\hat{G}^*(\mathbf{x}_A, \mathbf{x}, \omega)\nabla\hat{G}(\mathbf{x}_B, \mathbf{x}, \omega) \\
&- \nabla\hat{G}^*(\mathbf{x}_A, \mathbf{x}, \omega)\hat{G}(\mathbf{x}_B, \mathbf{x}, \omega)] \cdot \mathrm{d}\mathbf{S} \ .
\end{aligned} \qquad (2.1.15)$$

Having exchanged the source and receiver in (2.1.14), we are now sampling the acoustic wavefield in the interior of $\mathcal{D}$, at the points $\mathbf{x}_A$ and $\mathbf{x}_B$. The 'sources' of the representation integral on the right-hand side are located at the boundary of $\mathcal{D}$, and del operates with respect to $\mathbf{x}$. From Equation (2.1.15) we see how correlations between GFs (recall that $f \star g \overset{\mathcal{F}}{\to} \hat{f}^*\hat{g}$) sampled at two interior points can be used to approximate their mutual GF, essentially giving the principle of seismic interferometry.

I call the right-hand side of (2.1.15) the *representation integral* since it is analogous to the representation theorem in earthquake seismology. The theorem states that displacements in the elastic domain $\mathcal{D}$ are wholly determined by displacements or tractions (or both) at the boundary of $\mathcal{D}$ (Aki and Richards 2002). The representation theorem is used, for example, to reconstruct the displacement everywhere when we know the displacements on both sides of a fault.

If we can decompose $\partial \mathcal{D}$ as $\partial \mathcal{D} = \partial \mathcal{D}_1 \cup \partial \mathcal{D}_2$ where $\partial \mathcal{D}_1$ is the traction-free and $\partial \mathcal{D}_2$ the rigid part of the integration domain, the right-hand side of (2.1.15) vanishes for the traction-free part (that is, the ground surface), so we only need to consider what remains in $\partial \mathcal{D}_2$ for the integration. This is an important result since it implies that the representation integral (2.1.15) does not necessarily have to be taken over a closed boundary.

What are, then, the two elements G and $\nabla G \cdot d\mathbf{S}$ that are correlated with each other in the representation integral (2.1.15)? Clearly $G(\mathbf{x}_A, \mathbf{x}, t)$ is the GF sampled at $\mathbf{x}_A$ due to a single (*monopole*) source at $\mathbf{x}$. Assuming that we have two such sources, with opposite signs for $q(\mathbf{x}, t)$, separated by a (small) distance $\mathbf{n}$ so that the negative source is located at $\mathbf{x}'$ and the positive source at $\mathbf{x}' + \mathbf{n}$ with $|\mathbf{n}| \ll |\mathbf{x} - \mathbf{x}'|$. Note that due to the linearity of GF with respect to $q(\mathbf{x}, t)$, the combined effect of the two monopoles is

$$\hat{G}(\mathbf{x}, \mathbf{x}' + \mathbf{n}, \omega) - \hat{G}(\mathbf{x}, \mathbf{x}', \omega) \approx \nabla' \hat{G}(\mathbf{x}, \mathbf{x}', \omega) \cdot \mathbf{n} , \qquad (2.1.16)$$

that is, the total differential of $\hat{G}$ at $\mathbf{n}$, where del operates with respect to the primed coordinates. We can interpret (2.1.16) as the pressure field due to a *dipole* located at $\mathbf{x}'$ and oriented along $\mathbf{n}$. This shows that the representation integral is fundamentally built on the correlations between monopole and dipole sources spread over the part of $\partial \mathcal{D}$ where traction does not vanish. The principle is illustrated in Figure 2.2.

2.2 Seismic interferometry equations

2.2.1 Formulation

Next, I proceed to expressing the equation (2.1.15) in a form that is actually useful for EGF retrieval, and present a generalisation for the elastodynamic case.

The representation integral (2.1.15) is simplified considerably if one considers a homogeneous medium (with constant ρ and c_p), assumes that the waves propagating outwards do not return to the integration domain, assumes that the integration domain is so large that the dipole sources can be approximated with monopole sources, and replaces transient sources with uncorrelated noise sources. These assumptions lead to the acoustic interferometry equation (Wapenaar and Fokkema 2006)

$$2\Re\left\{\hat{G}(\mathbf{x}_A, \mathbf{x}_B, \omega)\right\} \hat{S}(\omega) \approx \frac{2}{\rho c_p} \left\langle \hat{p}^{\mathrm{obs}*}(\mathbf{x}_A, \omega) \hat{p}^{\mathrm{obs}}(\mathbf{x}_B, \omega) \right\rangle , \qquad (2.2.1)$$
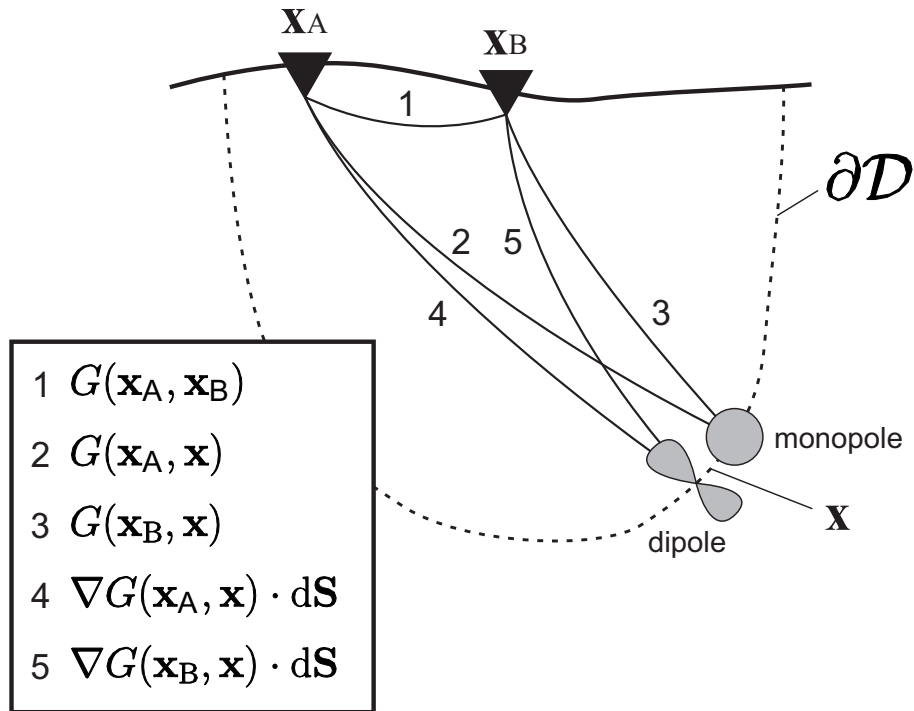
Figure 2.2: The GF between locations $\mathbf{x}_A$ and $\mathbf{x}_B$ (1) can be represented with the cross-correlations of monopole (2–3) and dipole (4–5) sources spread over $\partial\mathcal{D}$. d$\mathbf{S}$ is the normal vector at $\mathbf{x} \in \partial\mathcal{D}$, pointing outside the integration domain. Traction vanishes at free surface.

where $\hat{S}(\omega)$ is the power spectrum of the noise and $\hat{p}^{\mathrm{obs}}(\mathbf{x}_{\mathrm{A}}, \omega)$ and $\hat{p}^{\mathrm{obs}}(\mathbf{x}_{\mathrm{B}}, \omega)$ are the observed wavefields at $\mathbf{x}_{\mathrm{A}}$ and $\mathbf{x}_{\mathrm{B}}$. The angle brackets indicate spatial ensemble averaging, which for ergodic random processes is equivalent to averaging over long enough time periods. Exactly how long is 'long enough' depends on the situation, but in practical applications of the formula (2.2.1), we can postulate that the period should contain enough body-wave events that illuminate the target with as good azimuthal coverage as possible (Snieder and Sens-Schönfelder 2015).

In the elastodynamic case, we also have to consider the ability of the medium to sustain shear. This generalizes the acoustic wave equations (2.1.2) into the *elastodynamic wave equations* (Wapenaar and Fokkema 2006)

$$
\begin{cases}
j\omega\rho(\mathbf{x})\hat{\mathbf{v}}(\mathbf{x}, \omega) - \nabla \cdot \hat{\boldsymbol{\tau}}(\mathbf{x}, \omega) = \hat{\mathbf{f}}(\mathbf{x}, \omega) \\
-j\omega\mathbf{s}(\mathbf{x}) : \hat{\boldsymbol{\tau}}(\mathbf{x}, \omega) + \frac{1}{2}\left(\nabla\hat{\mathbf{v}}(\mathbf{x}, \omega) + \nabla\hat{\mathbf{v}}(\mathbf{x}, \omega)^{\mathsf{T}}\right) = \hat{\mathbf{h}}(\mathbf{x}, \omega)
\end{cases}
, \tag{2.2.2}
$$

where $\mathbf{v}(\mathbf{x}, t)$ is the velocity field, $\hat{\boldsymbol{\tau}}$ is the stress tensor, $\mathbf{s}(\mathbf{x})$ is the fourth-order compliance tensor, and $\hat{\mathbf{h}}(\mathbf{x}, t)$ is the external deformation rate density tensor. The colon stands for the double dot product, i.e., $\mathbf{s}(\mathbf{x}) : \hat{\boldsymbol{\tau}} = s_{ijk\ell}\hat{\tau}_{k\ell}$.

Without dwelling too much on the mathematical details, the interferometric solution is given by Wapenaar and Fokkema (2006) as

$$
2\Re\left\{\hat{G}_{pq}(\mathbf{x}_{\mathrm{A}}, \mathbf{x}_{\mathrm{B}}, \omega)\right\}\hat{S}(\omega) \approx \frac{2}{\rho c_p}\left\langle\hat{v}_p^{\mathrm{obs}*}(\mathbf{x}_{\mathrm{A}}, \omega)\hat{v}_q^{\mathrm{obs}}(\mathbf{x}_{\mathrm{B}}, \omega)\right\rangle \tag{2.2.3}
$$

and represents the p component of the response of the elastic system at $\mathbf{x}_{\mathrm{A}}$ due to a force source at $\mathbf{x}_{\mathrm{B}}$ oriented along q axis. Because of the elastodynamic assumption, the solution contains both P and S waves, and with wavefield separation techniques the latter one can further be separated into the horizontally polarized SH phase and the vertical-plane polarized SV phase.

2.2.2 Properties of the elastodynamic solution

It is easy to see from (2.2.3) that in the elastodynamic case, GF is a second order tensor $\mathbf{G}(\mathbf{x}_{\mathrm{A}}, t; \mathbf{x}_{\mathrm{B}}, 0) = G_{ij}(\mathbf{x}_{\mathrm{A}}, t; \mathbf{x}_{\mathrm{B}}, 0)$ that satisfies both the invariance to time shifts and the source-receiver reciprocity

$$
G_{ij}(\mathbf{x}_{\mathrm{A}}, t; \mathbf{x}_{\mathrm{B}}, 0) = G_{ji}(\mathbf{x}_{\mathrm{B}}, t; \mathbf{x}_{\mathrm{A}}, 0) . \tag{2.2.4}
$$

To derive it using seismic interferometry, we need full three-component observations of the velocity field. Using 3C geophones, we can observe the ZNE components simultaneously and, averaging over long enough time periods and applying the formula (2.2.3), it is possible to estimate the $3 \times 3 = 9$ components of the Green's tensor.

Assume now that the force source is uniaxially oriented along the unit vector $\mathbf{s}$ and the receiver is uniaxially oriented along the unit vector $\mathbf{r}$. We can express the elastodynamic wavefield due to the force source as

$$G_{i1}s_1 + G_{i2}s_2 + G_{i3}s_3 = \mathbf{Gs} \ ,$$

and since we only observe the component of this along $\mathbf{r} = (r_1, r_2, r_3)$, we can apply ordinary projection to yield the following expression as our observable:

$$
\begin{aligned}
g(t) &= (r_1, r_2, r_3) \cdot (G_{i1}s_1 + G_{i2}s_2 + G_{i3}s_3) \\
&= r_1 G_{11} s_1 + r_1 G_{12} s_2 + r_1 G_{13} s_3 \\
&\quad + r_2 G_{21} s_1 + r_2 G_{22} s_2 + r_2 G_{23} s_3 \\
&\quad + r_3 G_{31} s_1 + r_3 G_{32} s_2 + r_3 G_{33} s_3 = \mathbf{rs} : \mathbf{G} \ .
\end{aligned}
\tag{2.2.5}
$$

If during acquisition of the data the principal components were not oriented along the inline and crossline directions, we can use this formula to correct the orientation for the line's azimuth after EGF retrieval.

Consider an elementary example where the data acquisition took place in a ZNE coordinate system. To rotate the data for the ZRT orientations, we can write $\mathbf{r}_Z = \mathbf{s}_Z = (1, 0, 0)$, $\mathbf{r}_R = \mathbf{s}_R = (0, \cos\phi, \sin\phi)$, and $\mathbf{r}_T = \mathbf{s}_T = (0, \sin\phi, -\cos\phi)$ where ϕ is the inline azimuth measured clockwise from the direction of the north. Together with the projection equation (2.2.5), this gives as our derived observables

$$
g_Z(\phi) = \begin{pmatrix} 1 & 0 & 0 \\ 0 & 0 & 0 \\ 0 & 0 & 0 \end{pmatrix} : \begin{pmatrix} G_{11} & G_{12} & G_{13} \\ G_{21} & G_{22} & G_{23} \\ G_{31} & G_{32} & G_{33} \end{pmatrix} = G_{11} \ ,
\tag{2.2.6}
$$

$$
\begin{aligned}
g_R(\phi) &= \begin{pmatrix} 0 & 0 & 0 \\ 0 & \cos^2\phi & \cos\phi\sin\phi \\ 0 & \sin\phi\cos\phi & \sin^2\phi \end{pmatrix} : \begin{pmatrix} G_{11} & G_{12} & G_{13} \\ G_{21} & G_{22} & G_{23} \\ G_{31} & G_{32} & G_{33} \end{pmatrix} \\
&= (\cos^2\phi)G_{22} + \sin\phi\cos\phi(G_{23} + G_{32}) + (\sin^2\phi)G_{33} \ ,
\end{aligned}
\tag{2.2.7}
$$

and

$$
\begin{aligned}
g_T(\phi) &= \begin{pmatrix} 0 & 0 & 0 \\ 0 & \sin^2\phi & -\sin\phi\cos\phi \\ 0 & -\cos\phi\sin\phi & \cos^2\phi \end{pmatrix} : \begin{pmatrix} G_{11} & G_{12} & G_{13} \\ G_{21} & G_{22} & G_{23} \\ G_{31} & G_{32} & G_{33} \end{pmatrix} \\
&= (\sin^2\phi)G_{22} - \sin\phi\cos\phi(G_{23} + G_{32}) + (\cos^2\phi)G_{33} \ ,
\end{aligned}
\tag{2.2.8}
$$

essentially showing that we only need to compute five independent correlation pairs, G_{11}, G_{22}, G_{33}, G_{23}, and G_{32}, to be able to transform the GF from ZNE into ZRT coordinates.

Chapter 3

Study site in Polvijärvi, Finland

*Dès qu'un phénomène se manifeste, il quitte le bruit, dès qu'une apparence
surgit et point, elle se révèle en voilant le bruit.*

— Serres, Michel (1982). *Genèse*, p. 21.

3.1 Overview

The cratonized Karelian continent (see Fig. 3.1b/c) served as the cornerstone of bedrock
evolution in Central Fennoscandia during Early Proterozoic times. Archaean (4.0 Ga –
2.5 Ga) in age, it has a large number of alien blocks and at present has a deep erosion
level and shows late overprinting from Svecofennian (1.92 Ga – 1.79 Ga) crustal-shaping
processes, including extensive mafic dykes that ornament the crustal fabric in BABEL
(Baltic And Bothnian Echoes from the Lithosphere; BABEL Working Group 1990) and
FIRE (Finnish Reflection Experiment; Kukkonen and Lahtinen 2006) seismic lines. The
Central Karelia subprovince of the Karelian continent outcrops to the east of the city
of Joensuu in Eastern Finland. It comprises granite–gneisses and migmatites, is mostly
Neoarchaean (2.75 Ga) in age, and has sanukitoid (granodioritic + Mg, K, Sr, Ba) affinities.
The Archaean crust is also visible as occasional tectonic windows in the Proterozoic domains
between the cities of Outokumpu and Joensuu. (Hölttä et al. 2012)

The Outokumpu nappe complex (Nironen 2017) lies north-east of the main suture (Raahe–
Ladoga) between Karelian and Svecofennian and is essentially an allochtonous cover thrusted
on top of the Karelian continent. In Early Proterozoic times, the Karelian continent was
stretched which led to mantle uplift and formation of an intracontinental basin by 2.1 Ga.
This is coeval with the chronometrically defined Rhyacian Period at 2.3 Ga – 2.05 Ga
during which the global carbon cycle went through a large positive excursion in $\delta^{13}C$
(Lomagundi–Jatuli Excursion) and several layered complexes formed in different continents
(Ogg et al. 2016).
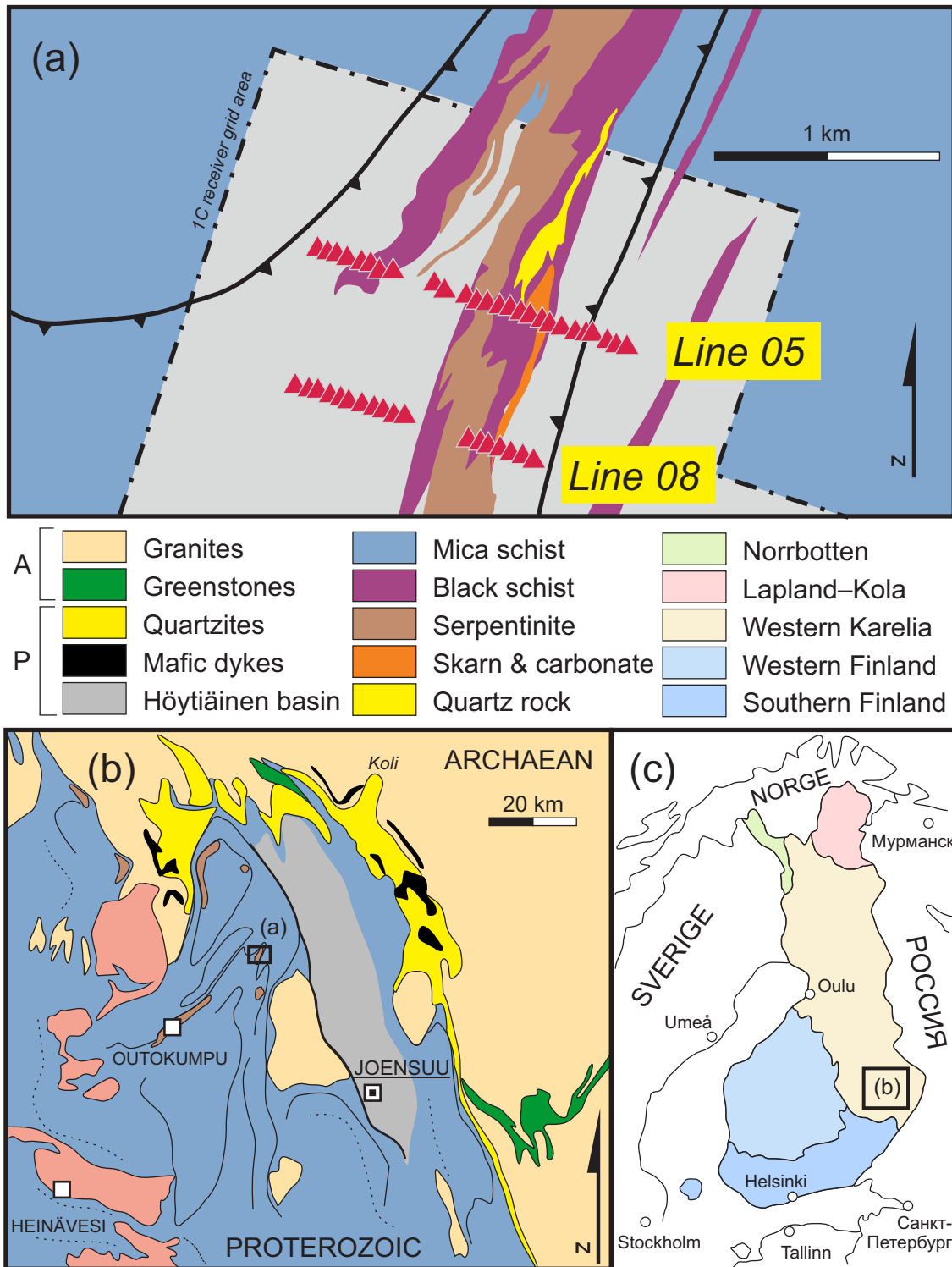
Figure 3.1: Geological map showing the regional geology of Eastern Finland and the dominant lithologies in the Kylylahti area. (a) Kylylahti synform. The OSI receivers (used in this study) are depicted as pink triangles. The COGITO-MIN 1C receiver grid area is shown using a dash-dot line and gray shading. (b) Regional map of Outokumpu nappe complex, allochtonous cover on top of the Archaean Karelian continent. A = Archaean, P = Proterozoic. (c) Index map showing the tectonic provinces of Finland. Modified from the Bedrock of Finland 1:200 000 and 1:1 000 000 datasets by the Geological Survey of Finland (2019). The original geological maps are licensed under CC BY 4.0.

Following the marginal magmatism of Jormua at 1.95 Ga, syn-sedimentary obduction related to the accretionary stage of the Svecofennian orogeny began to push newly formed sediments and tectonic slices of the oceanic crust onto the cratonic basement while the inherited extensional traits inverted. The late Viinijärvi suite (Upper Kaleva; 1.92 Ga – 1.90 Ga) turbidite, greywacke, and black schist sequences were deposited during this process in quiet conditions into relatively deep waters (Kontinen 2005).

The Outokumpu Field is a set of VHMS type mineral deposits distributed along the Outokumpu nappe margin. The Kylylahti corridor that hosts the Kylylahti deposit (see Fig. 3.1a) is located at the northeast corner of the Outokumpu Field. It is characterized by rim-altered ultramafic bodies (mantle tectonites) hosted by metasedimentary schists. Provided it was originally continuous, it was almost ~ 20 km long. Outokumpu-type ores differ from normal VHMS systems by their high Cu–Ni contents and low Pb content. Exhalative sediments and basaltic lavas are also characteristically lacking in Outokumpu area. (Kontinen et al. 2006)

The following sections outline the tectonic evolution of Eastern Finland, the petrology and petrography of Kylylahti, and the structural evolution and ore genesis theories for Outokumpu area. Finally, a brief review will be given of the petrophysical properties of the Kylylahti rocks, based on the Master thesis work by Luhta (2019).

3.2   Tectonic evolution of Eastern Finland

The *terminus post quem* of the rifting of the Karelian continent is determined by the intrusion of the ca. 2.44 Ga layered suites (Lahtinen et al. 2012) in the Siderian Period of the Palaeoproterozoic Era. Following this, the continent was torn apart over the course of hundreds of millions of years and an intracontinental sea formed by 2.2 Ga – 2.0 Ga.

Sedimentary and volcanic rocks were deposited in the intracratonic basins and their margins. These cover sequences from Karelia Supergroup (2.5 Ga – 1.9 Ga) are called the Karelian formations and they are traditionally subdivided into Sumi–Sariolan, Jatulian, and Kalevian tectofacies that represent consecutive stages of a transgressive sedimentation environment (Nironen 2017). Korsman et al. (1999) suggest two different phases of ocean opening, separated by an unknown 'orogeny'. The final opening was reflected as the marginal magmatism of Jormua about 200 km NNW of Kylylahti, aged ca. 1.95 Ga. Jormua is one of the oldest sites in the world where a full ophiolite sequence of a Precambrian oceanic basin has been preserved. The metagabbros and mid-ocean ridge type plagiogranites in Kylylahti support an analogous interpretation of Outokumpu ultramafics as ophiolites, despite the lack of the character traits of ophiolite complexes (Kontinen 2005) such as pillow lavas.

In the early stage of the polyphase Svecofennian orogeny, extension turned to compression;

however, sedimentation persisted as island arcs and microcontinents accreted to the margin of the Archaean Karelian continent. During the obduction of Outokumpu nappe at 1.90 Ga, carbonate–quartz alteration took place in peridotite rims. The resulting carbonate rocks and cherts do not have a well-defined lithostratigraphic position in the tectonic setting of Eastern Finland. Regional deformation continued after the obduction until around 1.85 Ga. The metamorphism peaked in relatively low-grade (lower amphibolite) facies conditions. In Kylylahti, the structural evolution is evident by aligned chlorite flakes in mafic rocks and tectonic banding and shearing in pyrrhotite mineralizations. (Peltonen et al. 2008; Kontinen et al. 2006)

The mafic intrusions in Outokumpu and basalts from Jormua have been suggested to have LOTI and E-MORB affinities. LOTIs are typical indicators of abnormally large heat flows in tectonic settings. The chemistry of the ultramafic units suits a pyrolitic composition. They have been variably interpreted as originally Archaean sub-continental lithospheric mantle that was refertilized during the final opening of the Outokumpu ocean. (Kontinen et al. 2006)

3.3   Regional geology of Kylylahti corridor

3.3.1   Petrology and petrography

The Viinijärvi suite comprises monotonic biotite paraschists that indicate a quiescent and non-active depositional environment, possibly mid-fan parts of a massive deep-water turbidite complex (Kontinen 2005). In the Outokumpu area, the obducted units have brought along dozens of meters thick horizons of sulphidic black schists. There are also intercalations of greywackes in the black schists, meaning that their deposition ages are overlapping. The black schists host phosphorous-rich boudinaged thin interlayers which may represent mass deaths of pelagic sea organisms. The black schists also host quartz breccia veinlets. (Kontinen et al. 2006)

Outokumpu suite rocks, as opposed to the Viinijärvi suite sediments, are coarsely divided into three main types (cf. Fig. 3.1): (1) ultramafic rocks (metaperidotitic rocks), (2) basaltic gabbros and dykes, and (3) skarns and quartz rocks.

The ultramafic rocks are thoroughly serpentinized and have dominant antigorite with carbonate porphyroblasts and coarse-grained chromite. The coexistence of antigorite with olivine implies peak metamorphic temperatures of $(520 \pm 20)\,°C$. Even higher regional metamorphic temperatures are expected in areas where talc and olivine coexist such as in soapstones (Kontinen et al. 2006).

The basaltic gabbros and dykes occur as narrow intrusions, blobs, and dykes in the ultramafic rocks. Typically they do not penetrate into greywackes or black schists but

may be found in marginal positions to the ultramafites. The metabasites are relatively low grade but have abundant chlorite flakes and often peak-metamorphic amphibole prisms. In the western part of Kylylahti complex, there is a strongly tectonized zone with coeval metagabbros and MOR-type plagiogranites. The metagabbros have ϵ_{Nd} (epsilon-neodymium) values close to zero (Kontinen et al. 2006).

The carbonate–skarn–quartz rocks have mantle-like Cr and Ni compositions, and it has been concluded that they represent listwaenite–birbirite type alteration haloes in ultramafites without any particular stratigraphic position in the sequence. Some older hypotheses speculated that they would be, e.g., exhalative cherts or sedimentary carbonate rocks but that is nowadays ruled out by mineralogical and geochemical constraints (Kontinen et al. 2006).

3.3.2 Structural evolution

In the stages named 'pre-D_1,' after Koistinen (1981), the ophiolite assemblage and greywackes were thrust as nappes at a low angle on the cover sequences of the craton. The oblique craton margin forced the units to thrust towards NE, despite a N–S-oriented regional stress field. The ultramafites show even earlier planar deformation structures related to deformation of mantle (Koistinen 2001). Koistinen (1981) unwrapped the F_1 folds and concluded that the ultramafics were originally laterally extensive 'pools' about 4 km in diameter that hosted the stratabound pyrrhotitic and pyritic ore layers.

Kylylahti deposit was discovered in 1984, three years after the doctoral dissertation of Koistinen (1981) was published, and there is little discussion about the Polvijärvi area in it. Kontinen et al. (2006) point out that the Kylylahti Cu mineralization flanks the faulted eastern contact of the thrust sheet and suggest that D_3 or older structures controlled the remobilization, if not already the initial deposition, of the ores. They thus daringly challenge the view expressed by Koistinen (1981) that the Outokumpu ores would have ended in their present positions already in F_1 folding. Kontinen et al. (2006) also infer that the carbonate-silica alteration took place before D_1 but still after the tectonic detachment of the ophiolite.

The earliest regional deformation stage D_1 is identified by large, tight-to-isoclinal recumbent folds with NE–SW-vergent fold axes that deform the original S_0 layering (Koistinen 1981). They show the greatest effect on the structural geology of the Outokumpu area and also involve overthrusting along the axial planes. The strongly developed axial plane cleavage S_1 is due to metamorphic segregation banding. The F_1 folds are sawtooth-shaped and are oriented NE–SW although no compression in this direction is recognized elsewhere in Eastern Finland. Koistinen (2001) explain this by convergence and divergence between adjacent nappe blocks as they continued their thrusting towards NE.

The D_2 stage is identified by asymmetric F_2 folding, a pervasive S_2 schistosity or crenulation,

and a very clear L_2 lineation oriented NE–SW that can be seen all across the Outokumpu nappe complex.

The D_3 stage (in Koistinen 1981, D_{2c} where c stands for 'conjugate') started by dextral sliding along the craton margin far in the south, exemplified by the massive NW–SE-oriented Heinävesi wrench lineament (see Fig. 3.1b). In Outokumpu area, this deformation stage is shown as NNE and NW conjugate directions, asymmetric F_3 folds whose axis planes are deflected 25° to 30° from S_1, and related S_3 axial plane cleavage and crenulation.

The D_4 deformation is where Koistinen (1981) associates the highest metamorphic temperatures. F_4 folds are open and asymmetric and their axes are oriented 145° to 185°. The deformation stage also includes the N-oriented linear structures NW of Sotkuma.

The later deformation stages (D_5 to D_{late}) include minor open folds but also brittle structures such as faults that today fragment the Outokumpu ore into numerous subblocks (Koistinen 2001).

3.3.3 Ore genesis

The mineralization is located on the subvertical eastern flank of the Kylylahti synform. The massive to semimassive mineral lenses are found between carbonate-skarn-quartz rocks and black shales but they occasionally intrude into the black shales. Parallel to the massive lenses, there is a zone of skarn-hosted sulphide disseminations, veins, and small lenses. The disseminated mineralization grades out but can be delineated by the 1000 ppm Cu isopleth, as was done in the cross sections of Kontinen (2005). At least three separate subdomains are recognized in the deposit: the shallow northern lenses ('Wallaby'), the deep ore ('Wombat') which plunges at a greater angle down to ~ 900 m, and the 'Gap' domain between the other two and overlying 'Wombat'. The mineralization in Kylylahti, like Outokumpu style massive sulphide deposits in general, is characterized by high Co/Ni and Cu/Ni ratios.

The Outokumpu sulphide mineralization is these days considered polygenetic. The massive copper proto-ore (1.95 Ga) is interpreted to have been deposited in a hydrothermal enrichment process in the spreading stage of an ocean but, however, not in an exhalative process (Kontinen et al. 2006). The nickel-cobalt disseminations (1.91 Ga) are originally tectonic and they originate in the ultramafites whose margins were subjected to S-rich metasomatizing fluids (Peltonen et al. 2007). Outokumpu is not a VHMS deposit in the strictest sense due to the high Ni content. However, the Cyprus-type ophiolite-associated VHMS deposits have sometimes been proposed as analogues for it (Papunen 1987).

The main ore minerals of the Kylylahti deposit are pyrite+pyrrhotite+chalcopyrite±sphalerite. Coarse-grained quartz is a typical gangue mineral. Cobalt is present in cobaltite, pyrite, and pentlandite (Kontinen 2005). Typical ore fabrics include layered primary pyrite ore,

remobilized massive pyrrhotite ore, pyrrhotite ore with tectonic banding and occasional fragments of quartz rocks, and skarn-hosted sulphide disseminations, veinlets, and small lenses. Finely banded pyrite has often grown into small spherules and may be replaced by coarse-grained pyrrhotite and chalcopyrite (Kontinen et al. 2006).

3.3.4 Controversies and other possible interpretations

As noted above in section 3.3.2, Kontinen et al. (2006) suggest that the Outokumpu ores may have directly been deposited in boundary faults after D_3 and that they may have not been involved in the D_1 folding at all. This is in contradiction with the conclusion by Koistinen (1981) that the original stratabound ore layers were elongated into thin ruler-shaped ribbons in early L_1 and isoclinal folding. Their argument is based on cross-cutting relations between ore hosts and F_1 structures. However, Kontinen et al. (2006) soften their argument for the final GEOMEX Outokumpu model they propose and suggest that the copper and nickel proto-ores may have only remobilized in the regional deformation between 1.90 Ga to 1.85 Ga.

Kontinen et al. (2006) also raise the question whether the serpentinites unquestionably represent MORB source mantle / depleted asthenospheric mantle following the complete breakup of the subcontinental lithospheric mantle (SCLM) or whether they actually were partly derived from the ancient, Archaean SCLM. They note that in the Kylylahti area, some of the zircons in metabasites are aged over 2.2 Gyr and that the serpentinites have a harzburgitic geochemistry, both supporting the Archaean interpretation.

Although the geoscientific debate of plate-triggered versus plume-triggered continent breakups is far from settled, Kontinen et al. (2006) infer that the breakup of the Karelian craton was superplume-triggered and even call the plume signature 'obvious' (p. 129). In brief, the dispute concerns whether lithospheric extension and craton breakup can follow from postulated massive 'hot' mantle upwellings (plumes; see Condie et al. 2001) or whether they can be directly or indirectly accounted for by 'top-down' plate tectonic processes (Foulger 2011). The plume explanation has been favoured in Kontinen et al. (2006) based on the following observations:

- High metal contents in Outokumpu black shales (possibly reflecting increased productivity and increased hydrothermal activity),

- LOTI in Outokumpu, reflecting high temperature gradients,

- high Nb_N/La_N in Jormua E-MORB, often taken as characteristic of modern plume magmas,

- positive ϵ_{Nd} values between +0 to +3 in the Jormua–Outokumpu metabasites, and

- evidence of plume-related mafic magmatism in the remote Onega area, Russia, at

2.0 Ga, and similar evidence in Koli, Northern Karelia.

Their argumentation is countered by the fact that MORB geochemistry varies naturally a lot and it is not universally agreed what the difference between 'normal' and 'enriched' MORB is (Anderson 2007; Fitton 2007). Besides, it is quite far-reaching to draw conclusions about the tectonic circumstances of the time just based on an increase in pelagic basic productivity since it depends, among other factors, also on oceanic upwellings driven by global wind patterns and the fertilization of the ocean in nutrients, which in turn is connected to high continental erosion rates.

3.4 Petrophysical properties

3.4.1 Laboratory measurements

In her MSc work, Luhta (2019) determined the petrophysical properties of core samples and hand samples from Kylylahti area. The petrophysical variables considered were density, porosity, magnetic susceptibility, NRM intensity, inductive and galvanic resistivity, chargeability, and P-wave velocity (Luhta 2019). The core samples were divided into 13 lithological groups (see Fig. 3.2) based on visual determinations on the drill core inventory.

The main parameter dictating whether a target can be observed in a reflection survey or not is its seismic impedance (product of density ρ and seismic velocity c, $Z = \rho c$) contrast with the surroundings, quantified by the reflection coefficient

$$R = \frac{Z_2 - Z_1}{Z_2 + Z_1} = \frac{\rho_2 c_2 - \rho_1 c_1}{\rho_2 c_2 + \rho_1 c_1} , \qquad (3.4.1)$$

where the subscripts 1 and 2 stand for two contrasting lithologies. Following Salisbury et al. (1996), Luhta considered that a reflection coefficient of 0.06 between two lithologies is enough to produce systematic reflected signals from the interface between them.

The seismic impedance of the massive to semimassive sulphide mineralizations (above $23 \times 10^6 \, \text{kg} \, \text{s}^{-1} \, \text{m}^{-2}$) differs so greatly from other sample types (generally less than $20 \times 10^6 \, \text{kg} \, \text{s}^{-1} \, \text{m}^{-2}$) that they can be expected to be detectable in reflection seismic surveys ($R > 0.07$). A pronounced impedance contrast will probably also be observed between rocks of the Outokumpu association and Viinijärvi suite schists. Soapstones can cause internal reflectivity within serpentinites (Luhta 2019). However, it should be noted that the P-wave velocities showed a large scatter and, for example for massive ore samples ($N = 13$), the standard deviation of the measurements was $0.6 \, \text{km} \, \text{s}^{-1}$ or almost 10 % of the measured value.

As the background work for the seismic forward modelling on real lithologies, the original 13 lithological groups were reduced to four main types (see Table 3.1) based on their seismic

velocities and densities. The subdivision followed here is: (1) Kalevian schists (KAL), or Viinijärvi suite sulphide schists and mica schists (corresponding to black schist, sulphite rich black schist, and mica schist in Luhta 2019), (2) Outokumpu ultramafic rocks (OUM), or serpentinites and soapstones (corresponding to serpentinite and talc carbonate rock in Luhta 2019), (3) carbonate-skarn-quartz rock alteration haloes in ultramafics (OME), or marble-like dolomites, quartz rocks and tremolite–diopside skarns that are metasomatic alterations of the previous group (corresponding to skarn, tremolite skarn, quartz rock, carbonate rock, and chlorite schist in Luhta 2019), and (4) massive to semimassive sulphide mineralization (MS/SMS) (corresponding to massive ore and semimassive ore in Luhta 2019). Each of these main types is modelled with the most representative member of the original 13 groups (see Table 3.1). In particular, Kalevian schists were assigned the average velocity of sulphide-rich black schists because these are most commonly found in contact with the ultramafics.
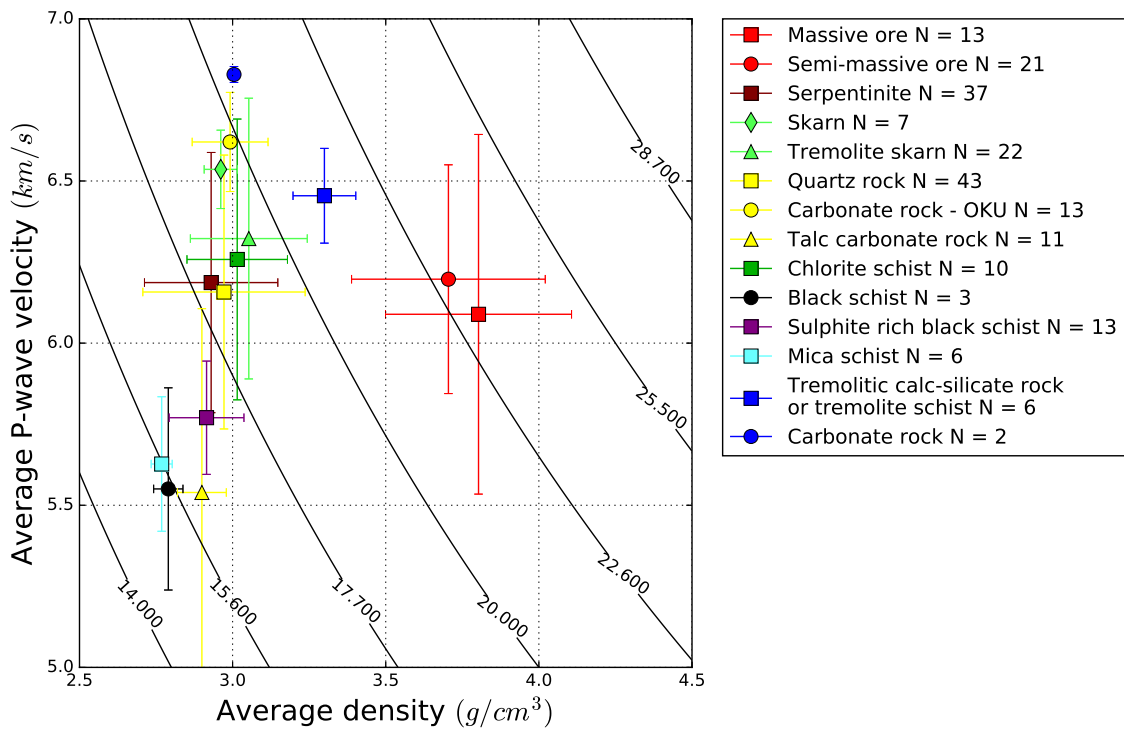
Figure 3.2: P-wave velocity and density measurements for Kylylahti samples ($N = 216$) from the MSc work by Luhta (2019) (reproduced with permission). The sample standard deviations are indicated in the figure with error bars. The black curves on the background are isolines of acoustic impedance; the difference between adjacent lines corresponds to a reflection coefficient of 0.06.

Table 3.1: P-wave velocities and densities for the four main lithologies in Kylylahti determined in laboratory conditions. The OME category is modelled with tremolite skarn, OUM with serpentinite, and KAL with sulphide-rich black schist of Luhta (2019).

Lithology	Modelled with	N	v_p (m/s)		ρ (kg/m^3)	
			avg.	std.	avg.	std.
Kalevian schists (KAL)	SULBS	13	5770	170	2915	122
Outokumpu ultramafics (OUM)	SP	37	6190	400	2930	218
Metasomatically altered rocks (OME)	TRESKA	22	6320	430	3053	191
Massive to semimassive sulphides (MS/SMS)	MS	13	6090	550	3803	304

3.4.2   Towards a physical model of subsurface

Seismic forward modelling with the finite-difference approach is based on solving either the acoustic (2.1.2) or elastic (2.2.2) wave equation on a staggered grid. The regional architecture of the shallow part of Kylylahti is well known due to long history of drilling in the area, and the mining operator Boliden possesses a 3D geological model of the volume units and lithological horizons in the subsurface. The model provides the geometry of the volume units which can then be populated with average P-wave velocities and densities from petrophysical measurements. Each volume unit in Boliden's voxet model was assigned a seismic velocity from Table 3.1. The density distribution was independently obtained from the 3D interpolation of laboratory density measurements on all available borehole data.

Two slices of the geological model were prepared across the strike of the Kylylahti syncline along the OSI receiver lines (see Fig. 3.3 and 3.4). The inter-profile separation was around 600 m, and the orientations of the slices were WNW–ESE. Both models extend to 1.3 km depth and have a 2 m spatial discretization interval. A slight Gaussian blur was applied to the slices in 2D so that they would have a less 'blocky' appearance. The greatest disadvantage of the model is that it does not incorporate the alterations of peridotite into soapstones. The soapstones were intentionally left out in order to keep the model simple so that other relevant high-amplitude information (such as the contacts to the sulphide mineralization) would be clearly visible in the FD modelling outputs.

The northern slice (Fig. 3.3) shows the Gap and Wombat subdomains at model depths between 300 m and 500 m, corresponding to true depths (below ground level) between 400 m and 600 m. The mineralization is shown as a narrow, upright sliver in the slice, so qualitatively it can be expected to reflect like a single, isolated diffractor considering wavelengths typically used in surface seismic surveys. The geology of the southern slice (Fig. 3.4) is less known, but if the ore extended to the southern profile, it would intersect this at a model depth of ~ 900 m (true depth 1000 m), assuming that the mineralization

strikes towards SSW and plunges at 40°. However, the first reflected arrivals do not come from right below but from the updip side, in this case from the NW side of the profile, from apparent depths of $\sim 700\,\mathrm{m}$ (true depth $600\,\mathrm{m}$).

It should finally be noted that the geological model's extent is also laterally narrower than the OSI spread, and some receivers in the spread are outside of the area where current geological knowledge extends.
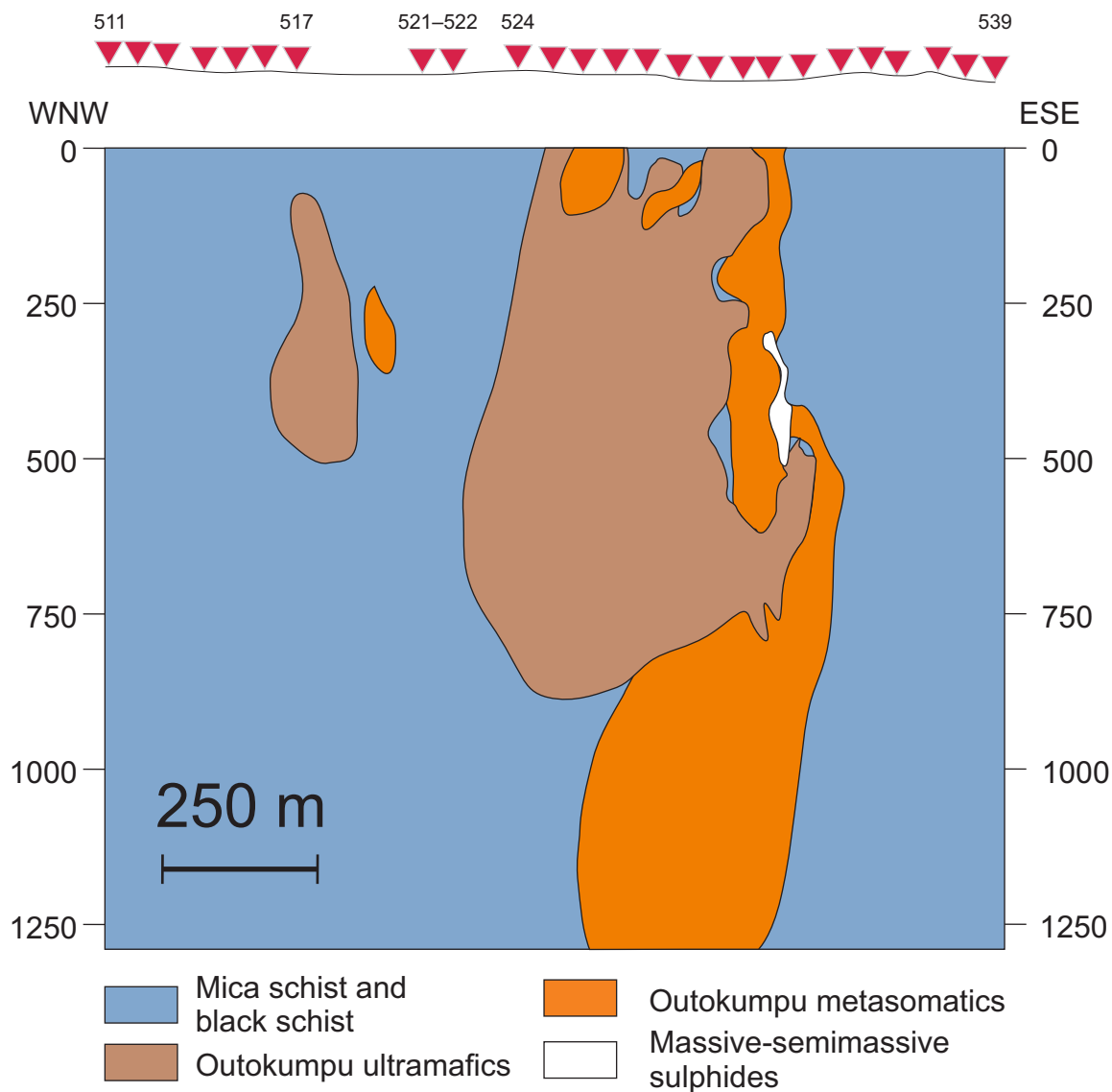
Figure 3.3: Slice across the lithological volume model of Boliden representing the northern OSI line (05). The topography of the ground surface does not vary much. One receiver (510) is left outside of the profile area. The strike of the profile is 108°. The mineralization plunges towards the viewer.
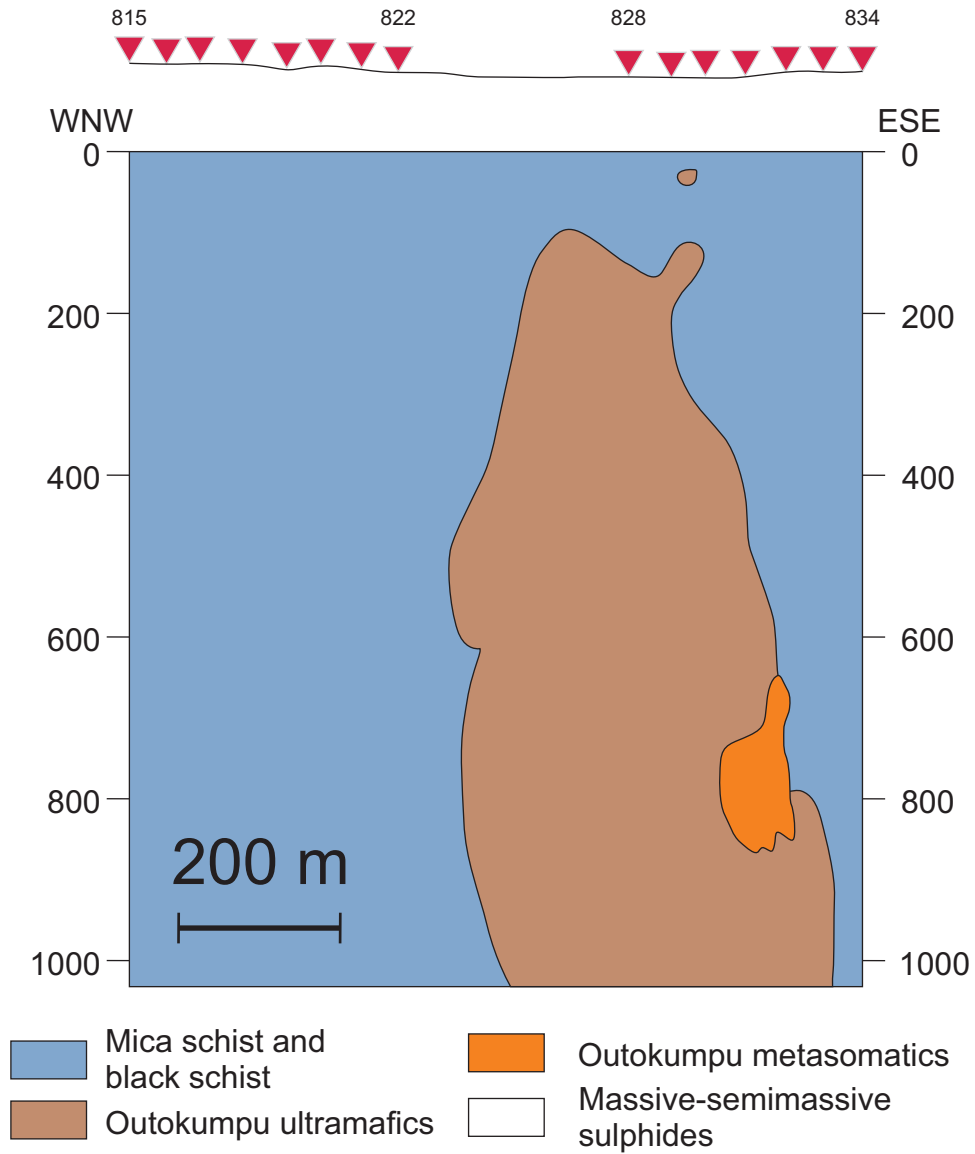
Figure 3.4: Slice across the lithological volume model of Boliden representing the southern OSI line (08). The topography of the ground surface does not vary much. Three receivers (812–814) are outside of the profile area. The strike of the profile is 108°. The Wombat mineralization is not known to extend to this area, but if it did, it should be encountered at model depths of $\sim 900\,\mathrm{m}$ or right where the OME alteration halo is in this profile.

Chapter 4

Development of workflow for 3C SI

> *Nous n'entendons jamais si bien ce que nous nommons bruit de fond qu'à la mer. Ce brouhaha tranquille ou véhément semble établi là pour l'éternité.*
>
> — Serres, Michel (1982). *Genèse*, p. 20.

4.1   Benchmarking SI with synthetic data

Before working with data retrieved in field conditions, the performance of SI can be evaluated by setting up a synthetic reference experiment (cf. Thorbecke and Draganov 2011) where sources are spread in a systematic fashion around the domain of the representation integral (2.1.15) or, preferably, in the stationary phase regions of the given receiver spread (Snieder and Sens-Schönfelder 2015).

This section illustrates how the synthetic reference experiment was prepared, what kind of features the modelled wavefields contain, and how the retrieved 2D seismic reflection sections compare with the geological models used to create them (Figs. 3.3 and 3.4). In the next section (4.2), the CTBTO/OSI data and their characteristics are described. In section 4.3, the 3C SI approach developed for the CTBTO/OSI data is described and the algorithms behind the implementation are illustrated in text and reproduced in pseudocode.

4.1.1   General conditions

The FD code `fdelmodc` by Thorbecke and Draganov (2011) was used to create data for a synthetic SI experiment over the Northern and Southern lines (Figs. 3.3 and 3.4). The code solves the acoustic wave equation (2.1.2) in 2D by approximating the derivatives by FDs.

The FD simulation needs a small enough time step to converge numerically, or else an instability will form and propagate, blowing up the numeral range of the modelling grid. In the case of `fdelmodc`, the condition of numerical convergence can be expressed as

$$\Delta t < \frac{0.606 \Delta x}{c_{\max}} \tag{4.1.1}$$

where $c_{\max}$ is the maximum seismic wave speed in the model, Δt is the time step and Δx is the spatial discretization interval. Since the models described earlier (see Figs. 3.3 and 3.4) have $\Delta x = 2\,\mathrm{m}$ and $c_{\max} = 6.3\,\mathrm{km\,s^{-1}}$, Δt needs to be smaller than $0.19\,\mathrm{ms}$. The time step was therefore chosen to be $\Delta t = 0.15\,\mathrm{ms}$.

The `makewave` utility by Jan Thorbecke was used to generate a source wavelet for the forward modelling. The wavelet was the first derivative of a Gaussian

$$\hat{s}(2\pi f) = \frac{f}{\sqrt{2}f_{\mathrm{p}}} \exp\left(-\frac{f^2}{2f_{\mathrm{p}}^2}\right) \tag{4.1.2}$$

whose peak frequency f_{p} was selected in a way that at $f = f_{\max} = 125\,\mathrm{Hz}$ (Nyquist frequency for data sampled at $250\,\mathrm{Hz}$), $\hat{s}(2\pi f)$ would be attenuated by $-40\,\mathrm{dB}$ from the peak value (i.e., to $1\,\%$). This happens at

$$0.01 \cdot \frac{1}{\sqrt{2}} \exp\left(-\frac{1}{2}\right) = \frac{f_{\max}}{\sqrt{2}f_{\mathrm{p}}} \exp\left(-\frac{f_{\max}^2}{2f_{\mathrm{p}}^2}\right) \Rightarrow f_p \approx 35\,\mathrm{Hz}\ .$$

The wavelet is illustrated in time and frequency domains in Figure 4.1.

4.1.2   Modelled wavefield

The `fdelmodc` modelling code was run in the acoustic scheme. The total modelling time was $4.0\,\mathrm{s}$, and the virtual receivers were placed on the top boundary of the model every 50 meters. The receivers were sampling the wavefield at a $2\,\mathrm{ms}$ sample rate, but before conventional 2D processing, the synthetic data were downsampled to $250\,\mathrm{Hz}$ since the real OSI data were also processed at that sampling rate. The left, right, and bottom boundary of the model were equipped with perfectly matched layer (PML) boundary conditions (Thorbecke and Draganov 2011) to suppress reflections from side and bottom. The top boundary had a free boundary condition.

Two modelling setups were used for preparing data for seismic interferometry (see Fig. 4.2):

- Northern line, sources placed every $10\,\mathrm{m}$ along the verticals $x = 200\,\mathrm{m}$ and $x = 1250\,\mathrm{m}$ and the horizontal $z = 1000\,\mathrm{m}$, giving a total of 308 forward-modelled source gathers.

- Southern line, sources placed every $10\,\mathrm{m}$ along the verticals $x = 200\,\mathrm{m}$ and $x = 680\,\mathrm{m}$ and the horizontal $z = 1000\,\mathrm{m}$, giving a total of 251 forward-modelled source gathers.
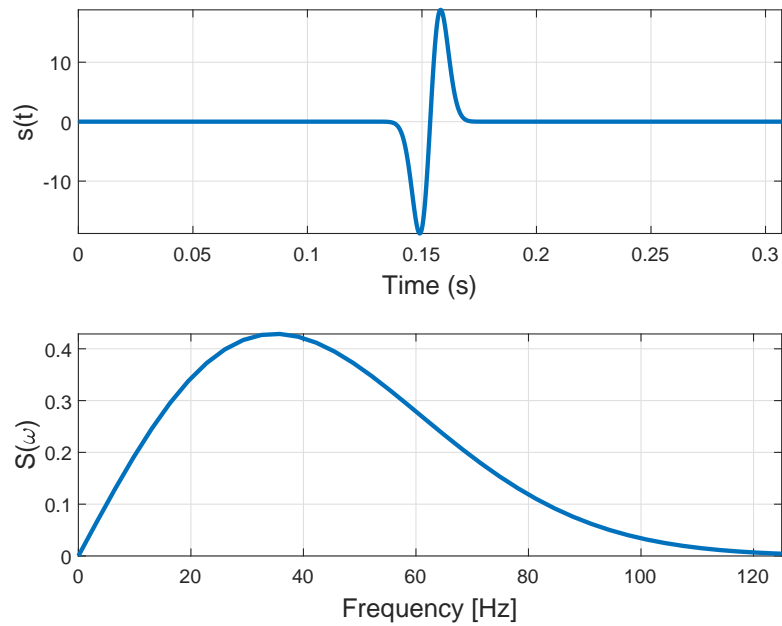
Figure 4.1: The 1$^{\text{st}}$-derivative Gaussian wavelet in time and frequency domains, used for seismic forward modelling on the OSI lines. The peak frequency is at $f_p = 35\,\text{Hz}$.
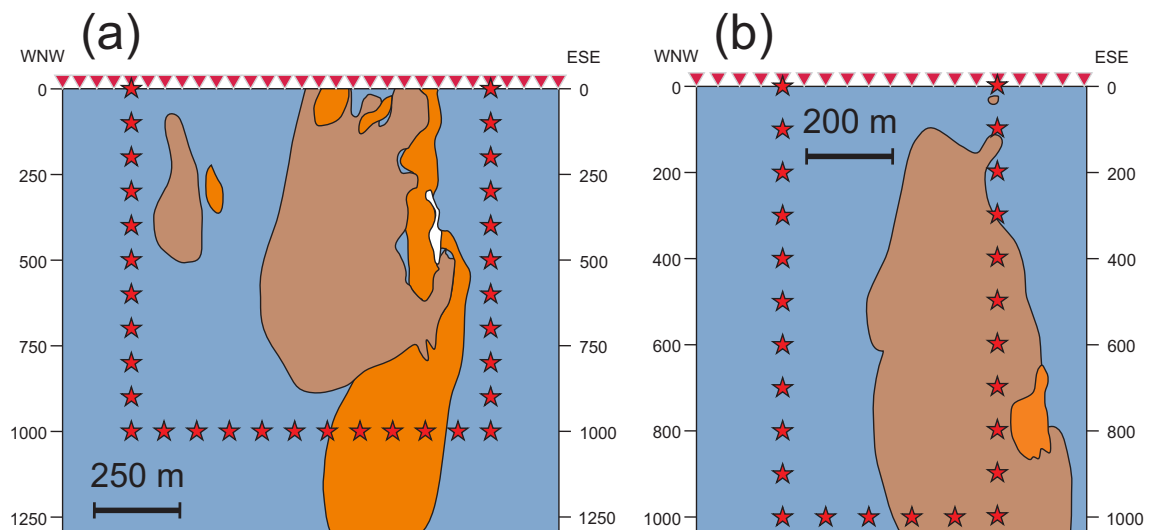
Figure 4.2: The two modelling setups used for generation of data for seismic interferometry. The locations of virtual receivers are indicated with triangles, and the locations of sources are indicated with stars. For clarity, only every tenth source is drawn. (a) Northern line, with sources restricted between $x = 200\,\text{m}$ and $x = 1250\,\text{m}$. (b) Southern line, with sources restricted between $x = 200\,\text{m}$ and $x = 680\,\text{m}$.
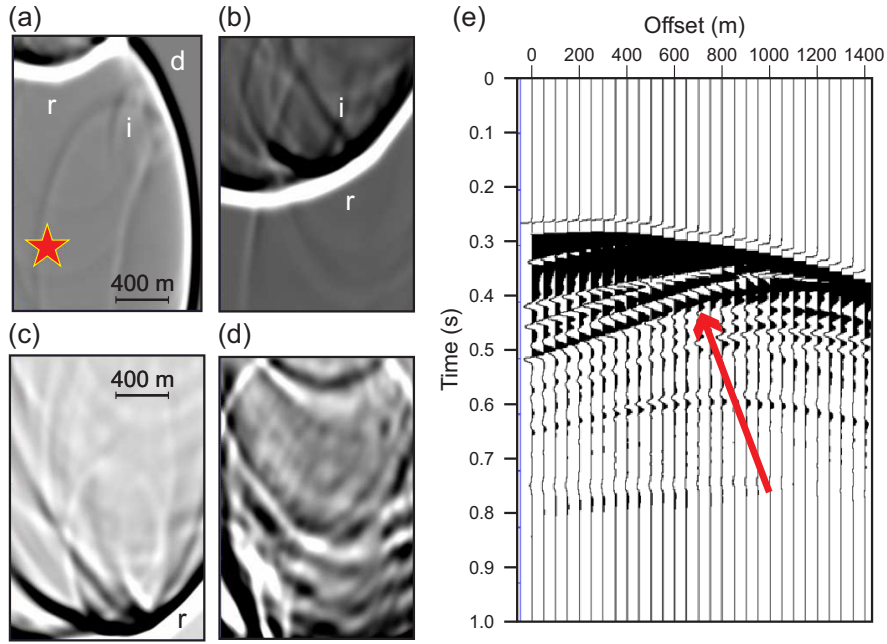
Figure 4.3: Northern line. (a–d) Snapshots of the pressure wavefield generated by a source at $x = 200\,\text{m}$, $z = 1000\,\text{m}$, sampled at $t = 0.3\,\text{s}$, $0.4\,\text{s}$, $0.5\,\text{s}$, and $0.6\,\text{s}$, respectively. d = direct arrival, r = ground surface reflected wave, i = internal reflections. (e) Shot gather as recorded on the surface receivers. The reflection due to the orebody is indicated with an arrow.

Snapshots of P-wavefield propagation for the model setup on the Northern line is shown in Figs 4.3a–d, following the activation of a single source at 1 km depth. The associated shot gather is shown in Fig. 4.3e. The reflected patterns are fairly complex, but the ore-associated reflections are easy to distinguish and have been indicated with an arrow in Fig. 4.3e.

4.1.3   SI with synthetic data

The next step in the study was to retrieve the EGFs from the synthetic active data using the seismic interferometry equation (2.2.1) and process the resulting virtual shot gathers as 2D reflection seismic lines. In practice, this was implemented by using each receiver in turn as a virtual source ($\mathbf{x}_B$) and estimating the GF between it and any other receiver ($\mathbf{x}_A$) with the sum $\sum_{i=1}^{N} v_{z,i}(\mathbf{x}_A) \star v_{z,i}(\mathbf{x}_B)$, where i iterates over the N synthetic sources. Since the top of the model domain has a free boundary condition, pressure $p(\mathbf{x}, t)$ vanishes there, and the vertical component of velocity $v_z(\mathbf{x}, t)$ needs to be used instead. Note that even though the synthetic data is retrieved from forward modelling, the SI implementation itself does not use any prior information about the spatial coverage of the sources or their frequency distribution. This implementation is an example of event-driven 'selective stacking' (Draganov et al. 2013) where the original traces are known for sure to contain

Table 4.1: Processing sequence for the synthetic seismic interferometry reference experiment. All stages were applied using Seismic Unix by the Colorado School of Mines.

Stage #	Operation	Parameters
1	Arranging into CMP gathers	
2	BP filtering	30–40–110–125 Hz
3	Geometrical spreading correction	$t^{1.2}$
4	Trace normalization	200–400 ms
5	Wiener filtering	lag 22–38 ms, applied between 50–600 ms
6	BP filtering	30–40–110–125 Hz
7	Trace normalization	200–400 ms
8	NMO + stacking	$v_P = 5900 \, \text{m s}^{-1}$
9	BP filtering	30–40–110–125 Hz
10	Trace normalization	200–400 ms
11	Stolt migration	$v_P = 5900 \, \text{m s}^{-1}$
12	BP filtering	30–40–110–125 Hz
13	Trace normalization	200–400 ms
14	t–z conversion	$v_P = 5900 \, \text{m s}^{-1}$

body-wave energy.

After EGF retrieval, the shot gathers were subjected to conventional 2D processing with the open-source seismic utilities package Seismic Unix[1]. The synthetic survey had a common midpoint (CMP) interval of 25 m and a maximal fold (how many times the same depth point has been sampled) of 50. The processing sequence and the parameters used are summarized in Table 4.1.

Line 05 (Northern line)

The stacked and migrated sections of the synthetic reference SI experiment for the Northern line can be seen in Fig. 4.4. The stack in Fig. 4.4a shows a set of three thick parabola-like reflective packages, centered at CMPs 15, 30, and 42. The deconvolution stage (Wiener filtering), whose purpose is to compress the source wavelet and reduce ringing in the prestack stage, did not manage to compress the reflective packages very much. Comparing the migrated section in Fig. 4.4b with the original velocity model (Fig. 3.3), we see that the shallow body on the WNW side of the profile corresponds to the reflector between CMPs 10 to 20. The deepest, synform-shaped package at approximately CMP 30 would be the curved bottom of the OUM unit. The inner structure of the area where the mineralization would be expected is lost in the migrated image. Instead, there is uniform high reflectivity

---
[1]http://www.cwp.mines.edu/cwpcodes/index.html

between ~ 50 ms to 200 ms.

Line 08 (Southern line)

The stacked and migrated sections of the synthetic reference SI experiment on the Southern line can be seen in Fig. 4.5. The stack in Fig. 4.5a shows a shallow diffraction parabola at CMP 25, and a thick subhorizontal reflector between 200 to 300 ms that undulates slightly and bifurcates towards WNW. In the migrated image Fig. 4.5b, the parabolae collapse into thick reflective bodies where internal structure cannot be distinguished. The three areas with elevated reflectivity (CMPs 17, 25, and 27) correlate with the folded left side of the OUM body, curved top surface of the same unit, and the OME occurrence buried between 700 to 800 m.

4.2   OSI data description

The 45 OSI receivers were recording continuously between 11 August 2016 and 15 September, 2016 (Julian days between 224 and 259). The station coordinates and elevations are listed in Appendix B. The receivers were LE-3Dlite -type seismometers by Lennartz electronic GmbH with a lower cut-off frequency of 1 Hz. The seismometers were connected to RefTek 130 dataloggers and planted by the CTBTO/OSI team in holes 30 cm to 40 cm deep. One of the stations was mounted on solid rock. The seismometers were each part of Seismic Aftershock Monitoring System (SAMS) mini-arrays (Gestermann et al. 2016) which also include 1C receivers. However, only the three-component system was in use.

The continuous data had been converted to MSEED in 24 h windows and a sample rate of 2 ms by the CTBTO/OSI team. The total volume of the data amounts to over 377 GB and the traces have only minor maintenance breaks. Some receivers in the spread have timing errors that often are related to data gaps. This especially affects receivers 513, 817, 819, and 834. Walter et al. (2018), who originally discovered these inaccuracies, also note that the receivers 517 and 539 were deployed with flipped horizontal components in a way that the east component is actually pointing to the west and the north component is pointing to south.

4.3   OSI data reductions

4.3.1   Mapping the alternative ways of SI processing

The Ambient Noise Seismic Interferometry (ANSI) workflow by Draganov et al. (2013) is the prime reference to which other exploration-scale SI workflows may be compared to. It was piloted on data collected in the Sirte Basin in Libya, comprising 11 h of seismic noise. In brief, the ANSI workflow for retrieving virtual source gathers consists of: (1) bandpass
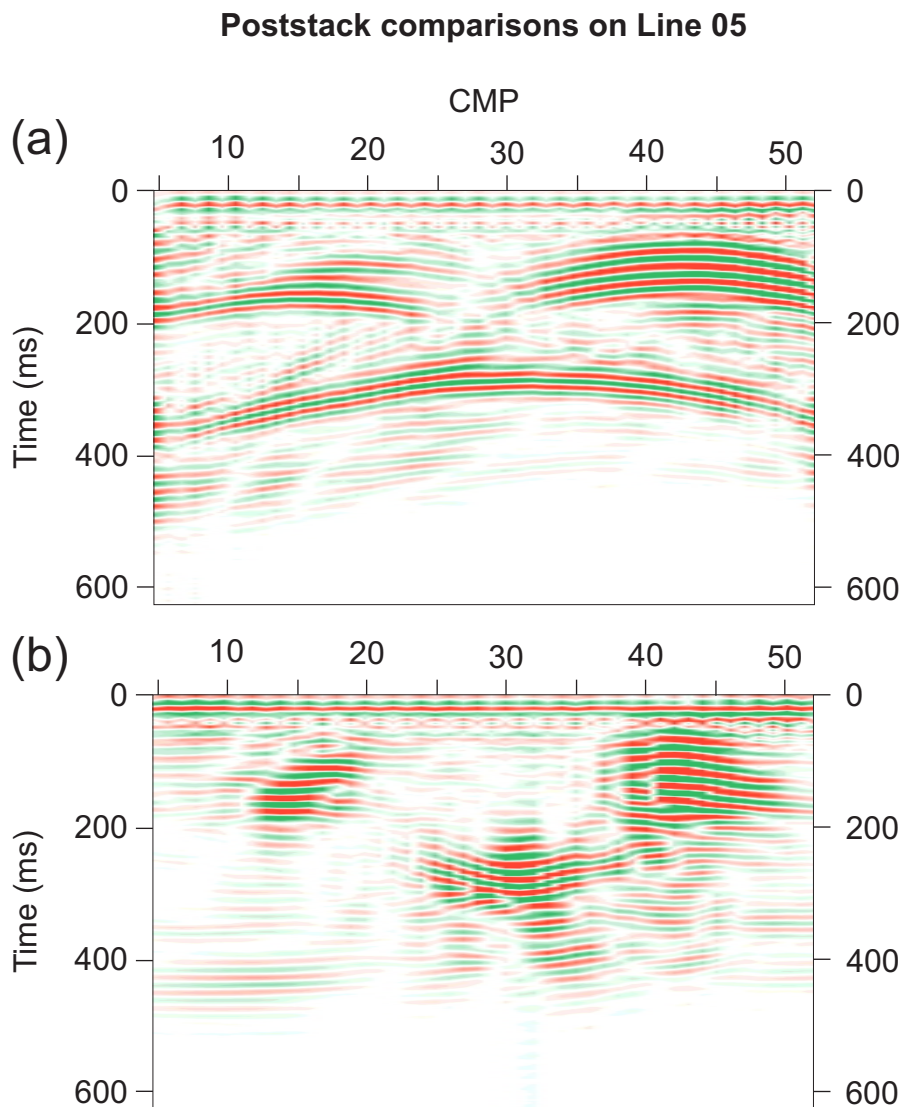
Figure 4.4: (a) The result after NMO correction and CMP stacking performed on synthetic SI data for the Northern line. Despite deconvolution, the three reflective packages appear either moderately or very thick and it is difficult to see any internal structure in them. (b) Stolt migration of the stacked section shown in Fig. (a). The deepest reflector appears synform-like and is result from migration of the 'bow-tie' shape in the top figure.

Poststack comparisons on Line 08
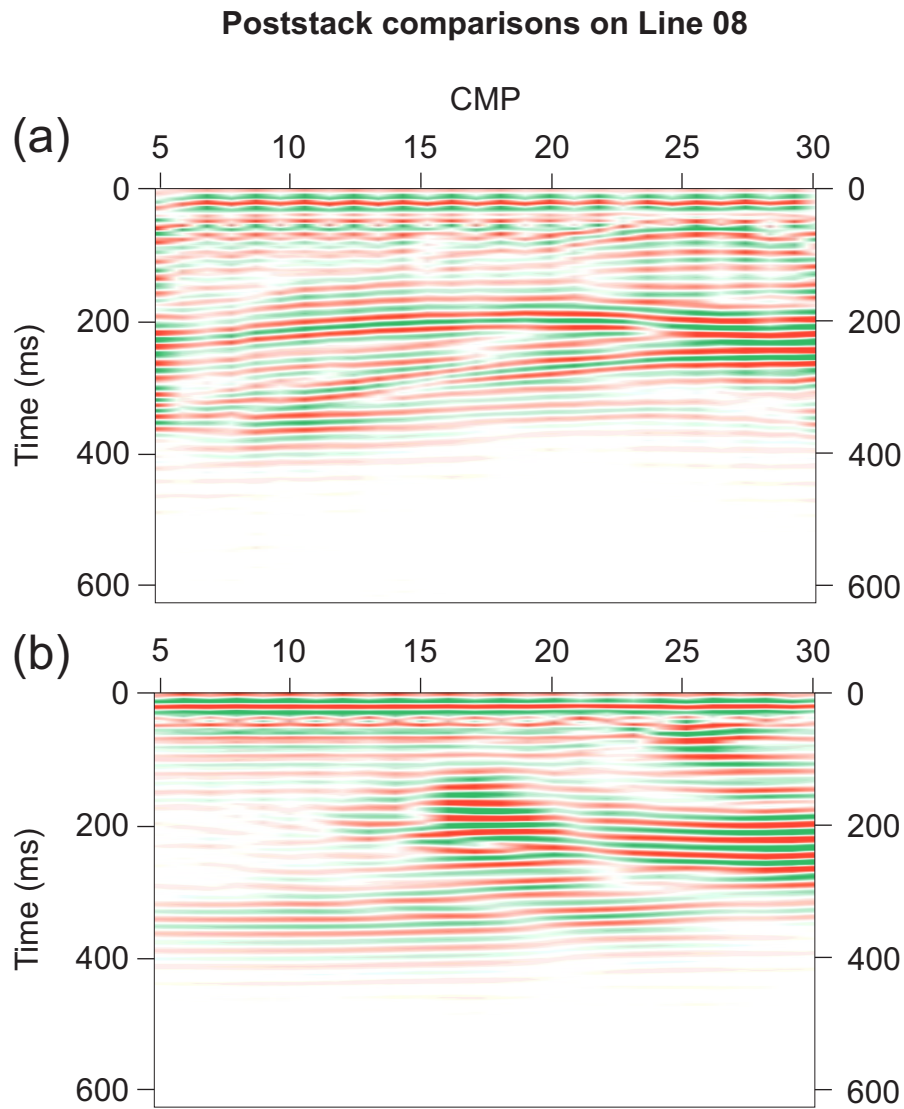
Figure 4.5: (a) The result after NMO correction and CMP performed on synthetic SI data for the Southern line. There seems to be a shallow parabola-like event at CMP 25. The horizontal curved event is almost parallel with the horizontal at 200 ms. Beneath it, there is another event that is more rapidly dipping towards WNW. (b) Stolt migration of the stacked section shown in Fig. (a). A bright package is imaged right between CMPs 15 to 20 and appears to be separated by a discontinuity from the subhorizontal reflectors to its left. The shallow event at CMP 25 is even clearer than in panel (a).

filtering for focusing only on 'useful energy', that is, the spectral bands where the body-waves are hypothesized to lie, (2) f–k filtering for further suppression of surface-waves, (3) normalization of the noise panels in time so that big events would not dominate the results, (4) cross correlation of the master trace (virtual source) with auxiliary traces (virtual receivers), (5) stacking of correlated panels, (6) deconvolution with the estimated source autocorrelation function, (7) summation of causal and acausal parts. Draganov et al. (2013) apply the ANSI workflow both for all noise panels (noise-driven approach) and only those panels where body-wave energy has been identified in beamforming analysis (event-driven approach). They conclude that both approaches yield comparable images of subsurface, but event-driven approach may be more useful especially if velocities of the subsurface are unknown. Draganov et al. (2013) could not find out what the source of their body-waves was, but they use slowness considerations to propose that the events originate in crustal phases.

Chamarczuk et al. (2018) modify the ANSI approach into the Mineral Exploration Seismic Interferometry (MESI) workflow by locating the subsurface sources (that are abundant in an active mine area such as Kylylahti), and selectively stacking over stationary phase regions that are known to have the highest contribution for EGF retrieval (e.g., Snieder and Sens-Schönfelder 2015). The motivation behind these modifications is to maximize the information content in the noise panels before stacking. On the other hand, the MESI approach is more event-driven than the ANSI approach of Draganov et al. (2013), and the stability of the retrieved EGFs is countered by the increased processing cost.

In surface-wave studies using ambient noise, two methods of data treatment are sometimes applied to attenuate the effect of disturbing transients and to equalize the spectral content of traces and to reduce the effect of coloured sources: sign-bit normalization (SBN) in the time domain and spectral whitening (SW) in the frequency domain. SBN is an aggressive non-linear method for removal of transients where each sample x in a noise trace is replaced by $\text{sgn}(x)$ in the time domain, where sgn is the signum function. Although all amplitude information is discarded in SBN, it is known to increase the SNR in many acoustic laboratory experiments (Bensen et al. 2007) and in a range of seismological applications (e.g., Cupillard and Capdeville 2010; Quiros et al. 2016). SW refers to the equalization of spectral amplitudes in a predetermined frequency band. The straightforward way of doing this is to divide each sample $x + jy$ in the Fourier domain with its modulus $\sqrt{x^2 + y^2}$, and taper the spectrum outside the frequency band of interest. The benefit of these two methods is that they are flexible and easy to implement. The possible shortcomings of the methods are that they can have a negative impact on the convergence of SI (which should be studied on a case-to-case basis), and that their performance in an exploration context is not exhaustively analysed yet.

For this thesis, I chose to implement a noise-driven approach where the decimated 24 h

traces are spectrally whitened, sign-bit normalized, and then correlated component- and station-wise with each other in sliding windows of 60 s. The implementation needed to be flexible enough to allow switching the SW and SBN stages on or off, to be able to test between whitened vs. unwhitened cross correlations and sign-bit normalized vs. unclipped correlations. The correlation was implemented in the Fourier domain with the coherency operator $f \star g \leftrightarrow \hat{f}^* \hat{g}/(|\hat{f}||\hat{g}| + \epsilon)$ where $\epsilon = 0.01$ ensures the stability of division when the spectral energy density in a frequency band is very low. The acausal and causal parts of the traces were summed by zeroing the imaginary part before applying the inverse Fourier transform.

The source-receiver reciprocity (2.1.11) is a fundamental property of GFs when the integration domain has homogeneous boundary conditions, but it cannot be guaranteed when EGFs are retrieved from noisy SI data. This is somewhat of a problem for the common-midpoint method because it requires that the data can be logically sorted in common source, common receiver or common midpoint gathers or views. The substitution

$$G_{ij}(\mathbf{x}_A, \mathbf{x}_B) = G_{ji}(\mathbf{x}_B, \mathbf{x}_A) \to \frac{1}{2}\left(G_{ij}(\mathbf{x}_A, \mathbf{x}_B) + G_{ji}(\mathbf{x}_B, \mathbf{x}_A)\right) \qquad (4.3.1)$$

would therefore be beneficial in cases where a feature is resolved well in the G_{ij} component but not as well in the G_{ji} component. The substitution (4.3.1) is both theoretically motivated and it fundamentally guarantees the reciprocity of Green's tensor. In mathematical terms, the substitution (4.3.1) could be represented as the application of a *symmetrising operation* on G.

As seen in subsection 2.2.2, one can first retrieve Z-to-Z, N-to-E, E-to-N, N-to-N, and E-to-E components of the Green's tensor and then use the rotation formulas (2.2.6), (2.2.7), and (2.2.8) to obtain the vertical, radial, and transverse components, respectively. A key requirement to a successful rotation is that the magnitudes of the components in the Green's tensor are truthful and their mutual balance is not distorted by any interleaving processing stages. In principle, rotation should be preferentially done 'at the mine's mouth', i.e., immediately after collecting the data, if one wants to remain absolutely sure that the balance between N and E components is retained. When one postpones the rotation until the full Green's tensor has been reconstructed, there is a risk that the mutual balance is lost at one of the stacking, averaging, whole-trace balancing, or normalizing stages that make part of a typical CMP processing sequence. For lack of a better alternative, the rotation stage is in the current implementation performed after NMO correction and stacking, which must be regarded as a possible source of uncertainty. On the other hand, retrieving Green's functions in the tensor form is the most flexible way of storing the multitude of information we get from SI, which is a clear benefit of the method.

Since the vertical components and horizontal components are never correlated together, vertical component data can be NMO corrected and migrated using typical P-wave velocities ($v_{\mathrm{P}} \approx 5900\,\mathrm{m\,s}^{-1}$) and horizontal component data using typical S-wave velocities

($v_{\mathrm{S}} \approx 3400\,\mathrm{m\,s^{-1}}$). The P-wave velocity was chosen for being compatible with the petro-physical measurements and is slightly higher than the 'standard' constant velocity of $5500\,\mathrm{m\,s^{-1}}$ of the 2D active seismic lines (Heinonen et al. 2019).

4.3.2   Implementation of algorithms in C

For this thesis, I have written two algorithms in the C programming language that expand on Jan Thorbecke's `fconv` utility by adding more supported filetypes (MSEED and CSS3.0) and inserting the missing coherence computation method that includes the summation of causal and acausal parts of the trace. The first programme, `mseed_retain_sign`, is intended for reading full traces from the MSEED archive, performing spectral whitening, performing sign-bit normalization, and exporting the results in a CSS3.0 trace database. After this, one trace is chosen to be the master trace (acting as the virtual source) and the remaining ones are auxiliary traces (acting as the virtual receivers) that are correlated against it. The second programme, `fconv_css`, reads in the master and auxiliary traces, computes the coherence in a sliding window between them, and exports the coherence panels retrieved from each 24 h of noise in the `.SU` (Seismic Unix) format. The codes have ~ 500 and ~ 1100 lines, respectively, and rely on interfaces both to `libmseed` library by Chad Trabant from the IRIS Data Management Center[2] and to the Seismic Unix suite.

The programmes have switches for spectral whitening (SW) and sign-bit normalization (SBN). The basic structure of the programmes are shown in pseudocode in Algorithms 1 and 2. GNU Parallel (Tange 2011) was used to run the algorithms in parallel on four cores and eight threads on the Institute of Seismology, University of Helsinki (ISUH) office workstation (Intel Core i7-7700 @ 3.6 GHz; 256 GB RAM).

4.3.3   Proposed processing sequence

The proposed ambient noise seismic interferometry workflow for 3C data is summarized in Table 4.2. It differs somewhat from the acoustic processing sequence in Table 4.1 since it also includes the stages for data preparation from the original 24 h traces. Most notably, the geometrical spreading correction has been omitted since it was observed to shift the trace balance too much towards the bottom of the retrieved EGF panels and hindered the interpretation of the results for the next chapter.

In the reflection seismic method, field records are at different stages of the processing sorted into common-source gathers or common midpoint (CMP) gathers. Common-source gathers are useful for first-break picking and the derivation and application of static corrections for the field data. CMP gathers are useful for performing the velocity analysis and applying move-out corrections, typically followed by stacking in the CMP domain.

---

[2]`https://github.com/iris-edu/libmseed`

Algorithm 1: The `mseed_retain_sign` algorithm, used for converting the data into CSS3.0 format, performing the spectral whitening, and performing the sign-bit normalization.

Data: segments (traces) from MSEED archive

Result: CSS3.0 table containing the downsampled, spectrally whitened and sign-bit normalized samples

1 **while** *segments remain in the archive* **do**

2   read new segment;

3   lowpass filter;

4   **if** *new segment follows the previous one* **then**

5 | reallocate and zero-initialize the gap;

6   **else if** *new segment overlaps with an older one* **then**

7 | reallocate if needed and discard values from previous segment;

8   **end**

9   copy data into the sample vector and simultaneously decimate using 16-point sinc interpolation (Shannon–Whittaker);

10   **if** *spectral whitening requested* **then**

11 | **foreach** *sequence of 65536 samples* **do**

12 | | DFT the sequence;

13 | | normalize amplitude spectrum and multiply by bandpass taper function;

14 | | inverse DFT;

15 | **end**

16   **end**

17   **if** *sign bit normalization requested* **then**

18 | **foreach** *sample* **do**

19 | | sample := sgn(sample);

20 | **end**

21   **end**

22 **end**

23 write out the full data trace;

24 write out the metadata in a CSS3.0 flatfile;

Algorithm 2: The `fconv_css` algorithm, used for performing the sign-bit normalization and computing the coherence between master trace and auxiliary traces.

Data: master trace and auxiliary traces described in separate CSS3.0 flatfiles

Result: a set of SU files containing the retrieved coherencies between the master trace and auxiliary traces

1 read in master trace;

2 read in auxiliary traces;

3 **foreach** *trace in auxiliary traces* **do**

4   outdata := zeros(length of coherence vector);

5   determine overlapping part of master trace and current auxiliary trace;

6   seek to beginning of overlapping part;

7   **while** *true* **do**

8   read one windowful of data from both traces;

9   **if** *sign bit normalization requested* **then**

10   **foreach** *sample in both windows* **do**

11   sample := sgn(sample);

12   **end**

13   **end**

14   compute coherence between windows in Fourier domain ($\rightarrow$ conv);

15 $\text{outdata}_i \mathrel{+}= \text{conv}_i$;

16   slide forward by 50 % of the window length;

17   **if** *one of the data streams is exhausted* **then**

18   break;

19   **end**

20   **end**

21   prepare output trace headers;

22   export outdata trace in the SU format;

23 **end**

Table 4.2: Processing sequence for the CTBTO/OSI ambient noise data.

Stage #	Operation	Parameters
1	Spectral whitening	15–20–115–120 Hz, (on/off)
2	Sign-bit normalization	(on/off)
3	Coherence computation	60 s window, max lag 1000 ms
4	Setting up geometry in the headers	
5	Arranging into CMP gathers	
6	Application of static corrections	
7	BP filtering	30–40–110–125 Hz
8	Geometrical spreading correction	omitted (see text)
9	Trace normalization	200–400 ms
10	Wiener filtering	lag 22–38 ms, applied btw. 50–600 ms
11	BP filtering	30–40–110–125 Hz
12	Trace normalization	200–400 ms
13	Averaging along GF symmetries	
14	NMO + stacking	$v_P = 5900 \, \mathrm{m \, s^{-1}}$, $v_S = 3400 \, \mathrm{m \, s^{-1}}$
15	Rotation	ZNE $\rightarrow$ ZRT
16	BP filtering	30–40–110–125 Hz
17	Trace normalization	200–400 ms
18	Stolt migration	$v_P = 5900 \, \mathrm{m \, s^{-1}}$, $v_S = 3400 \, \mathrm{m \, s^{-1}}$
19	BP filtering	30–40–110–125 Hz
20	Trace normalization	200–400 ms
21	t–z conversion	$v_P = 5900 \, \mathrm{m \, s^{-1}}$, $v_S = 3400 \, \mathrm{m \, s^{-1}}$

Static corrections or statics are used to correct for the imprecise source ignition times and the lags caused by lower wavespeeds in the overburden. Typically field statics simultaneously shift the data to a common vertical datum, say, $Z = +100$ m. Since the empirical Green's functions have very weak first breaks in the noise-driven approach, an overburden thickness model could not be reconstructed solely from passive measurements. However, COGITO-MIN featured a simultaneous deployment of an active seismic 3D grid (Singh et al. in press) from which receiver statics could be extracted for the OSI spread. The receiver statics are listed in Appendix B for each station and were applied both at the 'virtual source' end and at the 'virtual receiver' end.

Since the subsurface velocities in Kylylahti are relatively well understood from petro-physical sampling and laboratory measurements, and the dips are steep, making velocity analysis more unstable, only a single NMO velocity of $v_P = 5900 \, \mathrm{m \, s^{-1}}$ (and for S-waves, $v_S = 3400 \, \mathrm{m \, s^{-1}}$) was used. However, SNRs are moderately good in CMP gathers, and velocity analysis remains a viable option for SI in areas with unknown *in situ* seismic

velocities.

Chapter 5

Results and discussion

Le bruit est parasite, il suit la logique du parasite, chose très petite, raison sans suffisance, cause souvent sans conséquence, qui peut s'évanouir à gauche de la queue d'aronde, qui peut croître et grandir, à droite de l'instauration.

— Serres, Michel (1982). *Genèse*, p. 56.

5.1 Retrieval of 1C Green's functions

The effect of spectral whitening and sign-bit normalization on empirical Green's function (EGF) retrieval was studied using 1C data (vertical components) only because they are the easiest to compare against results from synthetic modelling. When the proper parameter combination had been determined, the approach could be extended to 3C data for the retrieval of vertical–radial–transverse (ZRT) components.

5.1.1 Effect of spectral whitening and sign-bit normalization

At an early stage, it became clear that whole-trace spectral whitening (SW) had a minimal effect on the retrieved EGFs. A visual inspection could not tell any significant difference between correlation panels retrieved with SW applied or not. This could be explained by the fact that the normalized coherency operator (see subsection 4.3.1) already takes care of prewhitening and thus makes an extra whitening stage redundant. Therefore, the EGFs shown in this chapter have been computed without whole-trace spectral whitening.

Figure 5.1 shows the effect of sign-bit normalization (SBN) on a common-source gather whose virtual source has been reconstructed at receiver 525, about in the middle of the Northern line. The traces in the common source gather have been muted above and at the expected first break picks using an apparent velocity of $6000\,\mathrm{m\,s^{-1}}$. The left figure shows the EGFs retrieved without SBN. The EGFs in the right figure have been computed using sign-bit normalized traces. The reflectivity is slightly stronger and individual reflectors

47

appear brighter, narrower, and laterally more continuous in the sign-bit normalized traces but the SNR is not significantly better than in the panel formed with unclipped traces. Some improvement can be seen in the area delimited by the black rectangle, which is the place where mineralization-associated reflections would be expected.

An example CMP gather for CMP 42 is seen in Fig. 5.2. Again, the left figure shows the EGFs retrieved without SBN and the right figure with SBN. The black lines are the theoretical reflection parabolae associated with horizontal reflectors at different depths. In a geometry with horizontal, flat reflectors, the CMP gather is symmetric about the midpoint and every reflector corresponds to a parabola defined by the NMO equation

$$t^2(x) = t_0^2 + \frac{x^2}{v_{\mathrm{NMO}}^2} \ , \tag{5.1.1}$$

where t is two-way traveltime, t_0 is the two-way traveltime at zero offset (that can be converted to depth using a suitable velocity model), x is the horizontal offset, and v_{NMO} is a representative velocity for the NMO correction (here $5900\,\mathrm{m\,s^{-1}}$). When the medium has a uniform wave speed, it can be taken as a suitable value for v_{NMO}.

In Figure 5.2, the effect of applying SBN is more apparent to the eye. The SBN version has more clearly defined reflective events and an overall increased reflectivity between normal-incidence two-way traveltimes between $100\,\mathrm{ms}$ and $300\,\mathrm{ms}$. In particular, the parabolae between $400\,\mathrm{ms}$ and $600\,\mathrm{ms}$ are more evident in the SBN figure. However, some of the detail in the left figure is also lost, like in the reflectors above the $\sim 400\,\mathrm{ms}$ mark.
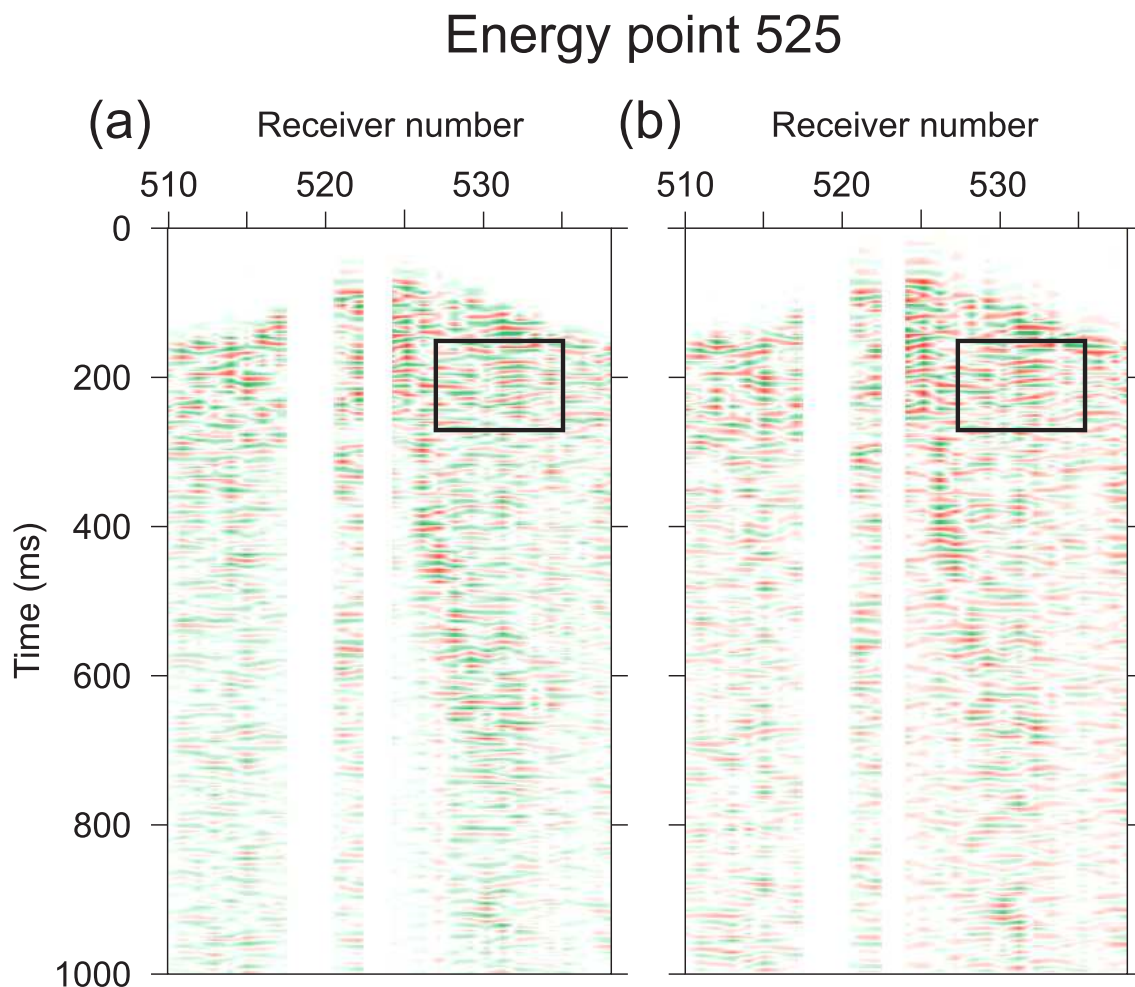
Figure 5.1: Empirical Green's functions extracted from 36 days of noise on Line 05 and sorted into a virtual shot gather, with virtual source located at geophone 525. The black square indicates the region where mineralization-associated reflections are expected according to synthetic modelling. (a) Without sign-bit normalization (SBN). Although the signal-to-noise ratio is elevated within the black rectangle, the individual reflectors are narrow and blend into each other. (b) With SBN. The area within the rectangle is more detailed than in the left figure, although the signal still does not stand out very clearly from the noise.
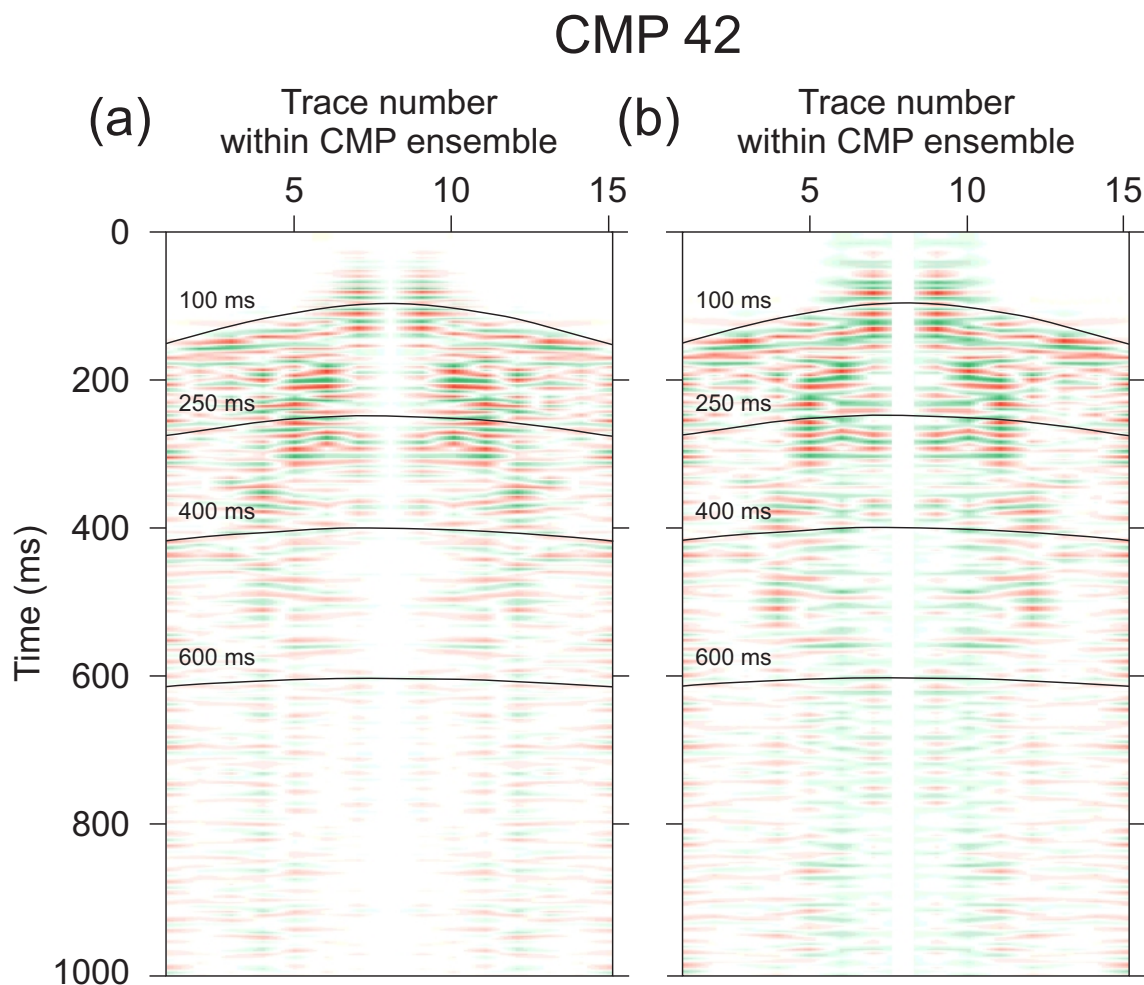
Figure 5.2: Empirical Green's functions extracted from 36 days of noise on Line 05 sorted into a virtual CMP gather about the midpoint 42. The black curves are the two-way traveltime predictions associated with horizontal reflectors at different depths (around $300\,\mathrm{m}$, $750\,\mathrm{m}$, $1200\,\mathrm{m}$, and $1800\,\mathrm{m}$) for a constant-velocity $v_{\mathrm{NMO}} = 5900\,\mathrm{m\,s^{-1}}$. After NMO correction and stacking, all details observed at less than $100\,\mathrm{ms}$ are based on relatively few traces and should not be used in final interpretation. (a) Unclipped traces, no sign-bit normalization (SBN). Elevated reflectivity can be observed at short offsets between $150\,\mathrm{ms}$ and $300\,\mathrm{ms}$. (b) With SBN. The short-offset data appears to be more detailed than in the left figure. The reflector with traveltime at normal incidence $t_0 = 550\,\mathrm{ms}$ is narrower but laterally more continuous.

5.1.2 Effect of recording time

As mentioned in chapter 4, the SI approach benefits most from body-wave contributions from the stationary-phase areas (Snieder and Sens-Schönfelder 2015). If the source distribution is unknown and there is no prior control of them, an immediate way to maximize the chances to retrieve body-waves is to aim at long recording times. However, increasing the recording time without bounds is not generally feasible since the random process behind the geophone data is not fully ergodic and the convergence cannot be guaranteed unless significant stationary-phase contributions are made to the representation integral. Indeed, there seems to be a trade-off between the duration of the recordings and the quality of the retrieved EGFs. The shape of this trade-off curve must so far be considered unknown due to the lack of previous studies in crystalline bedrock.

In statistics, *bootstrapping* is a technique for estimating the parameters of a distribution by forming (possibly overlapping) subsets of the original data samples and recomputing the statistics for the new 'sample pools'. A variant of this method can be used for the SI data to investigate the stability of the retrieved EGFs with increasing recording times. For comparisons, three subsets were formed by random sampling from 36 recording days, comprising 5, 10, and 20 days of data, respectively. The days of year that form the subsets are listed in Table 5.1.

Table 5.1: List of the days used for bootstrap testing on the whole data set (marked as the null hypothesis H_0 on the bottom line).

Sample #	Days in sample	Days of year forming the sample
1	5	224–225, 243, 245, 254
2	10	230–232, 234, 238, 240, 242–244, 256
3	20	224, 226–227, 230–231, 233, 235–237, 239–244, 247, 251–252, 254, 258
4 (H_0)	36	224–259

The stacked and migrated cross-sections of the bootstrapped CMP data are shown in Figures 5.3a–c (no sign-bit normalization) and 5.4a–c (sign-bit normalized). The main difference between panels based on five (a) and ten (b) days of data is the more uniform reflectivity near 100 ms at CMP 10 and the reorganization of the likely ore-associated reflectors (black rectangle in Figures 5.3a–c and 5.4a–c) between CMPs 40–50 into two oppositely tilted planes in Figs. 5.3b and 5.4b. The SNR is also greatly reduced at two-way travel times above 300 ms. The panels based on ten (b) and twenty (c) days of data do not show significantly better retrieval of the assumed ore-associated reflectors. However, the reflectivity at CMP 40 between 200 ms and 300 ms of two-way traveltime stands out more clearly in Fig. 5.4c than in other figures. The area between CMPs 20–40 is retrieved very

differently in all three panels and no single reflector can unambiguously be associated with the bottom of the OUM unit at CMP 30 (cf. Fig. 3.3). In the panels formed using 20 days of data, the sign-bit normalized version (Fig. 5.4c) appears visually to have a slightly lower signal-to-noise ratio than the unclipped version (Fig. 5.3c). The situation is the same for the panels based on 10 and 5 days of data (Figs. 5.4a–b and 5.3a–b). On the other hand, the sign-bit normalized versions have more detail in their reflection responses which might also be a good thing in terms of pointing out potential exploration targets.

5.1.3 Effect of static corrections

As discussed earlier in subsection 4.3.3, the simultaneous deployment of an active seismic 3D grid allowed the determination of static corrections at each receiver's location (Singh et al. in press). Appendix B lists the field statics in milliseconds that were applied to each virtual source and virtual receiver in the CTBTO/OSI spread. Even though residual statics would have been available as well, only the field static component was used since the residual component was thought to pertain to the active seismic 3D experiment and therefore be less general and less applicable to the OSI acquisition.

Figures 5.5a–d show the effect of field statics on common-source gathers on lines 05 and 08. The EGFs have been retrieved with sign-bit normalization. Apart from the general static shift of around 10 ms, the differences between the left and right panels are overall small, due to the little variance in the individual values of the shift. On Line 05 (Northern line), the mean one-way correction applied was 11 ms with a standard deviation of 3 ms. On Line 08 (Southern line), the mean one-way correction applied was 12 ms with a standard deviation of 5 ms.

The effect of field statics may be more clearly seen in Figures 5.6a–d which represent the top 400 ms of the NMO corrected and CMP stacked data without migration. According to the synthetic modelling of subsection 4.1.3, the reflective packages that arise from point features (features whose dimensions are small with respect to the dominant wavelength) ought to correspond to diffraction parabolae on the non-migrated sections. The reflective features on the Northern line (Line 05) are more nicely organized into arcs when field statics are applied to the data before stacking. On the Southern line (Line 08), the effect is twofold. Most notably, the features that look like sustained subhorizontal reflectivity at CMP 20 at 300 ms (indicated by the black arrow) disappear after applying the field statics. The area near CMP 20 has a reduced station coverage due to Kylylampi Pond (c.f. Fig. 1.1) and short offsets in the CMP gathers are effectively missing, which means that 'ghosts' related to large offsets can appear in the sections. The area inside the black rectangle is modified somewhat by the static corrections, simplifying the reflectivity in the shallow part, whereas the left side (WNW) of the section seems unaltered by them.

5.1.4   Preferred workflow for the Z-to-Z

For a conclusion, the lessons learned from 1C Green's function processing are briefly summarized, to pave the way for the 3C results which will be discussed in the next section.

Sign-bit normalization appears to enhance the deep reflectivity and make individual reflections brighter, laterally more continuous, and more localized in the depth dimension – all desirable qualities in reflection seismics. However, the signal-to-noise ratio is not always improved by SBN if the recording times are long and SI has had time to converge. It is therefore important to consider the effect of SBN on the retrieved EGFs on a case-to-case basis.

Static corrections, when available, have a positive impact on the retrieved EGFs because they eliminate some of the uncertainty in static shifts related to overburden thickness variations. When topography is moderate, bedrock is unfractured, and the bedrock-overburden contact is close to horizontal, the sample variance of field statics can be low, and the correction may not contribute a seemingly great difference to the retrieved EGFs. In this case, however, the static corrections were seen to improve the quality of the vertical-component data and were applied to all vertical-component panels that follow. The unknown residual corrections can constitute a possible source of error in some areas.

After time-to-depth conversion using a constant velocity of $5900\,\mathrm{m\,s^{-1}}$, the vertical component results are shown side by side with the geological model in Figs. 5.7 (Line 05) and 5.8 (Line 08). Both figures are dominated by relatively low frequencies, but higher-than-average reflectivity consistently follows the areas with the largest contrasts in seismic impedance. It is important to understand that the geological models of Figures 3.3 and 3.4 are largely simplified in the sense that, as mentioned earlier in subsection 3.4.1, soapstone alterations can cause internal reflectivity within the ultramafic units.

On the WNW side of Figure 5.7, there is significant elevated reflectivity between the model depths of $100\,\mathrm{m}$ to $400\,\mathrm{m}$ which, however, does not align laterally with the shallow ultramafic body underneath receiver 517. It should be noted that the 3D geometry of the deposit can easily fool the Stolt migration algorithm when it is used in two dimensions, which can lead to misalignments in the depth sections.
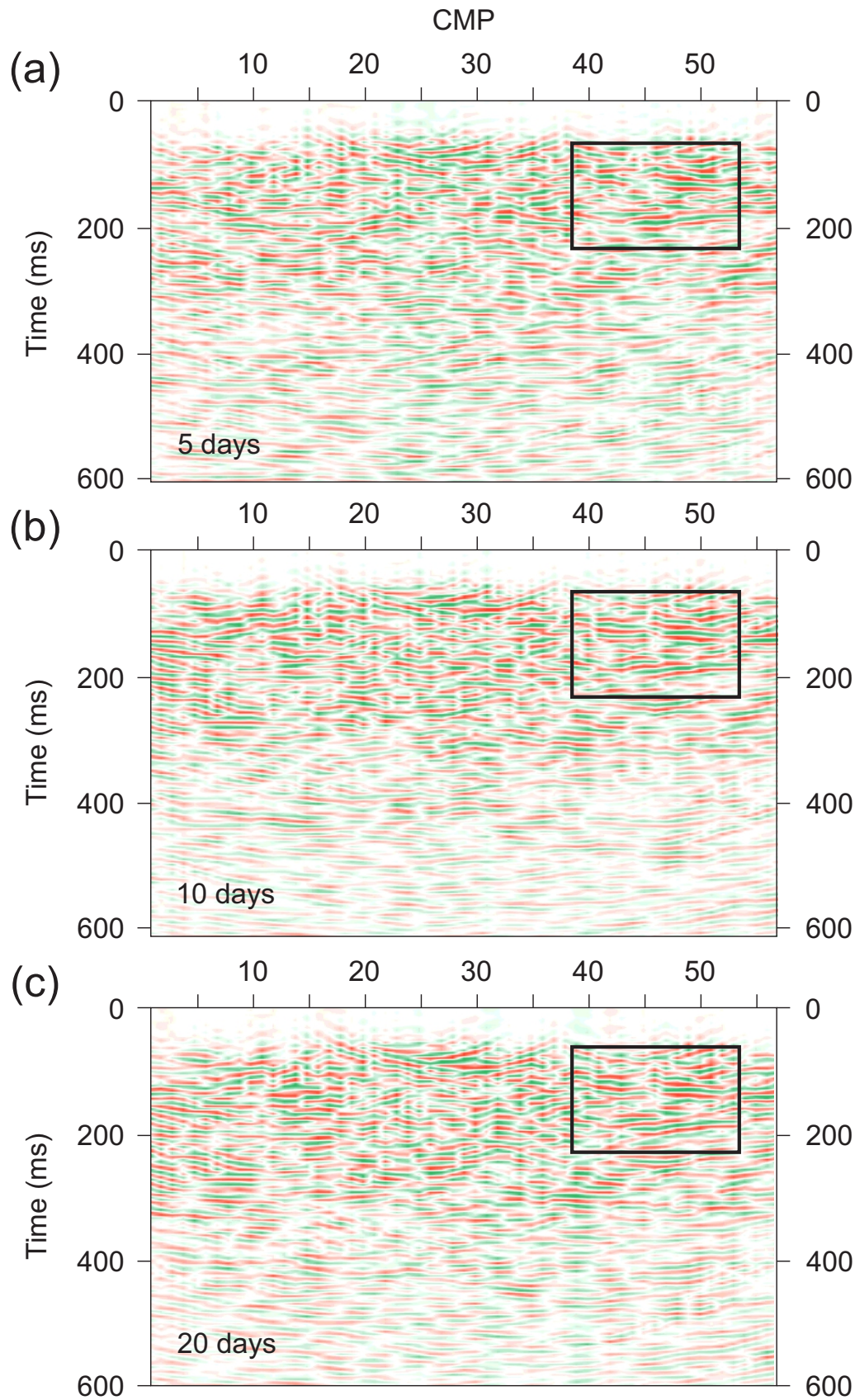
Figure 5.3: CMP stacked, NMO corrected and migrated cross sections for Line 05. The empirical Green's functions are computed without sign-bit normalization. The three panels are based on varying numbers of correlation days to model the effect of recording time on the quality of the retrieved EGFs. (a) 5 days of data, (b) 10 days of data, (c) 20 days of data.
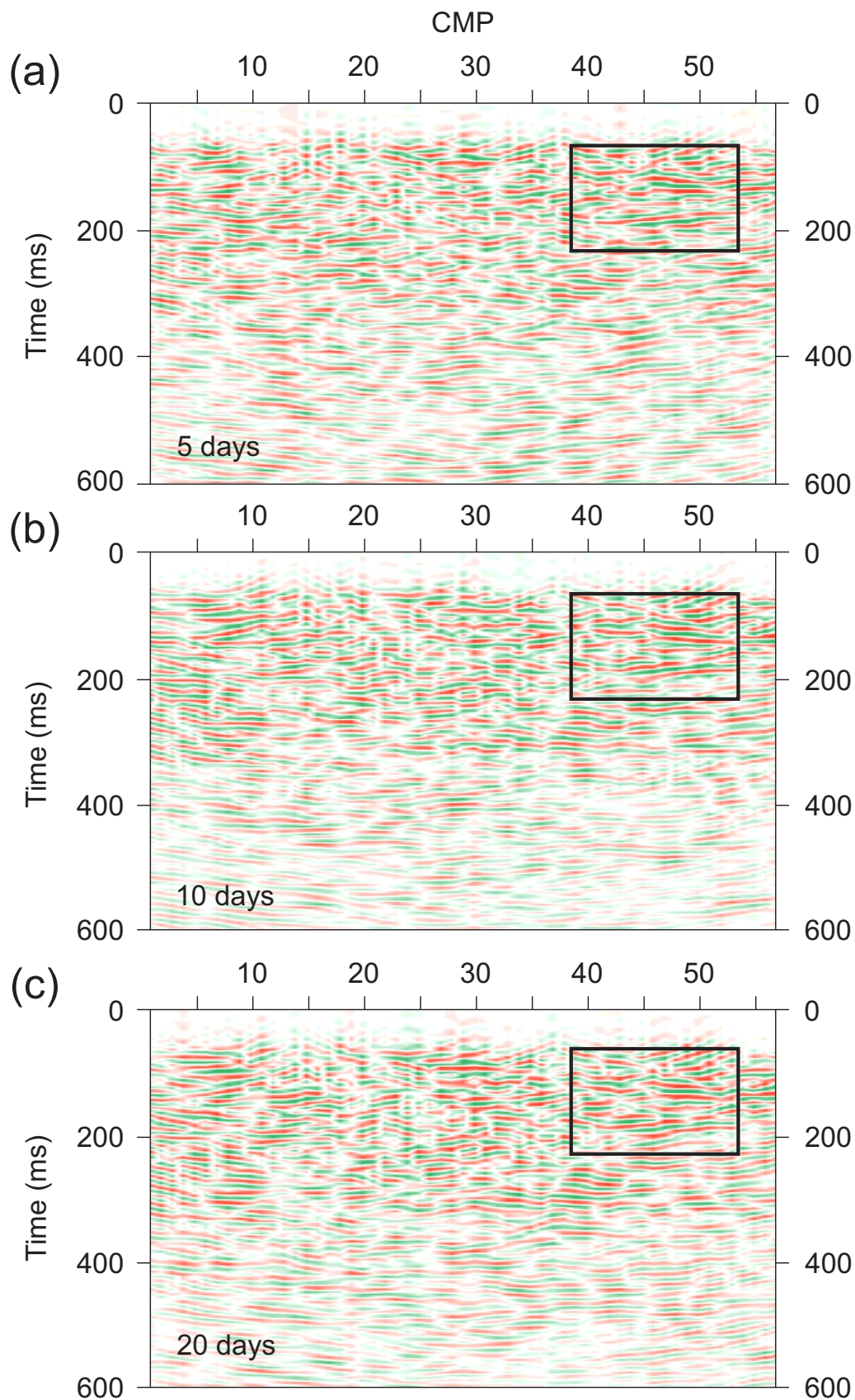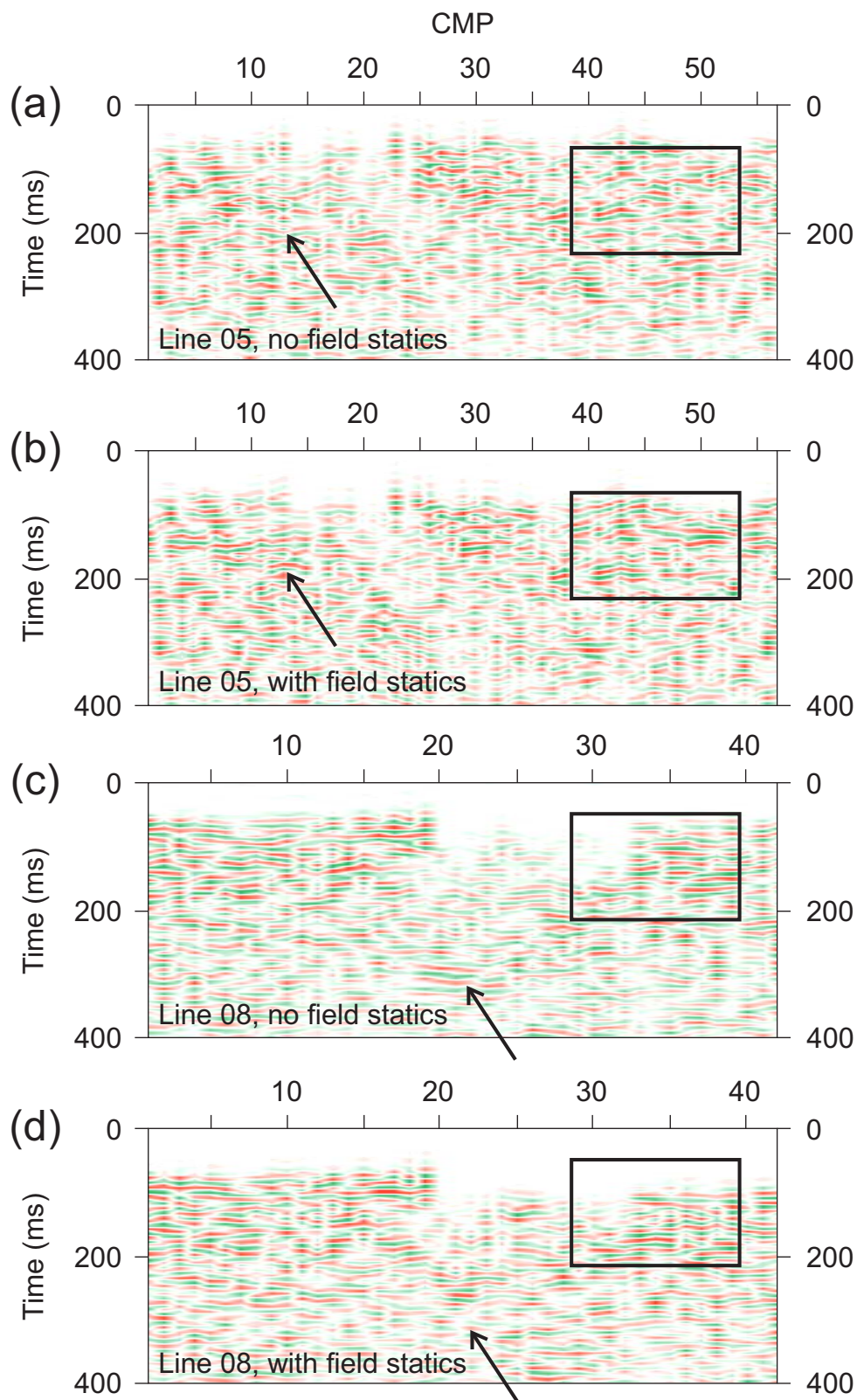
Figure 5.4: CMP stacked, NMO corrected and migrated cross sections for Line 05. The empirical Green's functions have been computed using sign-bit normalization. The three panels are based on varying numbers of correlation days to model the effect of recording time on the quality of the retrieved EGFs. (a) 5 days of data, (b) 10 days of data, (c) 20 days of data.
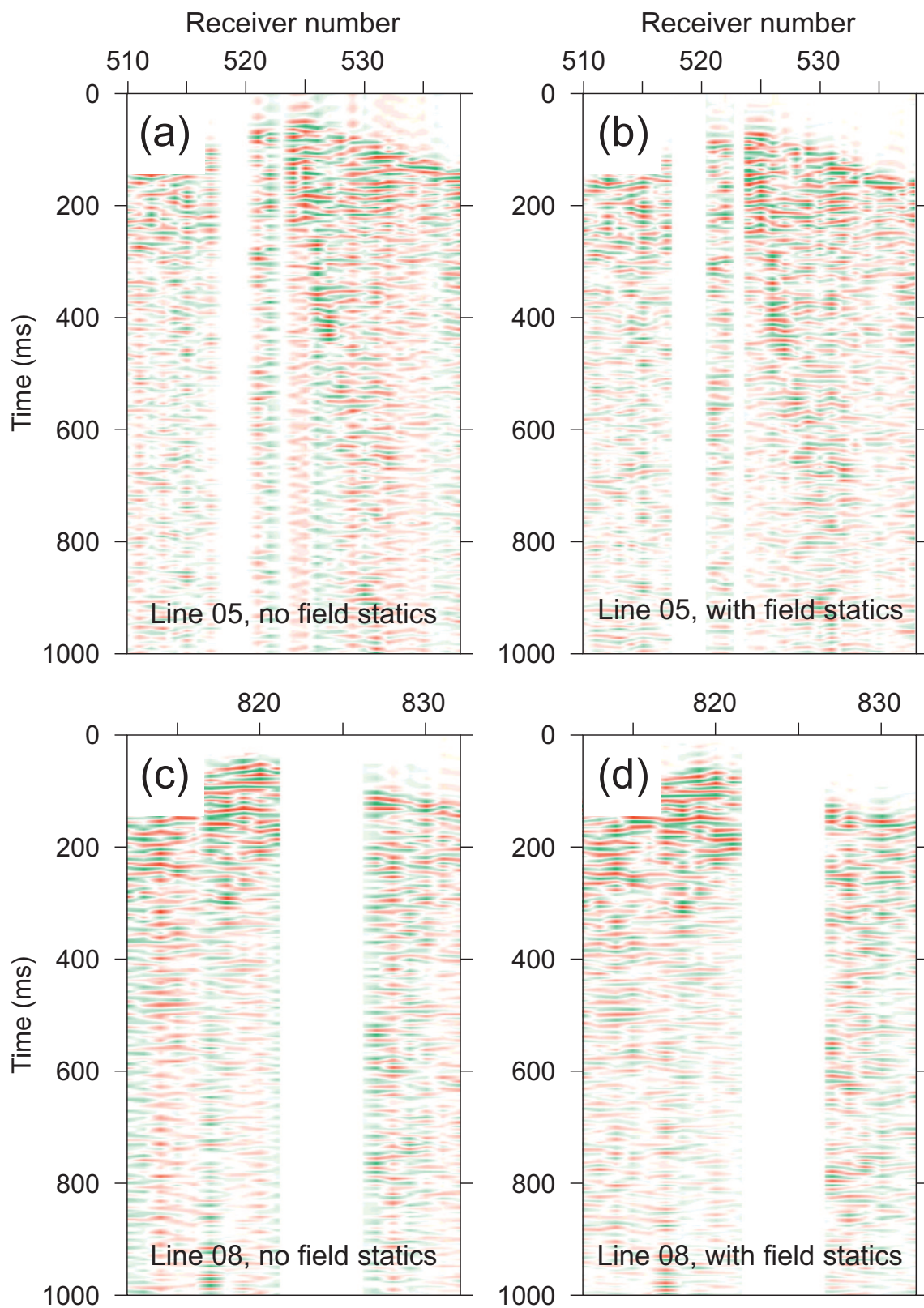
Figure 5.5: Comparison of the effect of field statics on the empirical Green's functions, computed with sign-bit normalization. The panels represent virtual shot gathers, with virtual source located at geophone 525 (for Line 05) or 820 (for Line 08). (a) Line 05, no field statics, (b) Line 05, field statics applied, (c) Line 08, no field statics, (d) Line 08, field statics applied.

Figure 5.6: Comparison of the effect of field statics on the NMO corrected and CMP stacked sections. The empirical Green's functions have been computed using sign-bit normalization. (a) Line 05, no field statics, (b) Line 05, field statics applied, (c) Line 08, no field statics, (d) Line 08, field statics applied.
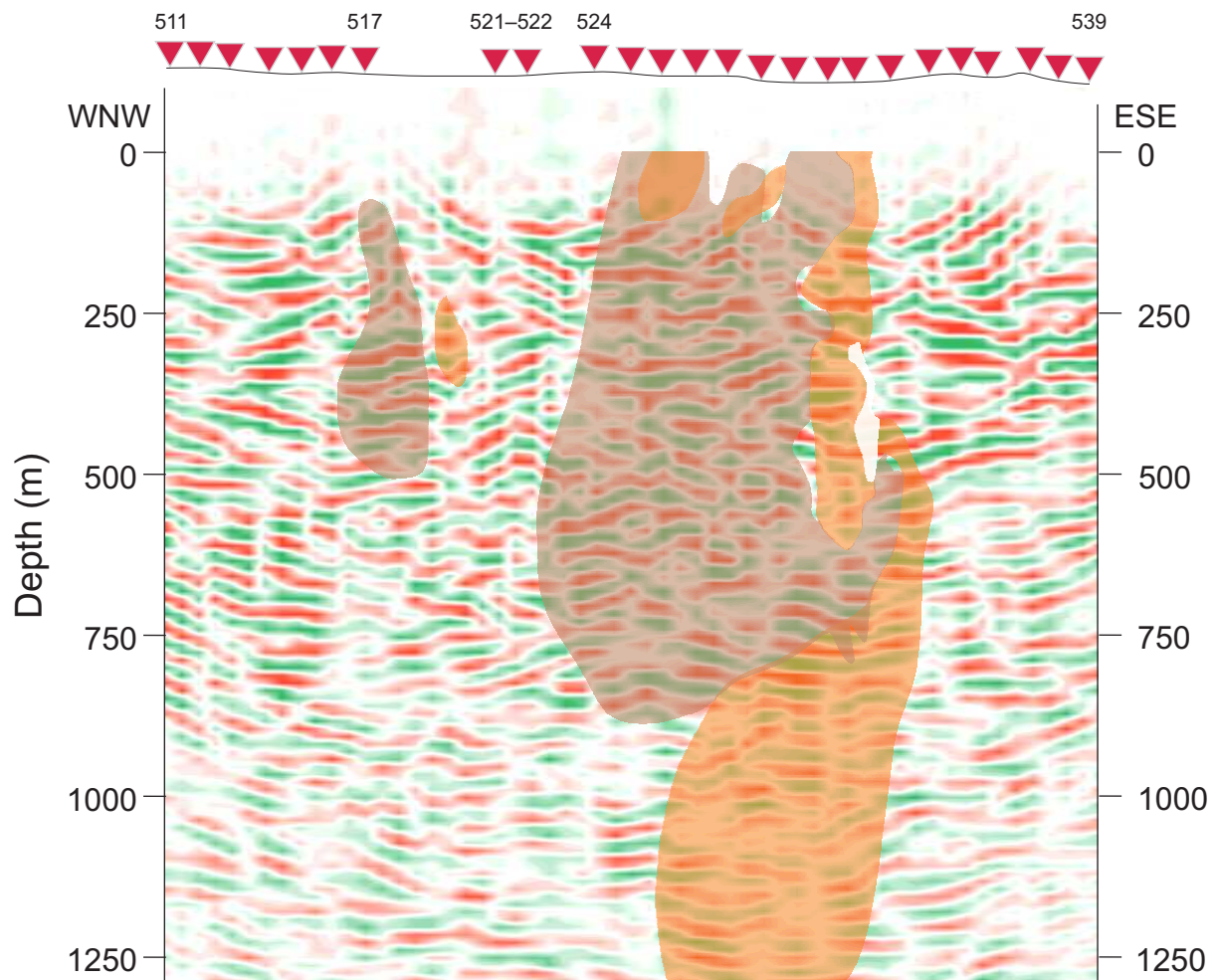
Figure 5.7: Migrated and depth-converted seismic reflectivity section extracted from vertical-component data on Line 05 (Northern line), shown side by side with a slice from Boliden's geological model. The explanations of the lithological units are shown earlier in Figure 3.3.
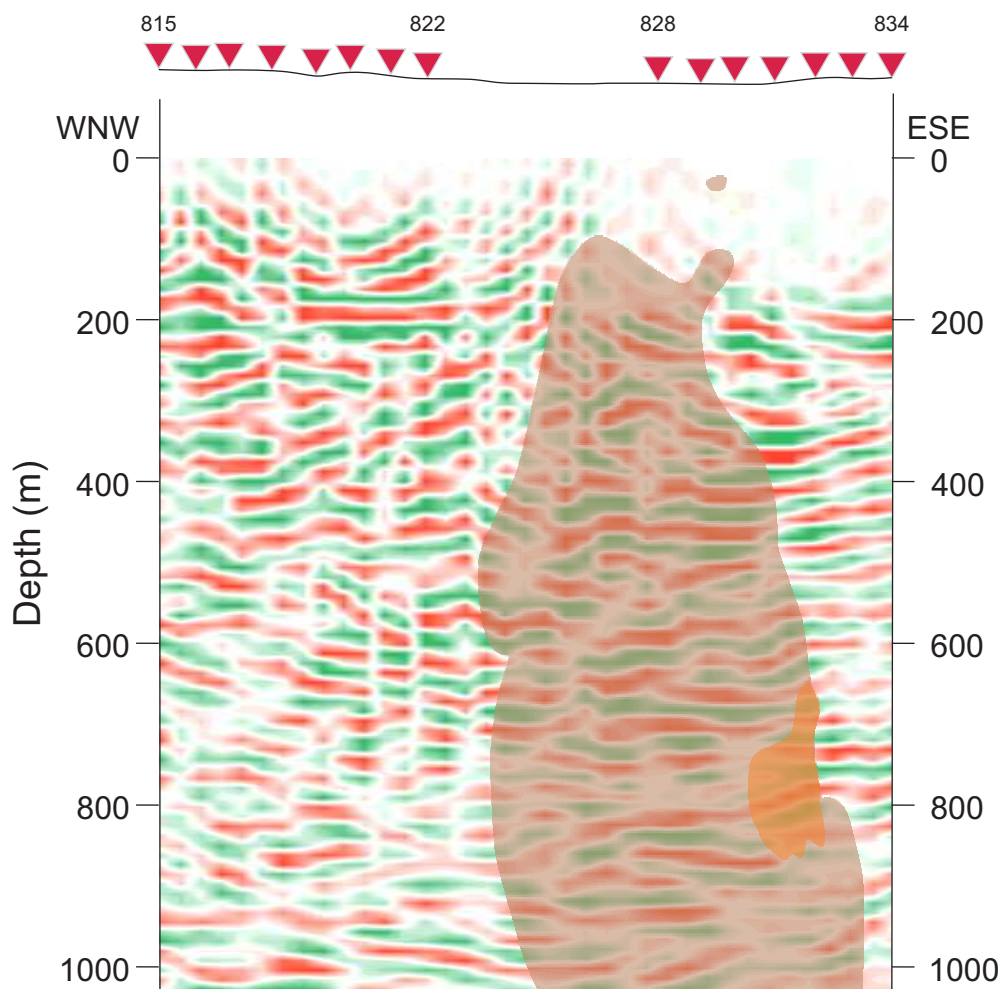
Figure 5.8: Migrated and depth-converted seismic reflectivity section extracted from vertical-component data on Line 08 (Southern line), shown side by side with a slice from Boliden's geological model. The explanations of the lithological units are shown earlier in Figure 3.4.

5.2   Retrieval of 3C Green's functions

The 3C processing sequence was only slightly modified from the 1C sequence listed in Table 4.2. Since the static corrections (for overburden thickness variation) had originally been computed for P-waves, they could not be directly applied for S-wave extraction. That is why static corrections were omitted for the horizontal-component data. However, some S-to-P conversion is sure to take place at the bedrock-overburden contact (30 m to 90 m in depth), which would give a partial justification to use the same field statics here as for the vertical-component data.

Another modification to the processing sequence for the horizontal components was to change the NMO, migration, and time-to-depth conversion velocities to a representative S wave velocity. There were no in situ or laboratory measurements of S wave velocities in the rocks, but provided the bedrock is a Poisson solid (for which the two Lamé parameters λ and μ are equal), the v_P/v_S ratio is theoretically expected to be $\sqrt{3}$. Therefore, assuming a P-wave velocity of $v_P = 5900\,\mathrm{m\,s^{-1}}$ gives a reasonable estimate $v_S \approx 3400\,\mathrm{m\,s^{-1}}$.

5.2.1   Characteristics of the Green's tensor in the horizontal

As the result of cross-correlating the horizontal component data with itself, the four missing components of the Green's tensor (N-to-N, E-to-E, N-to-E, E-to-N) were retrieved. Figure 5.9 is a comparison plot of the four Green's tensor components. Just like Figure 5.1, it represents a common-source gather whose virtual source has been reconstructed at receiver 525 or about in the middle of the Northern line. The traces in all four panels have been muted above and at the expected first break picks using an apparent velocity of $3400\,\mathrm{m\,s^{-1}}$. All EGFs have been computed using sign-bit normalized traces.

The black rectangles in Fig. 5.9 are the areas where ore-associated reflections should be expected to be found. No single panel shows arrivals that can clearly be associated with ore-associated reflectors, but the N-to-E and E-to-E panels (Fig. 5.9b and a) have elevated signal levels with respect to the N-to-N and E-to-N panels (Fig. 5.9d and c). Instead, the short offsets at two-way traveltimes less than 300 ms are filled with coherent energy whose internal details appear clearer here than in the vertical-component panel (Fig. 5.1). All four panels also demonstrate considerable ringing at the ~ 25 ms period.

An example CMP gather for CMP 42 is seen in Fig. 5.10. Again, the four panels correspond to the four horizontal components of the Green's tensor. The black lines are the theoretical reflection parabolae (c.f. Equation 5.1.1) associated with horizontal reflectors at different depths. The ore-associated reflections, if there are any, are expected to be encountered between 100 ms and 400 ms of two-way traveltime. All four panels have enhanced reflectivity at two-way traveltimes less than 300 ms. In particular, enhanced reflectivity can be seen in the E-to-E component of the Green's tensor (Figure 5.10a) and to a smaller extent, in the
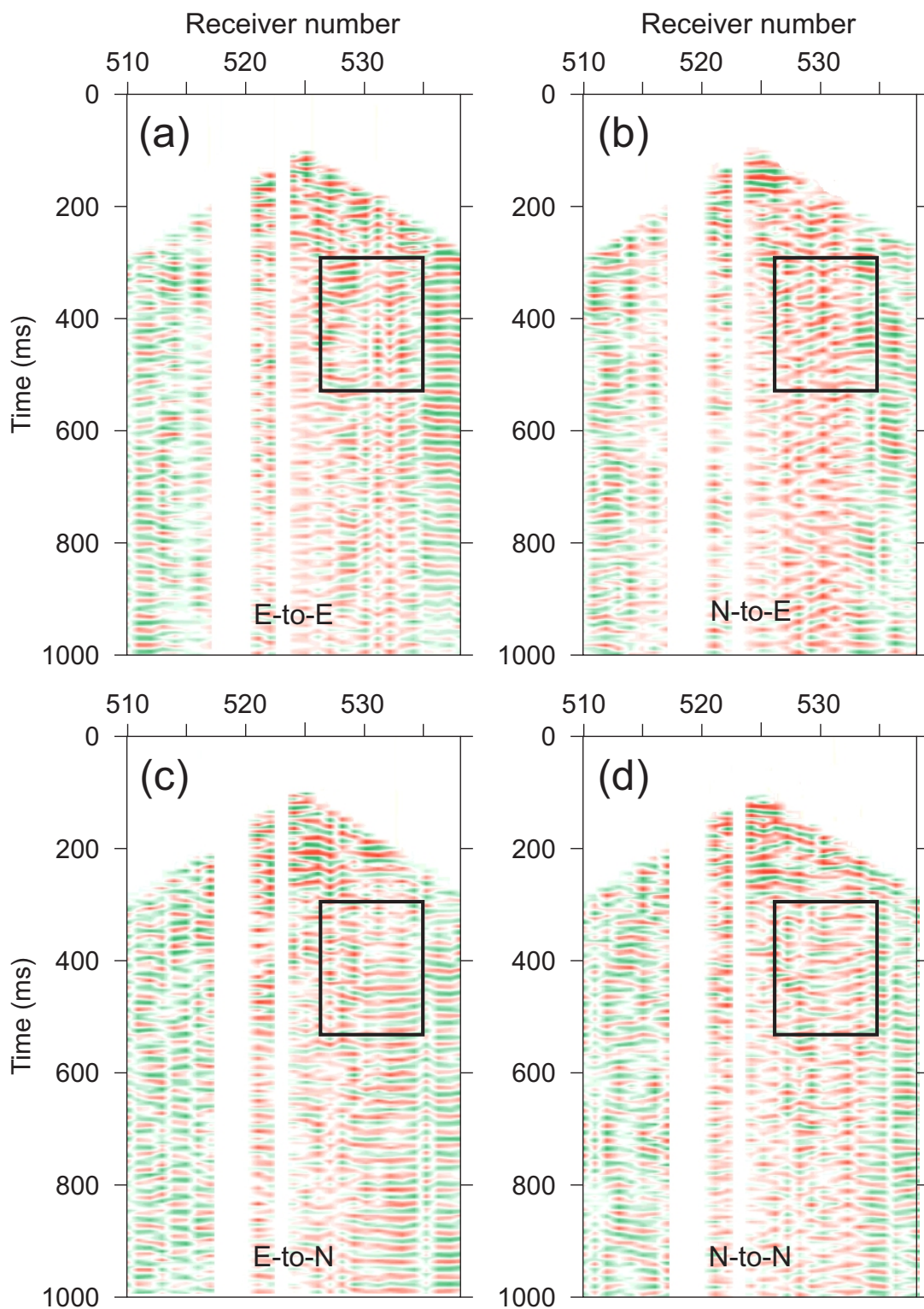
Figure 5.9: EGFs extracted from 36 days of sign-bit normalized noise on Line 05 sorted into virtual shot gathers, with virtual source located at geophone 525. The black square indicates the region where mineralization-associated reflections are expected according to synthetic modelling. The four panels stand for various source and receiver orientations: (a) source facing E, receiver facing E; (b) source facing N, receiver facing E; (c) source facing E, receiver facing N; (d) source facing N, receiver facing N.

N-to-N component (Figure 5.10d). The asymmetric nature of the off-diagonal CMP gathers immediately strikes the eye. For example, in Figure 5.10b there is elevated reflectivity at 250 ms of two-way traveltime on the left side of the CMP gather which is not repeated on the right side of the same figure. Instead, Figure 5.10c seems to be a vertically flipped version of section Figure 5.10b in the sense that there the feature is visible on the right side but not on the left.
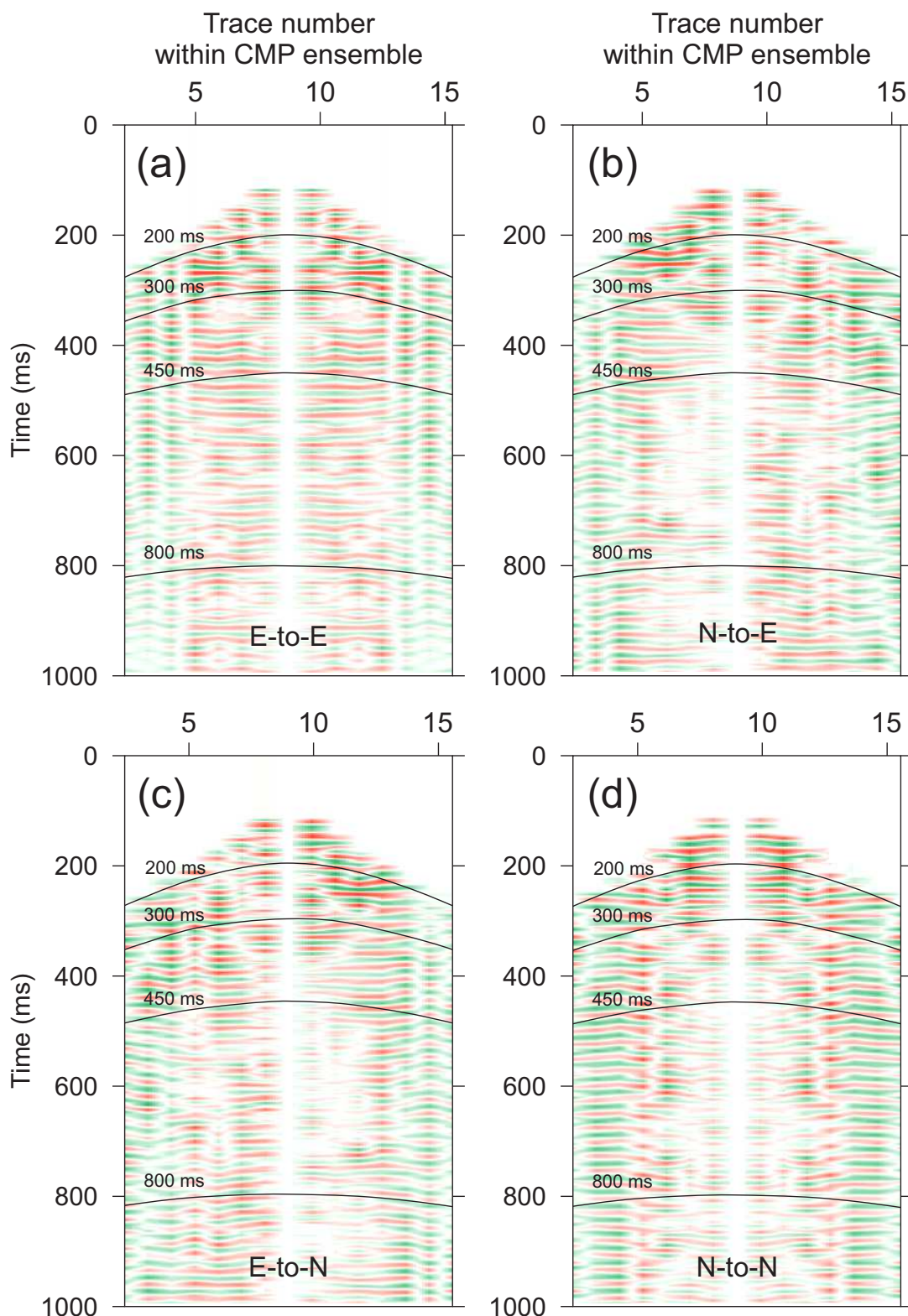
Figure 5.10: EGFs extracted from 36 days of sign-bit normalized horizontal-component noise on Line 05 sorted into virtual CMP gathers about the midpoint 42. The four panels stand for various source and receiver orientations: (a) source facing E, receiver facing E; (b) source facing N, receiver facing E; (c) source facing E, receiver facing N; (d) source facing N, receiver facing N. The black curves are the two-way traveltime predictions for S waves associated with horizontal reflectors at different depths (around 340 m, 510 m, 770 m, and 1400 m) using a constant velocity of $v_{\text{NMO}} = 3400\,\text{m s}^{-1}$.

5.2.2 Vertical, radial, transverse

To visualize the effect of sign-bit normalization on three-component EGF retrieval, Figures 5.11–5.14 show the NMO corrected, CMP stacked and migrated cross sections for Line 05 and Line 08 with SBN turned either off (Figs. 5.11 and 5.13) or on (Figs. 5.12 and 5.14). Each figure has three subplots or panels corresponding to the three principal orientations of the ZRT coordinate system, that is, vertical, radial (parallel to the strike of the line), and transverse (perpendicular to the strike of the line). All figures are based on full 36 days of recorded seismic noise. Field statics have only been applied to the vertical components.

Since S-wave energy is thought to be manifested in the radial and transverse components of the profile (Figs. 5.11–5.14bc), the black rectangles showing the area of interest in each figure have been lagged and extended along the time axis in the lower two panels to compensate for the slower wavespeed of S-waves with respect to P-waves. This also means that the information content of the lower two panels is spread out much more along the time dimension than in the top panel, a fact that must be considered before making visual comparisons between them.

Line 05 (Northern line)

The features seen in the vertical-component panels (Figs. 5.11a and 5.12a) have already been discussed above, in subsection 5.1.2.

The area indicated by the black rectangles in the radial-component panels (Figs. 5.11b and 5.12b) exhibits layered subhorizontal reflectors at ca. 300 ms. They are best visible in the unclipped panel (no SBN). From 400 ms of two-way traveltime onward there is pervasive enhanced reflectivity that breaks down in the sign-bit normalized version. On the other hand, the reflectivity at 300 ms to 400 ms near the left (WNW) end of the radial-component cross-sections emerges more clearly in the sign-bit normalized version than in the unclipped one. As was noted already in subsection 5.1.2, when SBN is applied, the maxima and minima of the data are more profound and the frequency content appears to be shifted to the low-frequency end with respect to the unclipped cross-sections.

In both transverse-component panels (Figs. 5.11c and 5.12c), reflectivity within the black rectangle is weak and sporadic. There is, however, some internally layered reflectivity between CMPs 20–30 at < 200 ms of two-way traveltime that emerges more clearly in the version where SBN has been turned off. However, the sign-bit normalized version is useful because comparisons between correlation results retrieved using two different methods help figure out where the signal is and where the noise is. It is also helpful to the interpreter that the deep reflectivity (> 300 ms) is more enhanced in the sign-bit normalized version, partly compensating for the lacking geometrical spreading correction because an optimal value for the time exponent could not be found.
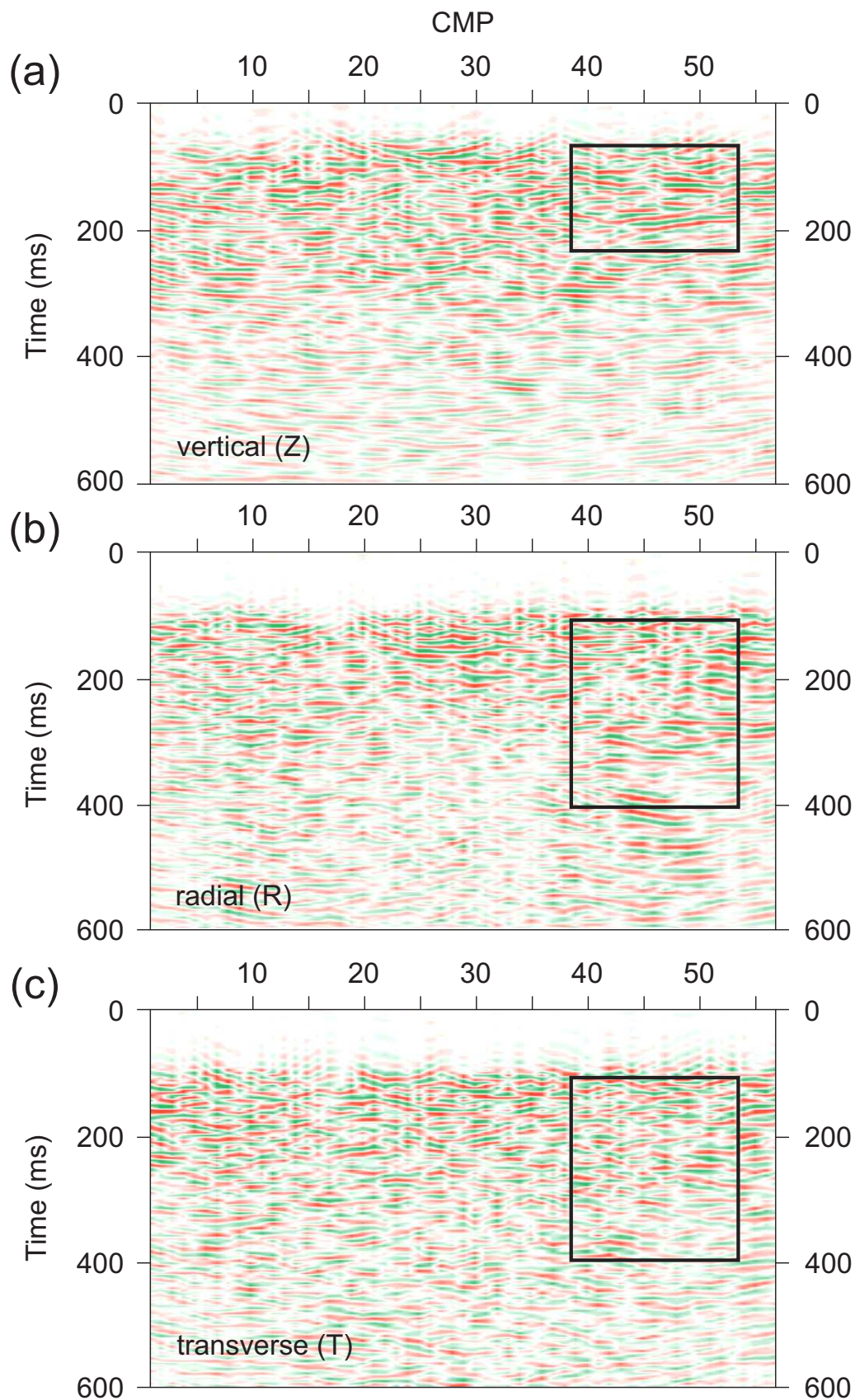
Figure 5.11: CMP stacked, NMO corrected and migrated cross sections for Line 05. The empirical Green's functions are retrieved for (a) vertical, (b) radial, and (c) transverse components, respectively, after the rotation of Green's tensor. Sign-bit normalization was not applied to the traces before coherency computation.
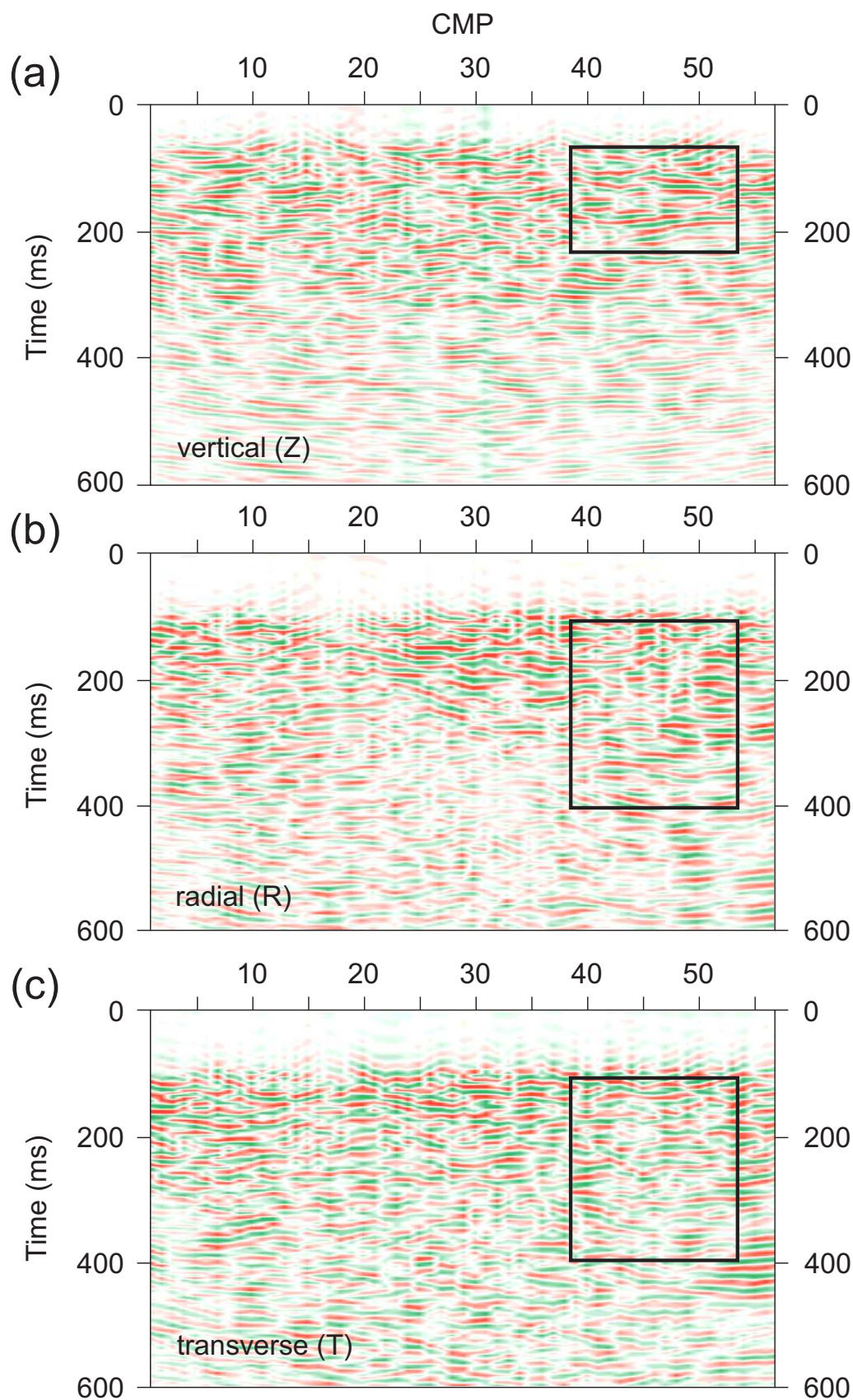
Figure 5.12: CMP stacked, NMO corrected and migrated cross sections for Line 05. The empirical Green's functions are retrieved for (a) vertical, (b) radial, and (c) transverse components, respectively, after the rotation of Green's tensor. Sign-bit normalization was applied to the traces before coherency computation.

Line 08 (Southern line)

On the Southern line, there is less knowledge of the geological structures than on the Northern line due to the small number of intersecting drill holes, and it is hard to make definitive parallels between lithology and the patterns observed in the reflectivity sections. One of the features that Boliden's lithological model predicts in the stacked and migrated NMO section is a bright reflective package between CMPs 15 and 20 near 200 ms of two-way traveltime and to its right, a set of subhorizontal reflectors extending to the right end of the section (c.f. Fig. 4.5). The area where the bright package would be expected has been marked with a black rectangle in Figures 5.13a–c and 5.14a–c.

In the vertical-component panels (Figs. 5.13a and 5.14a), the area delineated by the black rectangle has a stronger SNR in the sign-bit normalized version (Fig. 5.14) with respect to the unclipped one, but it is still difficult to discern any internal structure within the anomaly. Another remarkable feature of the vertical-component sections is that the shallow parts of the sections between CMPs 0 to 25 are saturated with coherent seismic energy that occasionally appears to extend to the right (ESE) end of the profile.

In the radial-component panels (Figs. 5.13b and 5.14b), more structure can be discerned within the black rectangle than in the vertical, but the section exhibits considerable ringing that disturbs the interpretations. Some of the more interesting features are the reflection piles on both sides of the black rectangle, one of which has been marked with a black arrow and is traceable over all three component orientations. The panel with SBN applied also shows strong uniform reflectivity towards the left (WNW) end of the section, from which the aligned reflectors curve upwards towards the middle part of the section.

In the transverse-component panels (Figs. 5.13c and 5.14c), there is indiscernible reflectivity within the black rectangle. However, the stacked reflectors on both sides of the rectangle are again very well visible and they come out stronger in the sign-bit normalized panel. Notably, there is some very bright reflectivity at ca. 200 ms near CMP 13 which, however, is not present in the vertical or the radial panels.
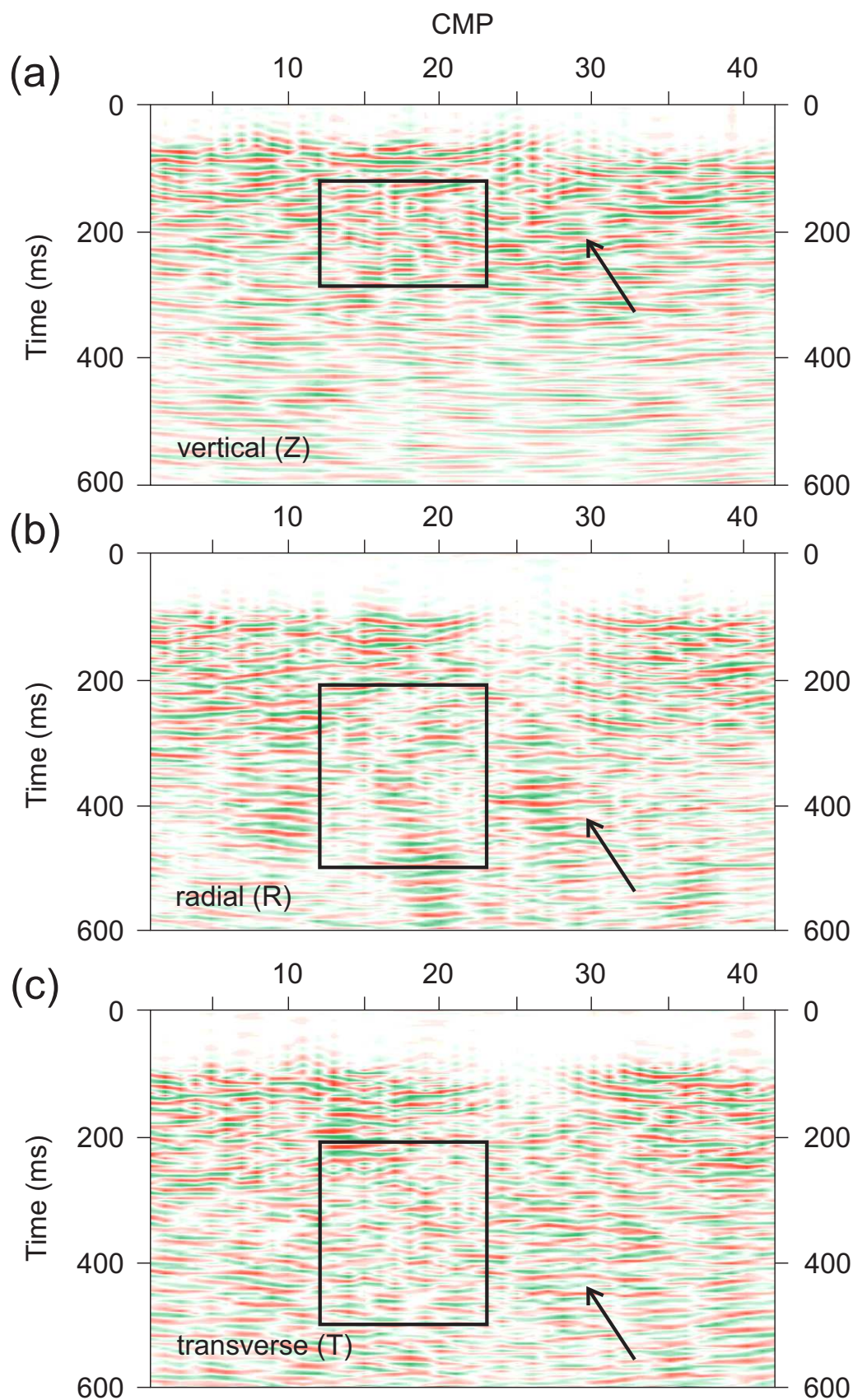
Figure 5.13: CMP stacked, NMO corrected and migrated cross sections for Line 08. The empirical Green's functions are retrieved for (a) vertical, (b) radial, and (c) transverse components, respectively, after the rotation of Green's tensor. Sign-bit normalization was not applied to the traces before coherency computation. The black rectangle shows the area where a strong signal would be expected according to synthetic modelling. The arrow shows an interesting horizontal feature that is replicated over all three panels.
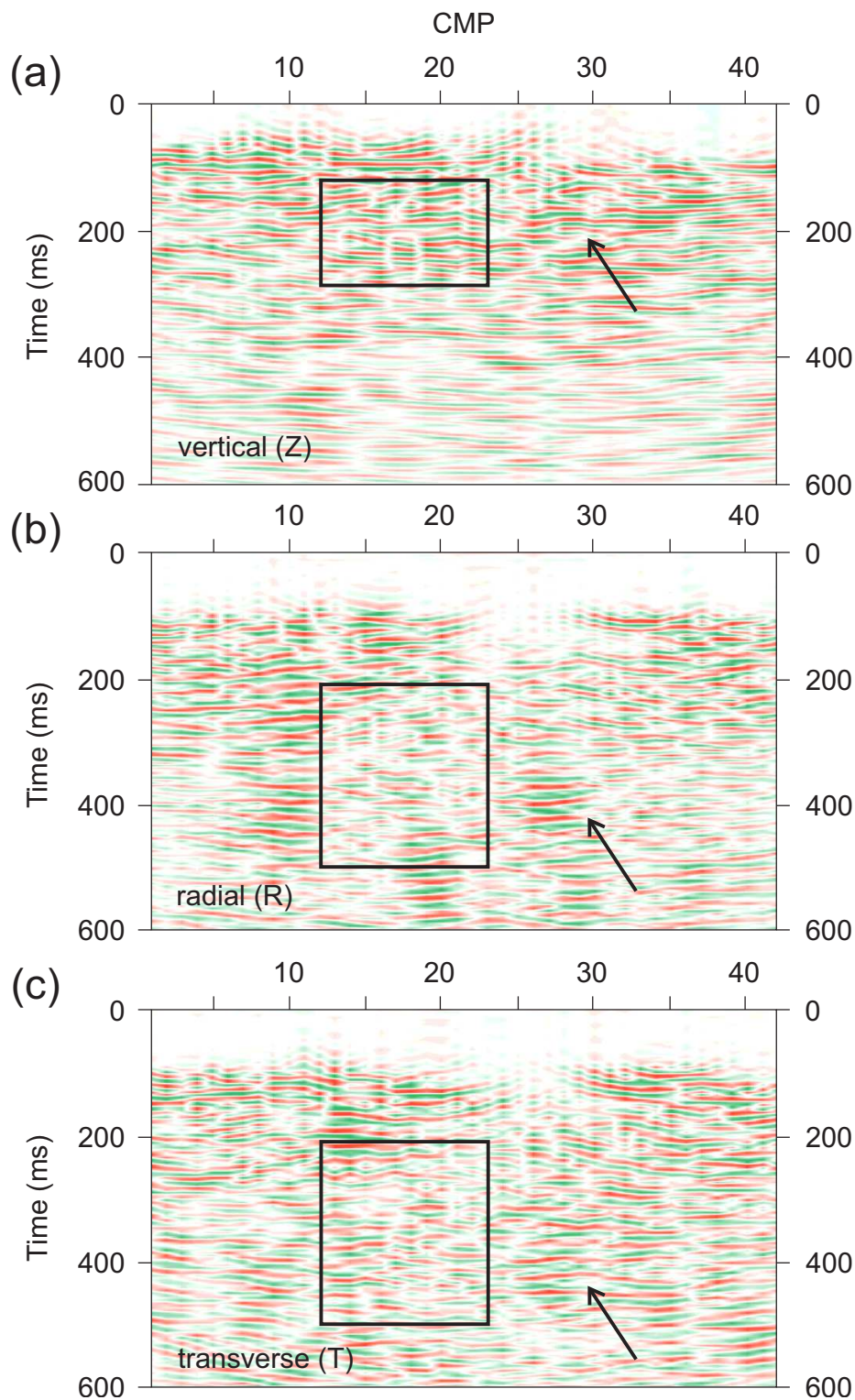
Figure 5.14: CMP stacked, NMO corrected and migrated cross sections for Line 08. The empirical Green's functions are retrieved for (a) vertical, (b) radial, and (c) transverse components, respectively, after the rotation of Green's tensor. Sign-bit normalization was applied to the traces before coherency computation. The black rectangle shows the area where a strong signal would be expected according to synthetic modelling. The arrow shows an interesting horizontal feature that is replicated over all three panels.

5.3 Assessing the reliability of the results

To pilot the SI method for body-wave retrieval in three-component data, 36 days of seismic noise collected for the CTBTO/OSI experiment were subjected to an interferometric processing sequence introduced in section 4.3. The 45 three-component Lennartz seismometers of the experiment were deployed in two parallel lines and buried in pits on the ground surface. The subsurface beneath the Northern line (Line 05) is known to host a mineralization at a depth of ca. 500 meters, and it has an intricately folded structure with intertwined sulphide schists, metasomatically altered Outokumpu ultramafic rocks, and Outokumpu ultramafics embedded in mica schist. In contrast, the geology of the Southern line is largely unknown due to only a small number of crossing drill holes.

In Kylylahti, the contacts between ore-hosting lithologies and their surroundings are subvertical – a geometry that is far from optimal for surface-based reflection seismology that operates best for subhorizontally layered structures. With an acquisition geometry like this, there is a risk that the retrieved reflectivity patterns have limited lateral continuity, and the areas of interest only appear as piecewise, scattered reflectivity. Besides, spatial aliasing is inevitable with steep dips. The data analyses were supported by forward modelling on a staggered 2D grid using the finite-difference code `fdelmodc`. Since the code was run in the acoustic mode and it did not incorporate a third dimension, it cannot model S-wave propagation, and the backscattered reflections are incorrectly assumed to originate from right below the surface receivers.

The SI workflow in this thesis is based on a noise-driven approach where 'every sample matters'. The convergence of the representation integral (2.1.15) cannot therefore be guaranteed like in event-driven approaches where only those parts of the data are selectively stacked that contribute the most to the EGF retrieval. However, the retrieved EGFs do not change significantly when the last 10 d of data are brought in for the correlation. This observation could be considered when making recommendations of acquisition times in future SI experiments.

The original data was collected at 500 Hz sample rate but was downsampled to 250 Hz because of computational cost. This reduces the best theoretically achievable depth resolution for P-waves (approximately $\lambda/4$ according to the Rayleigh criterion) from 6 m to 12 m but also negatively influences the lateral resolution (Fresnel zones), lowering it at the 500-meter depth from 100 m to about 160 m. The lithological model did not incorporate the alterations of peridotite into soapstones which, however, can add internal reflectivity to the real data. As the field statics are lacking for S-waves, there remains some uncertainty in the static shifts of individual traces at the 20 ms-level, which is reflected in the alignment of NMO corrected traces before stacking.

The quality of the migration output is definitely affected by the decision to only apply

the traditional Stolt migration for NMO stacked CMP gathers, instead of more elaborate migration and move-out correction techniques more suited to areas with steep dips. Despite the possibility that the migration output is not always faithful to the original geometry, many reflective events appear to be stable when cross-checked across various component orientations (vertical, radial, transverse) which gives weight to their authenticity. Further cross-checking can be done between unclipped and sign-bit normalized correlation panels, and in many cases, SBN seems to enhance the deep reflectors in a useful way, compensating for the lacking geometrical spreading correction.

Chapter 6

Summary

*Le bruit est du sujet, il est de l'objet. Il est de l'observé, il est de l'observateur,
de l'émetteur et du récepteur, de tout l'espace du canal. Il est de l'être et du
paraître.*

Serres, Michel (1982). *Genèse*, p. 61.

6.1   Interoperability of 3C and 1C data

Horizontal and vertical component data provide independent lines of evidence for the
seismic interpreter, and their greatest benefit – and disadvantage – is that they do not
always show consistent features. Some of this discrepancy arises because the different wave
types (P, SV, and SH) behave differently when they meet a target obliquely and off-line,
like in areas with a complicated underground geometry and steep dips. S-waves are slower
than P-waves, so they can provide complementary information of the subsurface especially
at small two-way traveltimes. Sheriff and Geldart (1995) stated in their seminal book
Exploration Seismology (p. 480) that '. . . three-component recording must be regarded as a
research rather than operational tool as of 1994,' and even as of today (2019), 3C data have
very limited operational applications for mineral exploration in crystalline bedrock. This
work hopes to put new impetus on S wave utilization by demonstrating new approaches to
processing and presenting 3C data.

Before starting this work, it was expected that transverse component would have the best
signal-to-noise ratio (SNR) for practical applications since SH waves (horizontally polarized
S waves) do not readily convert into other wave types when they hit an interface. However,
in the Kylylahti experiment it seems that the radial component panels (Figs. 5.12b and
5.14b) were more readily available for direct seismic interpretation than the transverse
panels. This, again, stresses the importance of retrieving as many components of the Green's
tensor as possible, especially if the underlying subsurface geometry is unknown.

73

6.2 Established workflow

A major problem that operators developing SI for mineral exploration sector work on is whether to favour event-driven approaches (like MESI by Chamarczuk et al. 2018) or noise-driven approaches (such as ANSI by Draganov et al. 2013). In this thesis, this question is given an additional level of complexity by investigating how the retrieved Green's functions change when one destroys all amplitude information and reduces each data sample in the full 24 h traces to its sign bit.

Another way by which the processing sequence presented here differs from previously published alternatives is the explicit symmetrisation of the Green's tensor using the reciprocities inherent in the mathematics behind it. The aim is to support three-component data processing in cases where the complicated 3D geometry of the surroundings, the qualities of the medium, or the noise background is biasing the Green's tensors and making them non-symmetric.

According to the outcomes of the present work, SBN shifts the Fourier balance towards lower frequencies throughout and enhances certain reflectors, in particular deep ones, considerably. With SBN, one is able to catch more easily up on the weak reflectors of the data. A simple explanation could be given to this behaviour. When relative amplitude information is destroyed, the operation of cross-correlation still reproduces the positions of the reflectors, but what used to be a weak reflector no longer remains that way. On the other hand, drawing parallels between lithology and what we see in the reflectivity patterns is now more difficult since the profiles do not differentiate between strong and weak reflections any more.

As a relevant outcome of this thesis, SBN could assist and guide the interpretation especially in crystalline bedrock where one already now has to utilize 'hacks' such as slowness enhancement / dip filtering to make the signal stand out from the noise. For 32-bit data collection, SBN is able to reduce the amount of data produced to $1/32^{nd}$ (e.g., from 377 GB to less than 12 GB), but will still retain plenty of useful information content. SBN thus paves the way for new effective data collection and packing algorithms for seismic observations that would retain the sign bit and the inter-correlability of the traces over brief time windows (some seconds). Such algorithms would also enable to increase sampling rates without fearing that the collected amount of data increases uncontrollably.

6.3 Potentials of the SI method

The work at hand has revealed many ways by which the veracity of the observed reflective patterns can be verified, among them increasing data multiplicity (redundancy) by boot-strapping tests, SBN tests, and computing the EGFs for the two remaining line orientations (radial and transverse).

The trade-off between the duration of the recordings and the quality of the retrieved EGFs should definitely be investigated more since it is of utmost practical relevance for the mineral exploration operator. The results of this work support the interpretation that the trade-off is met already with less than 30 days of 3C recordings in an area like Kylylahti with an elevated seismic noise background and plenty of subsurface sources. The determination of the exact form of the trade-off curve would either require a comparative study of many projects similar to COGITO-MIN or extensive forward modelling on artificial subsurface geometries.

The greatest benefit of SI is indubitably its cost-effectiveness and non-invasiveness, both features that can prove useful in sensitive areas such as nature protection sites. When SI is applied in the reconnaissance stage of a mineral exploration campaign in areas with unknown local geology, low natural seismic background, and weak subsurface reflectivities, it may also gain benefit from the SBN method introduced in this thesis. In Finland, there is an example of a major Cu–Ni–PGE deposit (Sakatti) located beneath a government-protected mire reserve and a pan-European Natura 2000 site (Mainio 2018), and in similar cases, the promotion of passive exploration methods may create a positive brand perception for mineral exploration companies.

6.4 Concluding remarks

When I first heard about seismic interferometry from my instructors, I was thrilled. It felt surreal to learn that incoherent and seemingly random noise could, through the mathematical operation of cross-correlation, give useful information about the observer's immediate surroundings. To a layman, the SI method sounds as astonishing as if a blind person walked into Finlandia Hall[1], and just by focusing on the silence that reigns, were able to form a mental image of the exact placement of the orchestral instruments on the stage, the façade of the Kangasala concert organ, and the locations of all 1,700 chairs in the main hall. I then came to realize that if these methods were adopted by the larger community of exploration geophysicists, it would pave the way for a new decade of exploration seismology in crystalline bedrock.

Working on this thesis, I grew to appreciate the amount of responsibility I was given to develop and benchmark a method whose mathematical theory was developed as late as the 21st century. For a 'serial-hobbyist' like me who is passionate about anything, being able to stand between disciplines and bring together geological and mathematical practical understanding and construct independent syntheses on them has been a mind-expanding experience.

Seismic interferometry is, in my opinion, well suited for the stage of mineral exploration

---

[1]a concert venue in Helsinki, designed by the Finnish architect Alvar Aalto and completed in 1971

where we do not yet have a precise understanding of the target, where electromagnetic methods may misguide the interpreter, and where all other resources except time are lacking. Most remarkably, seismic interferometry has the real ability to reduce costs related to data acquisition while also being non-invasive and environmentally permissive. It is truly the method of the 2020s, a passport to the future. And after all: is future not where we are all heading to?

Appendices

Appendix A

Definitions and properties

Let $f(t)$ and $g(t)$ be real or complex-valued continuous functions (signals) of a continuous variable (time), like the records of seismic ground motion. The *Fourier transform* $\mathcal{F}$ is an integral transform that transforms the signal from the time domain into the frequency domain, denoted by $f(t) \xrightarrow{\mathcal{F}} \hat{f}(\omega)$.

Throughout this thesis, I use the following convention for the Fourier transform:

$$\hat{f}(\omega) = \mathcal{F}\{f(t)\} \equiv \int_{-\infty}^{\infty} f(\tau) \exp(-j\omega\tau) \, \mathrm{d}\tau \,, \tag{A.0.1}$$

where $j^2 = -1$ defines the imaginary unit up to a sign, ω is the variable in the frequency domain, and τ is the integration variable. Then, the *inverse Fourier transform* is defined by

$$f(t) = \mathcal{F}^{-1}\{\hat{f}(\omega)\} \equiv \frac{1}{2\pi} \int_{-\infty}^{\infty} \hat{f}(\omega) \exp(j\omega\tau) \, \mathrm{d}\omega \,, \tag{A.0.2}$$

and it returns the original signal.

Some of the basic properties of the Fourier transform include linearity $[a \cdot f(t) + b \cdot g(t) \xrightarrow{\mathcal{F}} a\hat{f}(\omega) + b\hat{g}(\omega)]$ and the property that $\dfrac{\mathrm{d}}{\mathrm{d}t} f(t) \xrightarrow{\mathcal{F}} j\omega\hat{f}(\omega)$.

Cross-correlation is a binary operation for two signals $f(t)$ and $g(t)$, defined by the inner product

$$(f \star g)(t) \equiv \int_{-\infty}^{\infty} f^*(\tau)g(t + \tau) \, \mathrm{d}\tau \tag{A.0.3}$$

where $f^*(\tau)$ is the complex conjugate of the complex-valued signal $f(\tau)$. The independent variable t is called *lag* because it is the time shift of one of the signals with respect to the other. The correlation is maximized at the lag where $f(t)^*$ and $g(t + \tau)$ resemble each other the most.

Convolution is a binary operation for two signals $f(t)$ and $g(t)$, defined by

$$(f * g)(t) = \int_{-\infty}^{\infty} f(\tau)g(t - \tau) \, \mathrm{d}\tau \,. \tag{A.0.4}$$

It can be thought of as an overlay of the two signals where each point in the first time series is 'replaced' by the signal in the second time series. Unlike cross-correlation, convolution is commutative, i.e., $f * g = g * f$. It is frequently used in image processing where the convolution of an image with a point spread function (*kernel*) blurs out the sharp edges in the original image. In seismology, the observed seismic waveform can be thought of as the convolution between the source waveform, effects of the medium, site response, and the instrument response of the seismometer.

Now, consider a kernel $\delta(t)$ that would preserve the original function in the operation of convolution. This kernel has a minimal point spread around $t = 0$ and can be described as the *identity element* with respect to convolution, just as we can describe 1 as the identity element with respect to multiplication since $1x = x$ for all $x \in \mathbb{R}$. We require that

$$(f * \delta)(t) = (\delta * f)(t) = \int_{-\infty}^{\infty} \delta(\tau) f(t - \tau) \, \mathrm{d}\tau = f(t) \tag{A.0.5}$$

(*sieving property*). By choosing $f(t) = \exp(j\omega t)$ and $t = 0$, we see that the kernel $\delta(t)$ should also satisfy

$$\int_{-\infty}^{\infty} \delta(\tau) \exp(-j\omega\tau) \, \mathrm{d}\tau = \exp(j\omega \cdot 0) = 1 \ . \tag{A.0.6}$$

Contrasting this with the definition of the Fourier transform (A.0.1) we see that $\delta(t) \xrightarrow{\mathcal{F}} 1$, implying that we can express $\delta(t)$ as the inverse Fourier transform of 1, or

$$\delta(t) = \frac{1}{2\pi} \int_{-\infty}^{\infty} \exp(j\omega\tau) \, \mathrm{d}\omega \ . \tag{A.0.7}$$

The kernel $\delta(t)$ is called *Dirac's delta function*. Although looking like a definition, the equation (A.0.7) does in no way imply that such a $\delta(t)$ actually exists as a function. In fact, since the integrand does not converge as τ goes to infinity, the expression (A.0.7) is ill-defined and the integral does not even exist in the standard sense! However, a delta function expressed like this has all the necessary properties to fulfil the criterion (A.0.7), and in this sense, the notation is justified.

Dirac's delta function can be visualized as an infinitely narrow 'spike' (impulse) in time that has a unit area and whose location is determined by the zeroes of its argument. The delta function can be scaled and more than one delta functions can be multiplied together to localize the product both in time and space. For example, $q(\mathbf{x}, t) = A\delta(\mathbf{x} - \mathbf{x}')\delta(t - t')$ can be interpreted as an impulse with magnitude A at the location $\mathbf{x}'$ at the instant t'.

For our purposes, the derivative of the delta function will be formed with the auxiliary function $f(x)$ as

$$\int_{-\infty}^{\infty} f(x') \frac{\partial \delta(x' - a)}{\partial x'} \, \mathrm{d}x' = -\frac{\partial f}{\partial x}(a) \ . \tag{A.0.8}$$

Correlation and convolution have convenient expressions in the Fourier domain. They are

$$f \star g \xrightarrow{\mathcal{F}} \hat{f}^* \hat{g} \tag{A.0.9}$$

and

$$f * g \xrightarrow{\mathcal{F}} \hat{f}\hat{g} \,, \qquad\qquad\qquad (\text{A.0.10})$$

respectively.

Appendix B

OSI receiver spread

The coordinate system of the following table is KKJ4 (Finnish National Grid Coordinate System, band 4), which is a rectangular coordinate system based on the International ellipsoid 1924 and the transverse Mercator projection centred on the 30° prime meridian.

The field statics in column 5 are calculated using a layer-cake refraction static model of the shallow subsurface. The refraction static model is the same as that used for 3D grid processing of COGITO-MIN active data.

Station	X (northing, m)	Y (easting, m)	Z (elevation, m)	Field statics (ms)
ROCK	6973056.2	4465815.2	115.9	–
510	6973053.9	4465807.0	115.9	6.05
511	6973032.9	4465854.4	113.7	6.16
512	6973023.8	4465900.5	114.4	7.32
513	6973009.1	4465943.5	113.4	7.91
514	6972991.4	4466000.1	111.3	8.81
515	6972984.5	4466051.0	109.4	9.29
516	6972957.8	4466088.3	112.3	11.62
517	6972952.6	4466141.1	107.7	10.57
521	6972892.8	4466330.4	104.7	9.97
522	6972868.4	4466373.9	106.2	10.26
524	6972840.4	4466471.8	108.9	13.62
525	6972824.3	4466524.4	110.0	15.46
526	6972812.1	4466569.2	104.8	14.66
527	6972793.7	4466617.9	104.6	13.51
528	6972785.2	4466666.5	106.9	13.67
529	6972765.8	4466713.9	100.3	9.71
530	6972749.9	4466760.9	101.5	9.24

Station	X (northing, m)	Y (easting, m)	Z (elevation, m)	Field statics (ms)
531	6972735.8	4466811.4	98.8	8.37
532	6972715.0	4466847.1	99.6	9.55
533	6972704.8	4466900.4	101.9	11.44
534	6972684.3	4466956.4	108.1	16.11
535	6972678.2	4467005.6	107.7	15.75
536	6972670.5	4467044.4	106.0	14.68
537	6972640.4	4467102.8	109.1	16.05
538	6972619.1	4467142.0	101.0	11.58
539	6972613.9	4467189.7	97.4	9.83
812	6972448.5	4465717.6	114.3	11.53
813	6972435.8	4465768.3	114.3	11.40
814	6972427.3	4465812.8	114.2	11.33
815	6972406.3	4465865.1	114.9	11.31
816	6972389.9	4465908.8	112.5	10.17
817	6972373.8	4465949.0	105.6	7.41
818	6972363.1	4466003.6	111.9	9.63
819	6972347.1	4466056.4	106.1	7.91
820	6972330.9	4466097.6	101.2	6.79
821	6972313.3	4466148.5	101.7	7.48
822	6972308.2	4466197.5	97.4	6.82
828	6972206.4	4466480.3	92.8	20.11
829	6972191.6	4466533.7	92.7	22.79
830	6972176.7	4466574.9	93.0	25.72
831	6972162.8	4466625.5	97.4	25.43
832	6972143.1	4466675.1	104.1	25.13
833	6972131.3	4466722.3	102.0	18.16
834	6972108.4	4466765.5	100.7	13.69

Bibliography

Aki, Keiiti and Paul G. Richards (2002). *Quantitative Seismology*. 2nd ed. University Science Books, p. 704. ISBN: 0-935702-96-2.

Anderson, Don L. (2007). *New Theory of the Earth*. Cambridge: Cambridge University Press, p. 384. ISBN: 0521849594.

Baan, Mirko van der (July 2006). "PP/PS Wavefield separation by independent component analysis". In: *Geophysical Journal International* 166.1, pp. 339–348. DOI: 10.1111/j.1365-246x.2006.03014.x. URL: https://doi.org/10.1111/j.1365-246x.2006.03014.x.

BABEL Working Group (1990). "Evidence for early Proterozoic plate tectonics from seismic reflection profiles in the Baltic shield". In: *Nature* 348.34–38. DOI: 10.1038/348034a0.

Bensen, G. D. et al. (June 2007). "Processing seismic ambient noise data to obtain reliable broadband surface wave dispersion measurements". In: *Geophysical Journal International* 169.3, pp. 1239–1260. DOI: 10.1111/j.1365-246x.2007.03374.x.

Boliden (2015). *Competitive Mines and Smelters. Annual Report*. URL: https://www.companyreporting.com/sites/default/files/annual-report-index/boliden_annual-report_2015.pdf (visited on 01/07/2019).

— (2017). *Mineral Reserves and Mineral Resources*. URL: https://www.boliden.com/globalassets/operations/exploration/mineral-reserve/201802136644-1_eng.pdf (visited on 01/07/2019).

— (2018). *Metals for a Sustainable Society. Annual Report*. URL: https://vp217.alertir.com/afw/files/press/boliden/201903076646-1.pdf (visited on 05/12/2019).

Bönnemann, Christian (2017). *Monitoring Compliance with the Comprehensive Nuclear-Test-Ban Treaty (CTBT). Contributions by the German National Data Center*. Ed. by C. Pilger, L. Ceranna, and C. Bönnemann. Geologisches Jahrbuch, Reihe B, Heft 105. Chap. 1. Verification of the CTBT and its Implementation in Germany. ISBN: 3510968589.

Chamarczuk, Michał et al. (Sept. 2018). "Tu 2MIN 03 Seismic Interferometry for Mineral Exploration: Passive Seismic Experiment over Kylylahti Mine Area, Finland". In: DOI: 10.3997/2214-4609.201802703.

Chamarczuk, Michał et al. (2019). "Automatic 3D illumination-diagnosis method for large-N arrays: robust data scanner and machine-learning feature provider". In: *Geophysics* 84.3, p. 48. DOI: 10.1190/geo2018-0504.1.

Cheraghi, Saeid, James A. Craven, and Gilles Bellefleur (2015). "Feasibility of virtual source reflection seismology using interferometry for mineral exploration: A test study in the Lalor Lake volcanogenic massive sulphide mining area, Manitoba, Canada". In: *Geophysical Prospecting* 63.4, pp. 833–848. DOI: 10.1111/1365-2478.12244.

Condie, Kent C., David J. Des Marais, and Dallas Abbott (Mar. 2001). "Precambrian superplumes and supercontinents: A record in black shales, carbon isotopes, and paleoclimates?" English. In: *Precambrian Research* 106.3-4, pp. 239–260. ISSN: 0301-9268. DOI: 10.1016/S0301-9268(00)00097-8.

Cupillard, Paul and Yann Capdeville (Apr. 2010). "On the amplitude of surface waves obtained by noise correlation and the capability to recover the attenuation: a numerical approach". In: *Geophysical Journal International*. DOI: 10.1111/j.1365-246x.2010.04586.x.

Draganov, Deyan et al. (2013). "Seismic exploration-scale velocities and structure from ambient seismic noise (>1 Hz)". In: *Journal of Geophysical Research: Solid Earth* 118.8, pp. 4345–4360. DOI: 10.1002/jgrb.50339.

Fitton, J (Jan. 2007). "The OIB paradox". In: *Special Paper of the Geological Society of America* 430, pp. 387–412. DOI: 10.1130/2007.2430(20).

Foulger, Gillian R (2011). *Plates vs plumes: a geological controversy*. John Wiley & Sons. ISBN: 978-1-4443-3679-5.

Gestermann, N. et al. (Apr. 2016). "The Seismic Aftershock Monitoring System (SAMS) for OSI – Experiences from IFE14". In: *EGU General Assembly Conference Abstracts*. Vol. 18. EGU General Assembly Conference Abstracts, EPSC2016–12350.

Heinonen, Suvi et al. (2019). "Cost-Effective Seismic Exploration: 2D Reflection Imaging at the Kylylahti Massive Sulfide Deposit, Finland". In: *Minerals* 9.5. ISSN: 2075-163X. DOI: 10.3390/min9050263.

Höltta, Pentti et al. (2012). "Archaean Complexes of the Karelia Province in Finland". In: *Special Paper* 54: *The Archaean of the Karelia Province in Finland*. Ed. by Pentti Höltta, pp. 9–20.

Koistinen, Tapio J. (1981). "Structural Evolution of an early Proterozoic strata-bound Cu–Co–Zn deposit, Outokumpu, Finland". In: *Transactions of the Royal Society of Edinburgh: Earth Sciences* 72, pp. 115–158.

— (2001). "Raahe-Laatokka-vyöhykkeen rakenne-evoluutio". In: *Geophysical Research Abstracts. Raahe–Laatokka symposium* (Kuopio, Mar. 20–21, 2001).

Koivisto, Emilia et al. (2018). "From Regional Seismics to High-Resolution Resource Delineation: Example from the Outokumpu Ore District, Eastern Finland". In: *EAGE Near Surface Geoscience Conference & Exhibition 2018. 2nd Conference on Geophysics for Mineral Exploration and Mining* (Porto, Sept. 9–13, 2018).

Kontinen, Asko (2005). *Geology of the Kylylahti Cu-Co Deposit, Finland. A report to Vulcan Resources Ltd, Perth, Western Australia*. Raportti. Kuopio: Geologian tutkimuskeskus. 60 pp.

Kontinen, Asko, Petri Peltonen, and Hannu Huhma (2006). *Description and genetic modelling of the Outokumpu-type rock assemblage and associated sulphide deposits*. Final technical report for GEOMEX J.V., Workpackage Geology. Kuopio and Espoo: GTK and Outokumpu Oy. 378 pp.

Korsman, Kalevi et al. (1999). "The GGT/SVEKA Transect: Structure and Evolution of the Continental Crust in the Paleoproterozoic Svecofennian Orogen in Finland". In: *International Geology Review* 41.4, pp. 287–333. DOI: 10.1080/00206819909465144.

Kukkonen, Ilmo and Raimo Lahtinen, eds. (2006). *Finnish Reflection Experiment FIRE 2001–2005*. Vol. 43. Special Paper. Geological Survey of Finland. 247 pp.

Labak, P., P. Lindblom, and G. Malich (2017). "Seismic field measurements in Kylylahti, Finland, in support of the further development of geophysical seismic techniques for CTBT On-site Inspections". In: *Geophysical Research Abstracts. 19th EGU General Assembly* (Vienna).

Lahtinen, Raimo et al. (2012). "Main metallogenic events in Fennoscandia: summary". In: *Special Paper* 53: *Mineral deposits and metallogeny of Fennoscandia.* Ed. by P. Eilu, pp. 397–401.

Luhta, Tuija (2019). "Petrophysical properties of the Kylylahti Cu-Au-Zn sulphide mineralization and its host rocks". Master's thesis. Gustaf Hällströmin katu 2, FI-00014 Helsingin yliopisto: University of Helsinki, Faculty of Science.

Mainio, Tapio (Mar. 26, 2018). "Sodankylässä on etsitty jo vuosia tapaa päästä käsiksi sensaatiomaiseen "Eldoradoon" – ratkaiseeko vinotunneli kiistellyn Sakatin ongelman?" In: *Talouselämä.* URL: https://www.talouselama.fi/uutiset/sodankylassa-on-etsitty-jo-vuosia-tapaa-paasta-kasiksi-sensaatiomaiseen-eldoradoon-ratkaiseeko-vinotunneli-kiistellyn-sakatin-ongelman/185bcfa6-eba4-3519-bd03-5ef668466c9b (visited on 01/10/2019).

Nironen, Mikko (2017). "Guide to the geological map of Finland – Bedrock 1:1 000 000". In: *Special Paper* 60: *Bedrock of Finland at the scale 1:1 000 000 – Major stratigraphic units, metamorphism and tectonic evolution.* Ed. by Mikko Nironen, pp. 41–76.

Nishida, Kiwamu, Jean-Paul Montagner, and Hitoshi Kawakatsu (2009). "Global Surface Wave Tomography Using Seismic Hum". In: *Science* 326.5949, pp. 112–112. DOI: 10.1126/science.1176389.

Ogg, James G., Gabi M. Ogg, and Felix M. Gradstein (2016). "Precambrian". In: *A Concise Geologic Time Scale.* Elsevier, pp. 19–28. DOI: 10.1016/b978-0-444-59467-9.00003-0.

Papunen, Heikki (1987). "Outokumpu-type ores". In: *Special Paper* 1: *Otto Trüstedt symposium in Finland on June 3–5, 1985.* Ed. by T. A. Häkli, pp. 41–50.

Peltonen, P. et al. (2008). "Outokumpu revisited: New mineral deposit model for the mantle peridotite-associated Cu–Co–Zn–Ni–Ag–Au sulphide deposits". In: *Ore Geology Reviews* 33.3, pp. 559–617. ISSN: 0169-1368. DOI: 10.1016/j.oregeorev.2007.07.002.

Peltonen, Petri et al. (2007). "New mineral deposit model for the Cu–Co–Zn–Ni–Ag–Au sulphide deposits in Outokumpu, Finland". In: *SGA News* (21), pp. 7–9.

Quiros, Diego, Larry D. Brown, and Doyeon Kim (2016). "Seismic interferometry of railroad induced ground motions: Body and surface wave imaging". In: *Geophysical Journal International* 205, pp. 301–313. DOI: 10.1093/gji/ggw033.

Riedel, Marko et al. (2018). "Underground Vertical Seismic Profiling with Conventional and Fiber-Optic Systems for Exploration in the Kylylahti Polymetallic Mine, Eastern Finland". In: *Minerals* 8 (11), p. 21. DOI: 10.3390/min8110538.

Sabra, Karim G. et al. (2005). "Surface wave tomography from microseisms in Southern California". In: *Geophysical Research Letters* 32.14. DOI: 10.1029/2005GL023155.

Salisbury, Matthew H., Bernd Milkereit, and Wouter Bleeker (1996). "Seismic imaging of massive sulfide deposits: Part 1, Rock properties". In: *Economic Geology* 91, pp. 821–828.

Sheriff, R. E. and L. P. Geldart (1995). *Exploration Seismology.* Cambridge University Press. ISBN: 9780521468268.

Singh, Brij et al. (in press). "Sparse 3D Seismic Imaging in the Kylylahti Mine Area, Eastern Finland: Comparison of Time vs Depth Approach". In: *Minerals.*

Snieder, Roel and Christoph Sens-Schönfelder (2015). "Seismic interferometry and stationary phase at caustics". In: *Journal of Geophysical Research: Solid Earth* 120.6, pp. 4333–4343. DOI: 10.1002/2014JB011792.

Tange, Ole (2011). "GNU Parallel – The Command-Line Power Tool". In: *;login: The USENIX Magazine* 36.1, pp. 42–47.

Thorbecke, Jan W. and Deyan Draganov (2011). "Finite-difference modeling experiments for seismic interferometry". In: *Geophysics* 76.6, H1–H18. DOI: 10.1190/geo2010-0039.1.

Walter, Marco et al. (2018). "Processing of Kylylahti data for the development of OSI resonance seismometry". OSI Expert Meeting on Resonance Seismometry. Unpublished.

Wapenaar, Kees and Jacob Fokkema (2006). "Green's function representations for seismic interferometry". In: *Geophysics* 71.4, SI33–SI46. DOI: 10.1190/1.2213955.